

FLUORESCENCE PROPERTIES OF BLINKING SEMICONDUCTING
NANOPARTICLES AND INTERACTION EFFECTS

Siying Wang

A DISSERTATION

in

Physics and Astronomy

Presented to the Faculties of the University of Pennsylvania

in

Partial Fulfillment of the Requirements for the

Degree of Doctor of Philosophy

2011

Supervisor of Dissertation

Signature _____

Marija Drndić, Associate Professor, Physics and Astronomy

Graduate Group Chairperson

Signature _____

A.T.Charlie Johnson, Professor, Physics and Astronomy

Dissertation Committee

A.T.Charlie Johnson, Professor, Physics and Astronomy

Randall D. Kamien, Professor, Physics and Astronomy

Eugene J. Mele, Professor, Physics and Astronomy

Evelyn Thomson, Associate Professor, Physics and Astronomy

UMI Number: 3463099

All rights reserved

INFORMATION TO ALL USERS

The quality of this reproduction is dependent on the quality of the copy submitted.

In the unlikely event that the author did not send a complete manuscript and there are missing pages, these will be noted. Also, if material had to be removed, a note will indicate the deletion.



UMI 3463099

Copyright 2011 by ProQuest LLC.

All rights reserved. This edition of the work is protected against unauthorized copying under Title 17, United States Code.



ProQuest LLC.
789 East Eisenhower Parkway
P.O. Box 1346
Ann Arbor, MI 48106 - 1346

Acknowledgements

First and foremost, I would like to thank my advisor, Dr. Marija Drndic. Marija is an excellent mentor, both personally and professionally. She encouraged me from the first step of my project and never gave up believing that I could carry it on to the end. She is always willing to discuss problems with me but always letting me solve it on my own. I would also like to extend my appreciation to the members of my dissertation committee, Dr. Charlie Johnson, Dr. Randall Kamien, Dr. Eugene Mele, and Dr. Evelyn Thomsone for their guidance.

I am also very grateful to Dr. Catherine Crouch and Dr. Dmitry Novikov for the excellent collaboration. Catherine is also one of my first advisors to lead me into this research field. Dmitry is an excellent theorist and he shared many great ideas with us on the theory, modeling and data analysis.

I would like to express my thanks to all my group members, Claudia Querner, Tali Dadosh, Michael Fischbein, Lauren Willis, Matt Puster, Jessamyn Fairfield, Meni Wanunu, Kim Venta, Chris Merchant, Ken Healy and my friends in condensed matter experiments groups at Penn for discussions and inspirations of Physics. I would also like to thank my friends Qingwei Zhang, Chen Xu and Jing Cai for their friendship and many happy hours we had together in the past six years.

Finally, I owe my deepest gratitude to my mother, Jirui Qi, and my father, Dapeng Wang, for their support. I know I have made you proud. I would like to express my special thanks to my boyfriend, Haibin Liu, for his support, encouragements and accompanies.

ABSTRACT

FLUORESCENCE PROPERTIES OF BLINKING SEMICONDUCTING NANOPARTICLES AND INTERACTION EFFECTS

Siying Wang

Marija Drndić

Many molecular and nanoscale systems, ranging from fluorescent proteins to semiconductor nanoparticles, are known to emit light intermittently, *i.e.* to “blink”, under continuous illumination. In single semiconductor nanoparticles, the distributions of bright and dark periods (“on” and “off” times) in the fluorescence of individual particles follow non-Poissonian (Lévy) statistics. In the last two decades, blinking has been widely studied in spherical CdSe nanocrystals (NCs), both experimentally and theoretically. However, the mechanism leading to these statistics is still incompletely understood, but almost certainly involves charge transfer between the nanoparticle and its environment. Recently, novel anisotropic nanocrystal shapes have been synthesized. These are expected to offer a rich variety of electrical and optical properties. In this dissertation, fluorescence blinking from CdSe nanorods (NRs) in both single particle level and ensemble behaviour were studied. Fluorescence blinking statistics was measured from single CdSe NRs of different sizes with aspect ratios up to 11, with different surface ligands producing different degrees of surface passivation. The measurements of blinking statistics from NRs were compared to those from spherical CdSe core and CdSe/ZnS core/shell NCs. A technique of fluorescence measurements correlated with the particle number by direct particle counting (from single nanoparticles to ~10000) was developed.

This was uniquely enabled by combined transmission-electron (TEM) and atomic-force microscopy (AFM). The long ($\sim 10^4$ s) blinking measurements also directly reveal the previously unobserved truncation of the power law distribution of the off-times for single nanoparticles. Clusters containing two or three NRs exhibit intermittent fluorescence intensity trajectories, $I(t)$, similar to those of individual NRs. In contrast, statistically distinguishable blinking parameters are observed for clusters of five or more particles. With increasing particle number, the cluster fluorescence increases in intensity and the relative fluorescence fluctuations, originating from single particle events, decrease in accordance with the central limit theorem. Furthermore, blinking nanorods interact with each other in a cluster, and the interactions greatly affect the blinking statistics. The interaction-induced increase of on-time durations scales with the cluster size, revealing a novel collective effect in fluorescence at the nanoscale. It suggests that small nanorod clusters may be usable as nanoscale light sources with very long emission times.

Table of Contents

Acknowledgements	ii
1. Introduction.....	1
1.1 CdSe nanocrystals	1
1.2 Blinking statistics of CdSe/ZnS NCs.....	2
1.3 Motivation.....	3
2. Fluorescence blinking statistics from CdSe core and core-shell nanorods.....	7
2.1 Introduction.....	7
2.2 Experimental methods	8
2.2.1 Samples of CdSe NRs.....	8
2.2.2 Measurement of the absorption cross-section σ_λ	9
2.2.3 Fluorescence measurements.....	10
2.3 Results and discussion	11
2.3.1 Statistical analysis of fluorescence on- and off-times.....	11
2.3.2 Off-time statistics.....	14
2.3.3 On-time statistics	15
2.3.4 Effect of ligands.....	18
2.3.5 Effect of aspect ratio	20
2.3.6 Effect of excitation intensity.....	22
2.4 Conclusion	24
2.5 Supplementary information	25
2.5.1 Fitting methods of probability densities for off-times	25

2.5.2	Effect of experiment duration on individual NR on-time distributions.....	28
2.5.3	Determination of uncertainty in τ_c^{on}	29
3.	Blinking statistics correlated with nanoparticle number.....	31
3.1	Introduction.....	31
3.2	Experimental methods	33
3.3	Results and discussion	35
3.3.1	Individual NRs and effect of thresholds	35
3.3.2	A truncated Lévy off-time distribution	36
3.3.3	Small clusters.....	38
3.3.4	Blinking parameters	41
3.4	Conclusion	45
3.5	Supplementary information	46
3.5.1	Experimental details on NR synthesis and characterization	46
3.5.2	Determination of fluorescence intensity vs. time from fluorescence movies on silicon nitride membranes	49
3.5.3	Background correction and definition of threshold for fluorescence intensity trajectories on silicon nitride membranes	50
3.5.4	Dependence of blinking parameters on NR angle relative to the laser polarization direction.....	53
3.5.5	Auto-correlation function analysis.....	54
4.	Fluorescence dynamics of semiconductor nanorod clusters.....	55

4.1	Introduction.....	55
4.2	Experimental methods	56
4.3	Results and discussion	58
4.3.1	Fluorescence/TEM/AFM correlation of NR clusters and direct particle counting	58
4.3.2	Dependence of fluorescence intensity on N and assembly patterns.....	62
4.3.3	Dependence of fluorescence fluctuations on particle number	65
4.3.4	Fluorescence dynamics dependence on particle number (N < 10000)	67
4.3.5	Very large clusters ($N > 10000$) and long time-dependence of fluorescence	69
4.3.6	Statistical predictions of ensemble behavior based on single-particle dynamics	72
4.3.7	Deviations from the statistical model	76
4.4	Conclusion	78
4.5	Supplementary information	79
4.5.1	Details on direct particle counting	79
4.5.2	Additional transmission electron and atomic force micrographs of NR clusters	83
4.5.3	Additional correlations of structural and fluorescence parameters of NR clusters	86

4.5.4	Fluorescence vs. time of individual NR on Si ₃ N ₄	87
5.	Collective fluorescence enhancement in nanoparticle clusters.....	88
5.1	Introduction.....	88
5.2	Experimental methods	90
5.3	Results and discussion	91
5.3.1	Fluorescence intensity of NR clusters correlated with the number of NRs, N	91
5.3.2	Role of interactions in blinking statistics.....	91
5.3.3	Autocorrelation functions and charging process.....	100
5.3.4	Physical model	101
5.4	Conclusion	106
5.5	Supplementary information	107
5.5.1	Maximum and mean on-time results hold qualitatively for a range of thresholds	107
5.5.2	Comparison of independent fluorescence measurements on two different chips	107
5.5.3	Overlapping effect of summing up digitized traces of nine independent NRs	109
5.5.4	Integration of fluorescence signals from independent NRs and Monte-Carlo simulation	109
5.5.5	Total number of "on" events	111
5.5.6	Estimates of electric field-induced exciton rearrangement and field-driven coordinated trapping/detrapping	112

5.5.7	Fraction of close-packed NRs within clusters	114
5.5.8	“On” time vs. particle separation for clusters with $N=2$	115
Bibliography	116

List of Tables

2.1 Characteristics of CdSe core of samples	9
2.2 Off-time (on-time) exponents $\alpha_{off(on)}$ and on-time crossover times τ_c^{on} obtained for CdSe core and core/shell NCs and NRs	13
2.3 Intensity dependence of off- and on-time parameters for sample NR4	22
3.1 Blinking parameters of individual NRs ($N = 1$) and small NR clusters up to $N=15$	40
3.2 List of blinking parameters of NR clusters for different threshold levels	52
4.1 Structural details and fluorescence properties of NR clusters	63
4.2 Fitting parameters used to generate the theoretical intensity vs. time curves of nanocrystal and NR ensembles	77
4.3 Orientation with respect to the laser polarization	80
4.4 Summary of structural parameters of studied NR clusters	81
5.1 Fraction of close-packed NRs	115

List of Figures

1.1 A fluorescence intensity trajectory from a blinking CdSe/ZnS NC	1
1.2 A diagram of a CdSe nanocrystal core and a TEM image of a CdSe NC with a diameter of 5 nm	2
1.3 Off-time and on-time PDFs of individual NCs.....	3
1.4 A diagram of a charging model for blinking NCs	4
1.5 A diagram of elongated NRs in two different lengths and a NC with the same diameter.....	5
2.1 Low-resolution and high-resolution TEM images of 5.2×18 nm NRs	9
2.2 Schematic of the wide-field fluorescence imaging setup using an upright epi-fluorescence microscope	11
2.3 Representative intensity <i>vs.</i> time data, $I(t)$, obtained from a single NR and off-time probability density, $P(t_{off})$, obtained from single nanoparticles	12
2.4 On-time probability density $P(t_{on})$ obtained from single nanoparticles.....	15
2.5 Aggregated on-time probability distributions for nanorods with the same dimension but different ligands	19
2.6 Inverse crossover time <i>vs.</i> aspect ratio for all TOPO-capped core NC and NR samples studied	21
2.7 Excitation intensity dependence of the inverse crossover time of NR4	23
2.8 Fitting methods of probability densities for off-times	26
2.9 Effect of experiment duration on individual NR on-time distributions.....	29
2.10 Determination of uncertainty in τ_c^{on}	30

3.1 Schematic of the setup of wide-field fluorescence imaging correlated with TEM	33
3.2 Fluorescence micrograph and the TEM image of an individual CdSe/ZnSe/ZnS core/double shell NR.....	35
3.3 Off-time probability density with a truncated power fit	38
3.4. $I(t)$ and corresponding TEM images of small clusters.....	40
3.5 Fluorescence intensities <i>vs.</i> time, $I(t)$, in order of increasing particle number	42
3.6 Histograms of the blinking parameters	43
3.7 Absorption and emission spectra of CdSe core NRs recorded in toluene	48
3.8 Fluorescence micrograph of a 18 by $12 \mu\text{m}^2$ region and TEM of the same transparent window region patterned with a grid of gold lines	49
3.9 Determination of fluorescence intensity <i>vs.</i> time from fluorescence movies on silicon nitride membranes	50
3.10 Background signal with a polynomial fit and intensity trajectory of an individual NR with different thresholds	51
3.11 Histogram of the blinking parameters of individual NRs and small clusters up to 15NRs, shown for $m_{dark}+6\sigma_{dark}$	52
3.12 Histogram of the blinking parameters of individual NRs and small clusters up to 15NRs, shown for $m_{dark}+7\sigma_{dark}$	53
3.13 Histogram of the blinking parameters of individual NRs and small clusters up to 15NRs, shown for $m_{dark}+8\sigma_{dark}$	53
3.14 Blinking parameters of individual NRs on silicon nitride substrates as a function of NR angle relative to the laser polarization direction.....	54

3.15 Autocorrelation functions of individual NRs and small NR clusters	54
4.1 Fluorescence micrograph correlated with TEM and AFM of the same region on the substrate	57
4.2 Fluorescence micrograph correlated with TEM and AFM of a cluster	58
4.3. TEM images and corresponding integrated fluorescence <i>vs.</i> time	60
4.4. Mean fluorescence intensity <i>vs.</i> number of NRs for different clusters.....	64
4.5 Fluorescence intensity <i>vs.</i> time and the corresponding TEMs.....	66
4.6 Normalized fluorescence intensity <i>vs.</i> time on a log ₁₀ -log ₁₀ scale for NR clusters	68
4.7 Normalized fluorescence intensity <i>vs.</i> time on a log ₁₀ -log ₁₀ scale for NR clusters containing ~10000 NRs	71
4.8 Details on direct particle counting	79
4.9 Additional transmission electron and atomic force micrographs of NR clusters	83
4.10 Cluster area <i>vs.</i> total number of NRs shows an approximately linear increase	86
4.11 Mean fluorescence intensity <i>vs.</i> number of in-plane NRs	86
4.12 Statistical analysis of 6 h-long movies of 7 different individual NRs divided into three 2 h-long segments	87
5.1 Correlated fluorescence and TEM images of a 18 × 12 μm ² region on the Si ₃ N ₄ membrane window	92
5.2 Digitized segment of the fluorescence time trace from a cluster of nine NRs, from N = 9 uncorrelated NRs, and from a single NR	93
5.3 Probability density of on-times from the traces shown in Figure 5.2 for N = 9	94
5.4 Scaling of mean and maximum on-times with the cluster size N	95

5.5 Scaling of mean and maximum off-times with the cluster size N	96
5.6 Scaling of the fraction of the total time spent in the on-states with N	98
5.7 Autocorrelation functions of individual NRs.....	101
5.8 Proposed schematic diagrams of the charging process in a cluster of $N = 2$ and in two isolated NRs.....	102
5.9 Scaling of mean and maximum on-times with the cluster size N with a range of thresholds.....	107
5.10 Fluorescence micrographs of two silicon nitride chips.....	108
5.11 Compare the results from two chips measured independently	108
5.12 Overlapping effect of summing up digitized traces of nine independent NRs to produce the red trace in Figure 5.2	109
5.13 Scaling of mean and maximum on-times and mean and maximum off-times with the cluster size N using two methods of integrating independent single NRs.....	110
5.14 The total number of "on" events vs. the cluster size N	111
5.15 Fraction of close-packed NRs vs number of NRs of 74 clusters	114
5.16 Histogram of the fraction of close-packed NRs in clusters	115
5.17 Mean and maximum on-time vs. inter-particle separation of cluster with $N =$ 2	115

Chapter 1

Introduction

A system's complexity is often tied to its statistical properties. In chemical systems, complexity of the environment results in fluorescence intermittency under continuous illumination, or “blinking” and is displayed by many types of single emitters, such as single molecules, green fluorescent proteins, light harvesting complexes, organic fluorophores, and semiconductor nanoparticles. [Cichos 2007 and Frantsuzov 2008] The fluorescence intensity stochastically changes between bright and dark regimes, commonly referred to as on- and off-states (Figure 1.1). Furthermore, blinking from colloidally synthesized semiconductor nanocrystals (NCs) does not follow a simple two-level quantum jump model, but instead displays approximately power law (Lévy) statistics over many decades in time. [Cichos 2007, Frantsuzov 2008, Nirmal 1996, Wang 2006, Protasenko 2005, Glennon 2007]

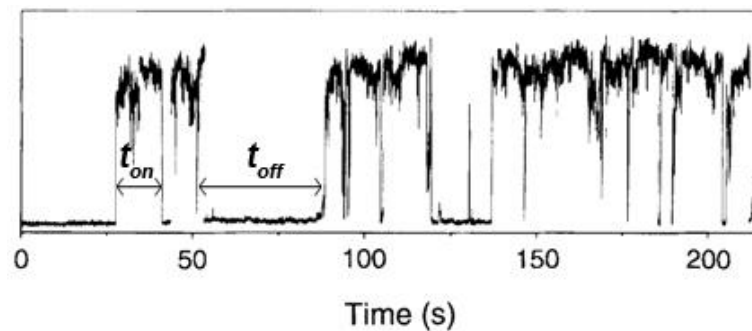


Figure 1.1 A fluorescence intensity trajectory from a blinking CdSe/ZnS NC, where t_{on} and t_{off} are the time duration of an on- and off-time event, respectively. The time resolution is ~ 100 ms.

1.1 CdSe nanocrystals (NCs)

Blinking behaviour has been widely studied in spherical CdSe nanocrystals (NCs), both experimentally and theoretically. The CdSe NCs in this study are made via colloidal

synthesis.[Murray 1993, Kuno 1997] Figure 1.2 shows a diagram and a transmission electron microscopy (TEM) of a CdSe nanocrystal core passivated with the organic ligands, trioctyl phosphine oxide (TOPO). In order to further passivate surface sites, the colloidal CdSe NCs are usually overcoated with a higher band gap semiconductor, ZnS. With the ZnS shell, CdSe NCs become noticeably brighter, with quantum yields increasing from 10% to 30%–50% at room temperature.[Peng 1997, Dabbousi 1997, Hines 1996] The colloidal synthesis is a highly adjustable process in order to achieve large number of uniform NCs with controllable size.

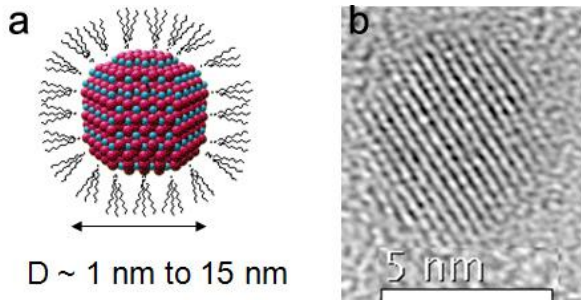


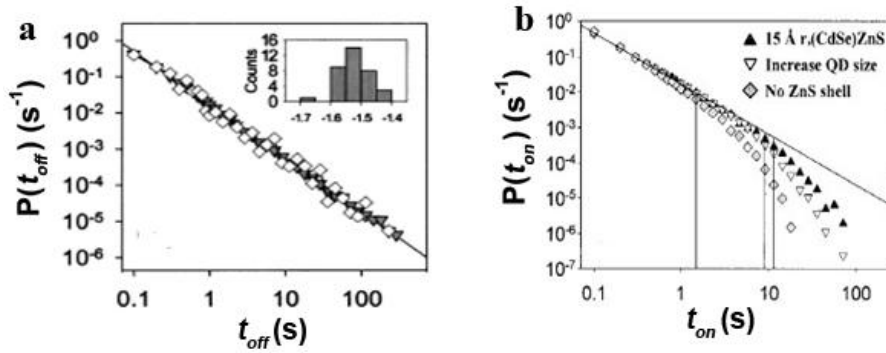
Figure 1.2 a) A diagram of a CdSe nanocrystal core passivated with the organic ligands, TOPO. b) A TEM image of a CdSe NC with a diameter of 5 nm.

1.2 Blinking statistics of CdSe/ZnS NCs

Blinking in CdSe/ZnS NCs differs significantly from blinking observed from other single fluorophores in the probability distribution of on or off events of a particular duration. If a histogram of the duration of all off-time events, t_{off} , observed from each NC is calculated, the resulting probability density function (PDF) of the off times, $P(t_{off})$, has been found for spherical core/shell CdSe/ZnS NCs to follow a power law or Lévy statistics (Figure 1.3a),

$$P(t_{off}) = At_{off}^{-\alpha_{off}} \quad \text{Eq. 1.1}$$

where $\alpha_{off} \sim 1.5$. [Kuno 2000, Shimizu 2001, van Sark 2002, Brokmann 2003, Kobitski 2004, Hohng 2004, Müller 2004, Yao 2005] The PDF of on-times, $P(t_{on})$, likewise follows a power law for short t_{on} , but falls below the power law at longer on-times at room temperature (Figure 1.3b). Probability distributions observed from most other single fluorophores are exponential or near-exponential. [Frantsuzov 2005]



K. T. Shimizu *et al.* *Physical Review B*, **63**, 205316, 2001

Figure 1.3 a) Off-time and b) on-time PDFs of individual NCs.

1.3 Motivation

The origin of the observed Lévy statistics has been the subject of extensive investigation, with several models proposed. [Cichos 2007, Frantsuzov 2008, Nirmal 1996] Although the details of the mechanism are still poorly understood, it is thought that NCs become “dark” or cease emitting light, when one of the charge carriers in a photoexcited exciton becomes trapped at the surface of the NC or tunnels off the NC into the environment, leaving a net charge delocalized in the NC core. In the charged core, highly efficient Auger processes lead to rapid nonradiative recombination of subsequent photoexcited excitons. Fluorescence then resumes once the core regains electrical neutrality (Figure 1.4). [Cichos 2007, Frantsuzov 2008, Nirmal 1996, Wang 2009, Yu 2006, Lee 2009,

Wang 2008, Querner 2008] Recently, Krauss and Klimov's groups observed near-complete suppression of blinking in NCs synthesized with graded shells that greatly reduce the efficiency of Auger recombination, providing strong support for the proposal that dark states involve Auger recombination.[Wang 2009, Garcia-Santamaria 2009] However, the exact mechanism is still under theoretical and experimental investigation.

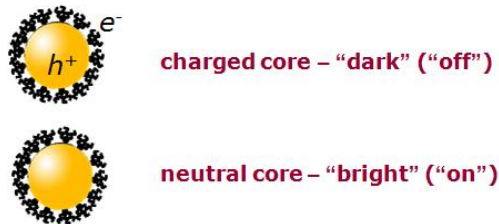


Figure 1.4 A diagram of a charging model for blinking NCs.

Recently, novel anisotropic nanocrystal shapes have been synthesized.[Manna 2000] These are expected to offer a rich variety of electrical and optical properties. One example is the nanorod (NR), a NC that is elongated along the crystal *c*-axis so that charge carriers are most strongly quantum-confined along the NR cross-section (Figure 1.5). The elongation of NRs also makes them better conductors than spherical NCs, and thus more suitable for certain device applications. [Huynh 2002, Millo 2004] Studying the optical and electrical properties of NRs offers the possibility of observing the transition from quantum states confined in all three dimensions (0D states), as in a spherical NC, to states confined in only two dimensions (1D states). While a variety of fluorescence measurements have been made on single NRs [Millo 2004, Chen 2001, Rothenberg 2004, Rothenberg 2005, Le Thomas 2005] and other elongated NCs, [Müller 2005a, Müller 2005b] a systematic study of NRs with different aspect ratios and blinking statistics from ensembles of NRs are still needed.

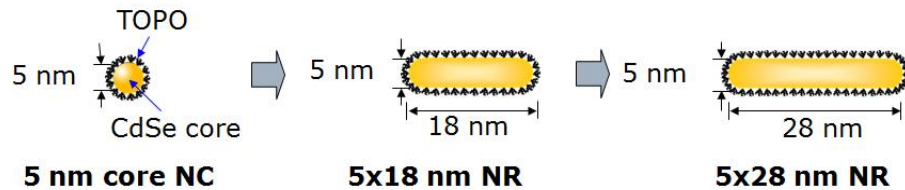


Figure 1.5 A diagram of elongated NRs in two different lengths and a NC with the same diameter.

Although a few studies used photon emission statistics [Brokmann 2003, Messin 2001] or spectral measurements [Issac 2005] to unambiguously identify single particles, most blinking studies rely on careful sample preparation from dropcasting extremely dilute nanocrystal solutions on the substrate and assume that well-dispersed nanoparticles result. In such studies, some blinking sources could in fact be clusters of a few particles. Therefore, a technique to correlate fluorescence to the number of particles is needed to investigate the mechanism of blinking further. Furthermore, with such a technique, it allows to investigate the possible interaction existing in clusters of NRs.

The random nature of CdSe blinking is a major obstacle to single-NC optoelectronic applications such as lasers [Chan 2004] and single-photon sources, [Brokmann 2004] as well as to using single NCs as biological fluorescent markers. [Bruchez 1998, Dubertret 2002] Consequently, understanding blinking may facilitate many applications.

In this dissertation, I will touch on aspects of blinking behavior of different types of NRs and study the possible interactions in small clusters. The first chapter introduces the background of the research of "blinking" from nanoparticles. Chapter 2 describes fluorescence blinking statistics measured from single CdSe NRs of different sizes and aspect ratios. Chapter 3 and 4 present the measurement of blinking statistics correlated with nanoparticle number, for small clusters (up to ~100 nanoparticles) and larger ensembles, respectively. Chapter 5 moves further into possible interactions in small

clusters. In particular, the collective behavior of enhancement of durations of on-times is investigated and compared to the combined fluorescence durations from the same number of independent nanoparticles.

Chapter 2

Fluorescence blinking statistics from CdSe core and core/shell nanorods

2.1 Introduction

Blinking in semiconductor NCs differs significantly from that observed in many other single fluorophores in the probability distribution of “on” or “off” events of a particular duration. As described in Chapter 1, the probability distribution function (PDF) of the off times, $P(t_{off})$, has been found to follow a power law for spherical core/shell CdSe/ZnS NCs,

$$P(t_{off}) = At_{off}^{-\alpha_{off}} \quad (\alpha_{off} \sim 1.5), \quad \text{Eq. 2.1}$$

where t_{off} is the duration of off times and α_{off} is a constant exponent.

Recently, NCs with anisotropic shapes have been synthesized.[Manna 2000] One example is the nanorod (NR) (Figure 1.5). The elongation of NRs also makes them better conductors than spherical NCs, and thus more suitable for certain device applications. [Huynh 2002, Millo 2004] In this chapter, it reports the study of blinking statistics from single CdSe NRs of different sizes with aspect ratios up to 11, and with different degrees of surface passivation. For four sizes of NRs, we studied both core CdSe and core/shell CdSe/ZnSe NRs; for a particular size of NRs, 5.2nm×28nm, we studied core NRs with two different surface ligands, trioctylphosphine oxide (TOPO) and hexadecylamine (HDA), which produce different degrees of surface passivation, allowing us to distinguish the effects of surface passivation and shape on the blinking statistics. Unlike

the off-time distribution, the distribution for on-times follows a power law for short on times, and falls below the power law for longer on times. To better match the shape of the on-time distributions, we fit them to a truncated power law,

$$P(t_{on}) \sim t_{on}^{-\alpha_{on}} e^{-t_{on}/\tau_c^{on}}, \quad \text{Eq. 2.2}$$

where t_{on} is the duration of on times, α_{on} is the constant exponent and τ_c^{on} represents the crossover time between the power law regime and the decay. Finally, we investigate the effect of excitation intensity and absorption cross-section on the on- and off-time statistics to gain further insight into NR blinking.

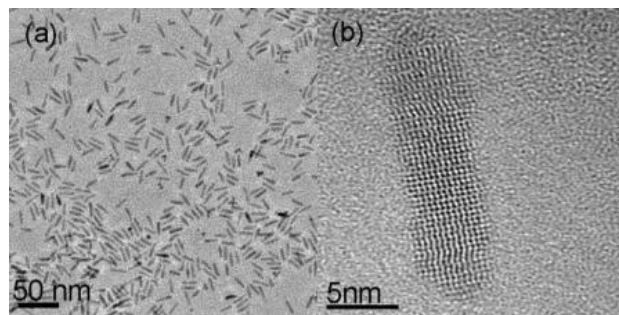
2.2 Experimental Methods

2.2.1 Samples of CdSe NRs

We synthesized CdSe NRs of different lengths and diameters (Table 2.1), capped with a 1.1 nm layer of TOPO, by adapting literature procedures.[Peng 2001, Peng 2002, Shieh 2005] A ZnSe shell was grown on some of the core samples according to [Reiss 2002]; HDA-capped NRs (NR5-HDA in Table 2.1) were prepared by heating TOPO-capped NRs in HDA for 1 h and precipitating/washing with methanol. Transmission electron microscopy (TEM, JEOL 2010F) confirmed the monodispersity (Figure 2.1a) and crystallinity (Figure 2.1b) of the NRs. Spherical CdSe and core/shell CdSe/ZnS NCs with core diameters of 5.2 nm were purchased from Evident Technologies. The samples studied are listed in Table 2.1. Core/shell NC and NR samples in this chapter are named according to the core on which the shell was grown followed by “cs”, e.g., NR1cs.

Table 2.1 Characteristics of CdSe core of samples used in this study.

Sample	d (nm)	l	d/l^a	A (nm 2) b	V b	$N_{\text{TOPO}}/N_{\text{CdSe(surf)}}^c$	σ_λ (nm 2) d	σ_{532} (nm 2) d
NC	5.2	-	1	85	74	49	2.7	2.6
NR1	3.4	18	5.3	192	153	45	5.3	4.0
NR2	3.5	25	7.1	275	229	42	6.7	5.0
NR3	3.4	38	11.2	406	335	42	7.9	6.1
NR4	5.2	18	3.5	295	345	37	8.0	8.9
NR5	5.2	28	5.4	457	558	36	8.3	9.6
NR6	6.4	22	3.5	442	639	34	9.6	19
NR7	6.9	34	4.9	737	1185	32	14	30

^a Diameter (d), length (l), and aspect ratio (d/l) determined from the absorption spectra and TEM analysis.^b Surface area (A) and volume (V) estimated from the dimensions of the particles assuming perfect sphere or rod shape including a cylinder with half-sphere ends.^c Coverage of available CdSe surface sites with TOPO molecules estimated from the ligand volume according to the procedure described by Bullen and Mulvaney. [Bullen 2006]^d Absorption cross-section at the excitonic peak (σ_λ) and at 532 nm (σ_{532}).**Figure 2.1** (a) Low-resolution and (b) high-resolution TEM images of 5.2×18 nm NRs deposited on thin films of amorphous carbon supported by a copper grid.

2.2.2 Measurement of the absorption cross-section σ_λ

We prepared a series of concentrations of dispersions of NCs and NRs in toluene, including at least seven different concentrations between $\sim 5 \cdot 10^{-8}$ and $\sim 5 \cdot 10^{-6}$ mol·L $^{-1}$ (maximum concentration of $6 \cdot 10^{-7}$ mol·L $^{-1}$ for NR6 and NR7). Absorption spectra were measured using a USB2000-VIS-NIR spectrometer (Ocean Optics; integration time, 30 ms; resolution, 1 nm; path length, 1 cm). A Beer's law plot of the absorbance intensities at the excitonic peak and at 532 nm (the laser wavelength used to excite fluorescence) was made to determine the molar extinction coefficients, ε_λ . The per particle absorption cross section, σ_λ , was then calculated according to [Leatherdale 2002] (Table 2.1).

2.2.3 Fluorescence Measurement

We performed wide-field fluorescence imaging (Figure 2.2) [Moerner 2003] of a very sparse sample of NCs or NRs, using an epifluorescence microscope (Olympus) with a 100×0.95 NA dry objective. Samples were prepared by drop- or spin-casting a very dilute toluene solution of CdSe NCs or NRs onto a freshly cleaved mica substrate. The concentration of the solution was chosen so that individual NCs or NRs were typically separated by a few micrometers. The sample was illuminated by 532 nm light from a continuous-wave (cw) frequency-doubled YAG laser (Coherent Compass). The excitation intensity used for most measurements in this chapter was $210 \text{ W}\cdot\text{cm}^{-2}$. In measurements for studying intensity dependence, the intensity was varied from 90 to $1000 \text{ W}\cdot\text{cm}^{-2}$. All samples were measured at room temperature in air immediately after preparation to minimize sample oxidation. Fluorescence movies were captured by a thermoelectrically cooled CCD camera (Princeton Instruments Cascade 512F) at 10 frames per second. All measurements presented in this chapter lasted 2000 seconds unless otherwise specified. A background image measured from a clean mica substrate was subtracted from each frame of the movies. Individual emitters were identified in the image acquisition software, and the fluorescence intensity, $I(t)$, of each emitter was determined in each frame throughout the entire movie. The mechanical stability of our setup with a drift of 100 nm/h allowed us to trace the fluorescence dynamics for many hours. For data (2000 seconds) in this chapter, the mechanical drift was small enough (much less than one pixel size, ~ 150 nm) to be ignored. For data with many hours in the following chapters, the small mechanical drift was accounted for by offsetting the position of the recorded frames appropriately during data analysis.

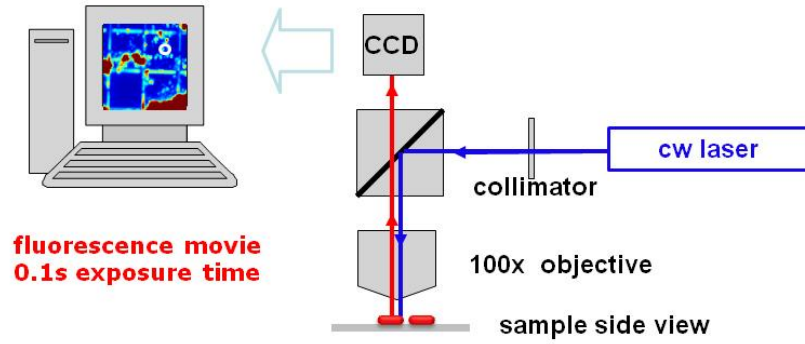


Figure 2.2 Schematic of the wide-field fluorescence imaging setup using an upright epi-fluorescence microscope.

2.3 Results and Discussion

2.3.1 Statistical analysis of fluorescence on- and off-times

Figure 2.3a shows an example of the time-dependent fluorescence intensity, $I(t)$, measured for 2000 second from a single 5×18 nm NR (NR4). To define the threshold above which the NR is considered on, we measured $I(t)$ in ten "dark" regions (*i.e.*, regions with no NRs), near the blinking NR and found the greatest intensity range, ΔI_{dark} (*i.e.*, the difference between the maximum and minimum intensity), and its standard deviation, σ_{dark} , represented among those ten. The threshold for on-times (solid line) for each NR was set by adding $\Delta I_{dark} + \sigma_{dark}$ to the minimum intensity measured from that NR (dotted line), as shown in Figure 2.3a.

From $I(t)$ of a single NR, we can determine the PDF of off (on) events of duration $t_{off(on)}$. The PDF is commonly defined as

$$P(t_{off(on)}) = \frac{N(t_{off(on)})}{N_{off(on)}^{tot}} \times \frac{1}{\Delta t}, \quad \text{Eq. 2.3}$$

where $N(t_{off(on)})$ is the number of off (on) events of duration $t_{off(on)}$, $N_{off(on)}^{tot}$ is the number of all off (on) events observed from that NR, and Δt is the 100 ms frame duration of the

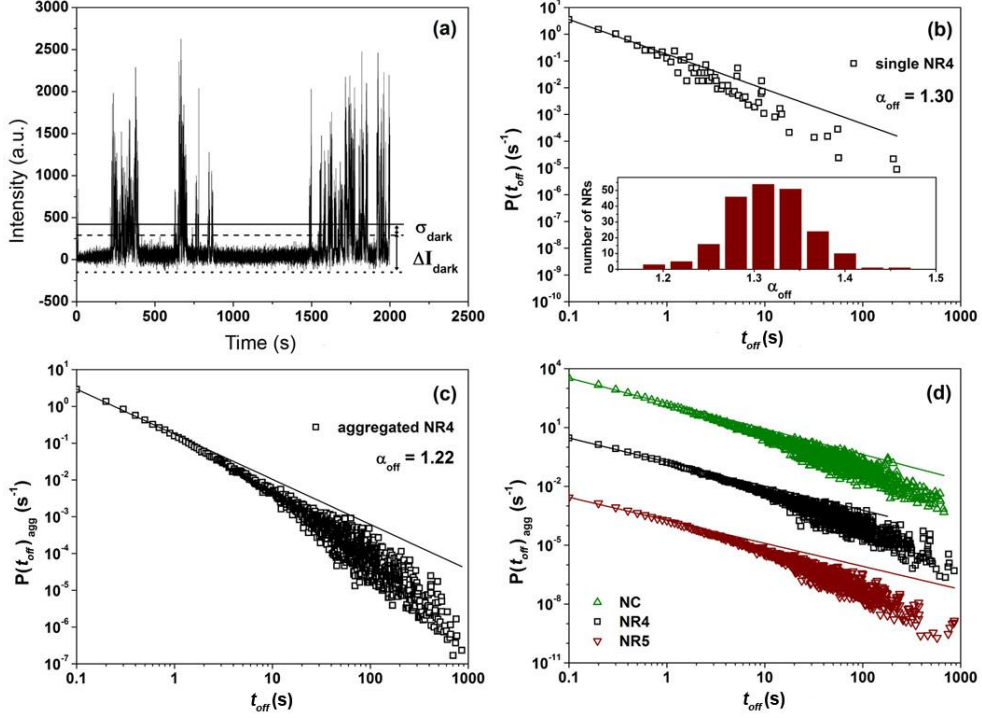


Figure 2.3 a) Representative intensity vs. time data, $I(t)$, obtained from a single NR (sample NR4) with the threshold above which it is considered to be on, indicated by the solid line. b) Off-time probability density, $P(t_{\text{off}})$, obtained from the data shown in (a). Inset: Histogram of exponents, α_{off} , for best-fit power law for each of 210 individual NRs observed in this sample. c) Aggregated probability density of off-times, $P(t_{\text{off}})_{\text{agg}}$, obtained by combining all off-times from all individual NRs observed. d) Comparison of $P(t_{\text{off}})_{\text{agg}}$ obtained from NC (green upright triangles), NR4 (black squares), and NR5 (red inverted triangles), offset vertically by multiples of three decades for clarity. The parameters of the best-fit power law (solid lines) are provided in Table 2.2.

movies. One problem with Eq. 2.3 is that it assigns the same probability density to any $t_{\text{off}(on)}$ occurring only once during a particular experiment, and assigns a probability of zero to any $t_{\text{off}(on)}$ not observed in that experiment. In other words, the probability density calculated using Eq. 2.3 for these rare events is not accurate. To account for this problem, we calculate a weighted probability density according to the method of Kuno *et al.* [Kuno 2001]:

$$P(t_{\text{off}(on)}) = \frac{N(t_{\text{off}(on)})}{N_{\text{tot}}^{\text{off}(on)}} \times \frac{1}{\Delta t_{\text{off}(on)}^{\text{ave}}}, \quad \text{Eq. 2.4}$$

defining $\Delta t_{\text{off}(on)}^{\text{ave}} = (a+b)/2$, where a and b are the time differences to the next longest and next shortest observed event. For common event durations, a and b are both equal to

Table 2.2. Off-time (on-time) exponents $\alpha_{off(on)}$ and on-time crossover times τ_c^{on} obtained for CdSe core and core/shell NCs and NRs.^a

Sample	α_{off}^b	α_{on}^c	τ_c^{on} (s) ^c
NC	1.30	1.32	4.6
NR1	1.17	1.18	0.60 ^d
NR2	1.08	0.96	0.36 ^e
NR3	1.16	0.98	0.44 ^d
NR4	1.22	1.10	1.1
NR5	1.17	1.17	0.88
NR6	1.23	1.05	1.0
NR7	1.20	0.93	0.62
NCcs	1.34	1.35	7.1
NR1cs	1.18	1.12	0.66
NR2cs	1.17	1.14	0.50
NR3cs	1.17	1.2	0.59
NR5cs	1.22	1.10	0.95 ^f
NR5-HDA	1.22	1.02	0.66

^a The fits were performed on aggregated data of 100 nanoparticles. Except when otherwise specified, data were obtained from movies 2000 s long.

^b Off-time exponent obtained from a power law fit (Eq. 2.1).

^c On-time fitting parameters obtained from a truncated power law fit (Eq. 2.2). The average uncertainty in the values of τ_c^{on} was 20%.

^d 1200 s long movie (uncertainty +30%/-20%).

^e 600 s long movie (uncertainty +40%/-30%).

^f Mean value of two independent measurements. Determination of uncertainties is discussed in Section 2.5.3.

the 100 ms frame duration and so $\Delta t_{off(on)}^{ave} = 100$ ms; $\Delta t_{off(on)}^{ave}$ increases for rare events

where a or b exceeds 100 ms. This weighting scheme gives a better approximation to the true probability density of these rare events.

Previous studies [Kuno 2000, 2001, Shimizu 2001] have used different approaches to fit their off-time PDF to a power law. We tried all these approaches for our data set obtained from the core/shell NCs (NCcs) (fits and discussion are provided in Supplementary Information 2.5.1). Depending on the fitting approach used, the same off-time data gave a power law exponent ranging from 1.34 to 1.87. For all analysis in this chapter, we binned our data by the 100 ms frame duration and fit $P(t_{off})$ to the power law $A t_{off}^{-\alpha_{off}}$ (rather than fitting a line to $\log[P(t_{off})]$ vs. $\log[t_{off}]$). This approach gave

somewhat (20 – 30%) smaller exponents than other methods. We chose this approach because it minimizes data manipulation, and the fits gave more weight to the most reliable (short duration) points in the probability distribution.

2.3.2 Off-time statistics

The off-time probability density $P(t_{off})$ extracted from the $I(t)$ data in Figure 2.3a is shown on a log-log scale in Figure 2.3b. Similar distributions were obtained for each of the 210 individual NRs in this sample (NR4). The combined probability density of all events from all NRs (the “aggregated” probability density, $P(t_{off})_{agg}$) is shown in Figure 2.3c. Both $P(t_{off})_{agg}$ and $P(t_{off})$ for individual NRs were described by a power law though the longest off-times fall slightly below the power law. For the NR shown in Figure 2.3b, the best fit gave $\alpha_{off} = 1.30$; the distribution of exponents obtained from 210 individual NRs (inset to Figure 2.3b) had an average value of 1.3 and a standard deviation of 0.1. The power law fit to the aggregated results (Figure 2.3c) gave $\alpha_{off} = 1.22$, which is within one standard deviation of the average α_{off} of individual NRs. We therefore estimated the uncertainty in α_{off} from the aggregated data to be 0.1, the standard deviation of the distribution, and concluded that the aggregated probability distribution is consistent with the range of individual probability distributions observed.

To investigate the effect of NR shape and surface passivation on blinking, we studied the blinking statistics for all fourteen samples (listed in Tables 2.1 and 2.2). The aggregated off-time probability distributions for the 5.2 nm diameter core NC and NRs, *i.e.* NC, NR4, and NR5, are shown in Figure 2.3d. All distributions showed power law behavior, with the longest off times falling slightly below the power law.

α_{off} obtained from the best power law fit to the aggregated data of different samples (Table 2.2) showed no significant dependence on the NR aspect ratio, the presence of a ZnSe shell, or the type of surface ligands; all values for NRs ($\alpha_{off} = 1.08$ to 1.22) fell within the uncertainty range of 0.1 as discussed early. The values obtained for the spherical NCs (core and core/shell) were slightly higher ($\alpha_{off} = 1.30$ and 1.34).

2.3.3 On-time statistics

Although the off-time distributions of NRs and NCs were essentially indistinguishable and independent of shape and surface passivation, their on-time distributions showed a

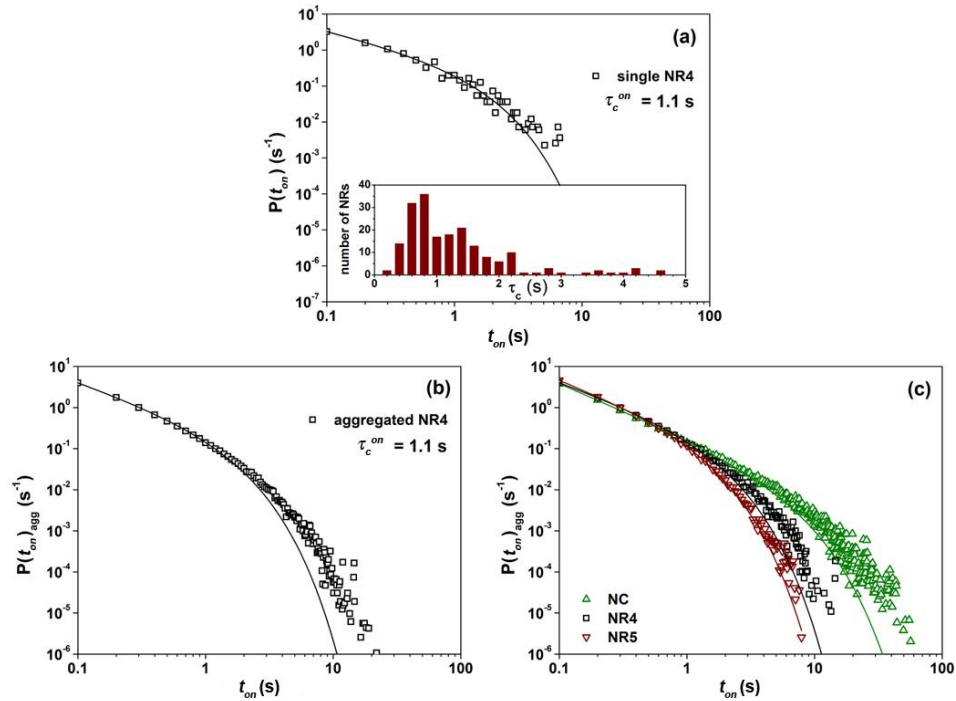


Figure 2.4 a) On-time probability density $P(t_{on})$ obtained from the data shown in Figure 2.3a. Inset: Histogram of crossover times τ_c^{on} for the best-fit truncated power law for each of 210 individual NRs observed (sample NR4). b) Aggregated on-time probability density $P(t_{on})_{agg}$ obtained by combining on-times from all individual NRs observed. c) Comparison of $P(t_{on})_{agg}$ obtained from NC (green upright triangles), NR4 (black squares), and NR5 (red inverted triangles). The parameters of the best-fit truncated power law (solid lines) are catalogued in Table 2.2.

distinct dependence on aspect ratio. Figure 2.4a shows the on-time probability density for the single NR from the NR4 data in Figure 2.3a; the aggregated probability density for all NR4 is plotted in Figure 2.4b. The on-time distributions obtained from other samples have a shape similar to that in Figure 2.4b they all followed a power law for on-times up to roughly 1 s for NRs and 5 s for NCs, and fell below the power law for longer on-times, which was consistent with previous findings for NCs. [Kuno 2000, 2001, Shimizu 2001]

To better match the shape of the on-time distributions, we fit them to a truncated power law, $P(t_{on}) = At_{on}^{-\alpha_{on}}e^{-t_{on}/\tau_c^{on}}$, shown by the curves in Figure 2.4. This function can be used to describe a physical process that is governed by a power law at short times and by an exponential decay at long times, as has been proposed for NC blinking.[Chung 2004, Tang 2005 a, b, c] the parameter τ_c^{on} represents the crossover time between the two regimes. This function fit the on-time distributions well for both individual and aggregated data, and the χ^2 of the fits was usually one hundred times smaller than that of a pure power law (Eq. 2.1).

We also examined whether a stretched exponential probability distribution, $P(t_{on}) = A \exp(-t_{on}/\tau_c^{on})^{-\beta}$, fits the on-time distributions (fits not shown), because stretched exponential probability distributions were predicted from some models of disordered systems. [Leatherdale 2002] However, the χ^2 of these fits were much larger than those obtained using a truncated power law, and were comparable to those obtained using a pure power law. More significantly, the parameter τ_c^{on} varied by two orders of magnitude among individual NRs or NCs of the same type, rather than displaying consistent values, as in the case of a truncated power law.

A comparison of on-time distributions obtained from experiments with different durations (shown in Supplementary Information 2.5.2) indicated that increasing the experiment duration, so that more long-time events are observed, produced an on-time distribution that increasingly resembled the distribution obtained by aggregating many shorter measurements. In addition, the histogram of crossover times calculated for individual NRs narrows, with the peak value staying the same within experimental uncertainty (Supplementary Information 2.5.3), and with the number of long crossover-time outliers greatly reduced. We therefore concluded that aggregated distributions, if enough NRs are included, served as a reasonably good approximation to the distribution that would be obtained from measurements with an extremely long duration. Since performing such measurements on single NRs or NCs was difficult, we therefore focused our analysis on aggregated data from many individual NRs, and used the distributions of crossover times of individual rods to determine the uncertainty in the value obtained from the aggregated data, as described in Supplementary Information 2.5.3.

Blinking of NRs exhibited many similar features as that of spherical NCs: the off-time distribution followed a power law that is independent of excitation intensity or sample shape, and the on-time distribution followed a truncated power law with an intensity-dependent crossover time τ_c^{on} . On the other hand, there were also significant differences between NR and NC blinking. In particular, τ_c^{on} was substantially shorter for NRs than for NCs, *i.e.*, NRs displayed far fewer long on-time events, and among a variety of NRs. For the 5.2 nm diameter core samples (Figure 2.4c), we obtained the shortest crossover time, 0.89 s, for the longest NR (NR5); τ_c increased to 1.1 s for the shorter NR (NR4) and finally to 4.6 s for the NC. The corresponding exponents α_{on} were slightly

smaller for NRs ($\alpha_{on} \sim 1.2$) than for NCs ($\alpha_{on} \sim 1.3$), but showed no significant dependence on NR length or surface passivation, as shown in Table 2.2.

Several important structural differences between NRs and NCs might have caused these differences. Firstly, NR surfaces are less sharply curved along its long dimension than the surface of spherical NCs or the ends of NRs. As a result, a lower percentage of surface coverage by the TOPO capping layer is expected for NRs, since TOPO molecules are conical. [Beadie 1995] Therefore the density of unpassivated surface traps in NRs should be larger than that of NCs, which may reduce the lifetime of on states. Second, quantum confinement of charge carriers in 1D NRs is weaker than that in 0D spherical NCs. Consequently, the barrier through which excited charge carriers can tunnel to the surface or into the environment is smaller in NRs than in NCs. [Chen 2001, Rothenberg 2004] The greater likelihood of such tunneling events would likewise be expected to reduce the probability of long on-times. Finally, the shorter crossover time in NRs might also be a consequence of their higher surface charge density . [Bullen 2006, Klimov 2000]

2.3.4 Effect of ligands

Figure 2.5 shows on-time distributions from the three types of 5×28 NRs with different surface passivation (NR5, NR5cs, and NR5-HDA). Equivalent data were obtained for all 14 samples in our study (Table 2.2).

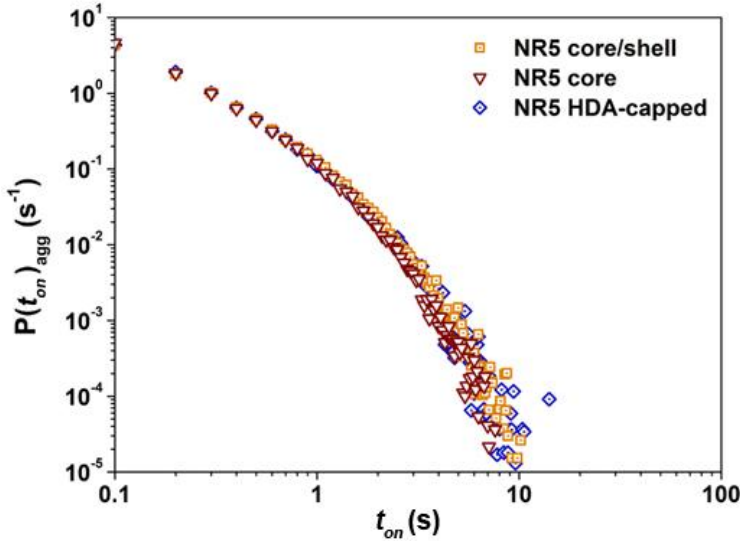


Figure 2.5 Aggregated on-time probability distributions for NR5cs (orange squares), NR5 (red inverted triangles), and NR5-HDA (blue diamonds), obtained from 100 NRs for each sample at $210 \text{ W}\cdot\text{cm}^{-2}$. Best-fit exponents and crossover times are provided in Table 2.2.

Surprisingly, we found the same on-time distribution and crossover time (within experimental uncertainty) for the core and core/shell $5\times28 \text{ nm}$ NRs (NR5 and NR5cs), as shown in Figure 2.5 and Table 2.2, in spite of a significant improvement in fluorescence quantum yield and resistance to photobleaching displayed by core/shell NRs. We also found very little difference between the core NRs capped with TOPO and with HDA, NR5 and NR5-HDA (Figure 2.5), in spite of an expected threefold difference in surface coverage. HDA was expected to attach to nearly all surface CdSe units while TOPO to only $\sim 36\%$. This is because HDA has a linear geometry while TOPO has a cone-shaped geometry. [Beadie 1995]

In core/shell NRs, the optically active core is almost perfectly passivated by the semiconductor shell that has a larger band gap. Lattice mismatches between the two crystal structures can introduce defects; however, this is not the case for ZnSe and CdSe since they are very well lattice-matched. [Krauss 1999] In core NRs, the surface is only passivated by the organic capping ligands, and the degree of passivation depends strongly

on the type of ligand. The linear shape of HDA molecule allows it to attach to nearly all CdSe surface sites, while TOPO attaches to less than half of the surface units. The samples compared thus represent a wide range of surface passivation.

We did find, however, that core/shell spherical NCs had a somewhat greater crossover time than the corresponding core NCs (Table 2.2). One possible explanation for why the crossover time of NRs but not NCs is insensitive to surface passivation is that in NRs, internal trap states, such as those induced by stacking faults in the crystal structure during growth, may have much more significant effects on carrier dynamics than surface trap states do. If so, improved surface passivation in NRs would not change the crossover time substantially.

2.3.5 Effect of aspect ratio

By examining data of NRs with different shapes, we found a single clear trend in the crossover time: τ_c^{on} decreased steadily with increasing NR aspect ratio. Quantitatively, it appeared that $1/\tau_c^{on}$ increases approximately linearly with NR aspect ratio, as shown in Figure 2.6. The uncertainty in τ_c^{on} was determined from repeated measurements and from the distribution of τ_c^{on} values of the individual NRs, as described in Supplementary Information 2.5.3. We found that the variation of α_{on} is larger than that of α_{off} , but with no clear trend.

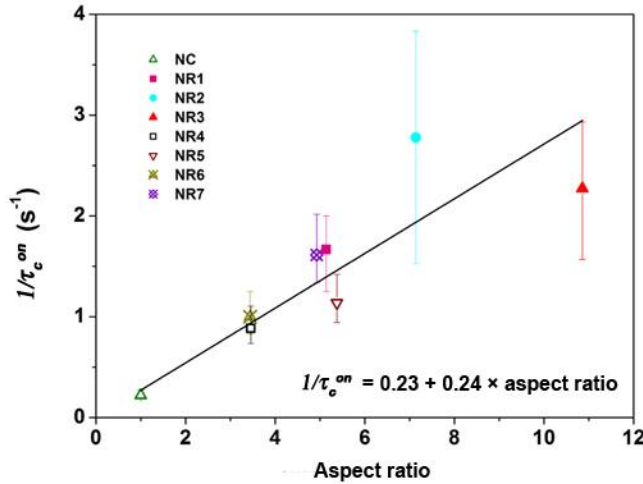


Figure 2.6 Inverse crossover time *vs.* aspect ratio for all TOPO-capped core NC and NR samples studied, along with best-fit line, $1/\tau_c^{on} = 0.23 + 0.24 \times \text{aspect ratio}$.

By comparing the crossover times (Table 2.2) measured for the 5.2 nm diameter NRs (NR4 and NR5) to those for the 6.4 and 6.9 nm diameter NRs (NR6 and NR7), we observed that for comparable lengths, a larger diameter reduced the crossover time. This was consistent with previous results from spherical NCs. [Shimizu 2001] Unexpectedly, the 3.5 nm-diameter NRs (NR1 through 3) showed smaller rather than larger crossover times, compared to the 5.2 nm diameter NRs. The 3.5 nm diameter NRs also bleached more rapidly than the larger NRs, leading to shorter data acquisition times, which resulted in larger uncertainties in τ_c^{on} , as indicated in Table 2.2.

The approximate linear relation between $1/\tau_c^{on}$ and the aspect ratio (Figure 2.6) could therefore be a manifestation of reduced quantum confinement due to increasing aspect ratio. If so, it also reveals that the transition from 0D to 1D confinement has a much greater effect on the crossover time than decreasing confinement by increasing the diameter of spherical NCs. It could also reflect an increased number of internal trap states with increasing aspect ratio, or both effects could contribute. We postulate that changes

in quantum confinement with NR aspect ratio may play a significant role and should be considered in future models.

2.3.6 Effect of excitation intensity

Finally, we examined the effect of the intensity of excitation on the NR off- and on-time statistics, by comparing blinking data of the 5×18 nm NRs (NR4) measured at eight different intensities from $90 \text{ W} \cdot \text{cm}^{-2}$ to $1000 \text{ W} \cdot \text{cm}^{-2}$. The off-time distribution was largely unaffected, as was found previously for spherical NCs. [Shimizu 2001]

The on-time distribution, on the other hand, showed an obvious trend with intensity change. Over the entire intensity range studied, the on-time distribution was well fit by a truncated power law. The theory of Tang and Marcus [Tang 2005a] predicts that $1/\tau_c^{on}$ should be proportional to the photon absorption rate, and hence for a particular

Table 2.3. Intensity dependence of off- and on-time parameters for sample NR4.^a

$I (\text{W} \cdot \text{cm}^{-2})^b$	α_{off}^c	α_{on}^d	$\tau_c^{on} (\text{s})^d$
90	1.27	1.09	1.3
210	1.23	1.10	1.1
300	1.29	1.01	1.1
400	1.24	0.92	0.79
500	1.22	0.79	0.73
600	1.21	0.79	0.69
690	1.14	1.16	0.69
870	1.12	1.20	0.65
1000	1.08	1.04	0.40

^a The fits were performed on aggregated data from 50 individual NRs.

^b Excitation intensity.

^c Off-time exponent obtained from a power law fit (Eq. 2.1).

^d On-time fitting parameters obtained from truncated power law fit (Eq. 2.2).

sample, proportional to the excitation intensity. As shown in Figure 2.7a, $1/\tau_c^{on}$ showed a small but steady increase with increasing intensity. The exponent from the truncated power law, α_{on} , also varied, but not in a consistent fashion (Table 2.3).

The variation of τ_c^{on} with excitation intensity raised a question: can the variation in τ_c^{on} with NR shape at a fixed intensity be attributed entirely to the change in photon absorption rate due to changes in the single-particle absorption cross-section? Indeed, our measurements of the single-particle cross-section at the excitation wavelength, σ_{532} , for each sample (Table 2.1) indicated that it increases with increasing NR volume, as has been found for spherical NCs. [Kuno 2001] To answer this question, we examined the variation in τ_c^{on} as the single-NR photon absorption rate is held constant.

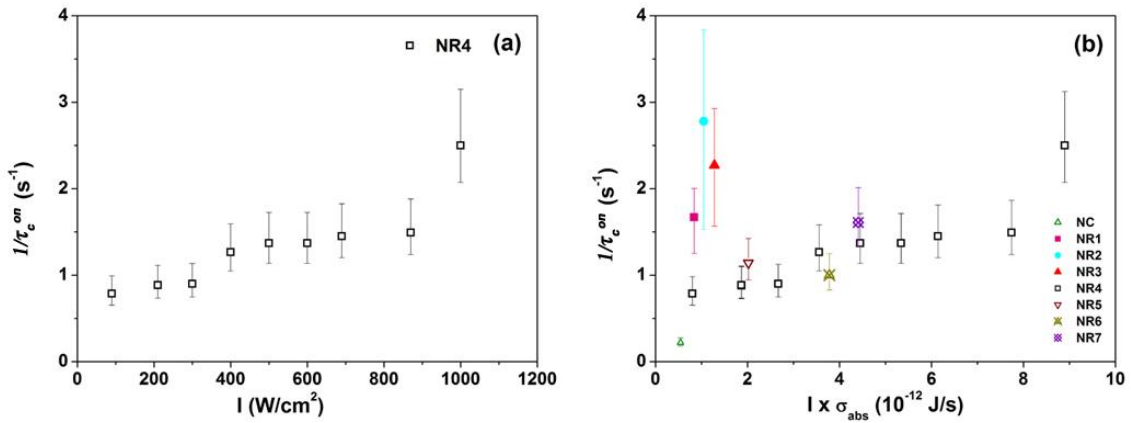


Figure 2.7 (a) Excitation intensity dependence of the inverse crossover time of NR4. Best-fit exponents and crossover times are provided in Table 2.3. (b) Inverse crossover times of measured core NRs and NC as a function of excitation intensity \times single-particle absorption cross-section (this quantity is proportional to the single-particle photon absorption rate).

Figure 2.7b shows $1/\tau_c^{on}$ vs. the product of excitation intensity and single-particle cross-section (proportional to photon absorption rate) for all core samples measured. Core/shell samples have essentially the same $1/\tau_c^{on}$ as the core samples of the same size. [Tang 2005a] The $1/\tau_c^{on}$ values obtained from the NRs with larger diameters (NR5, NR6, and NR7) were consistent with the measured intensity dependence of NR4, when intensity was converted to single-particle absorption rate. However, values obtained from the 3.5 nm diameter NRs (NR1 through 3) and the spherical NCs did not map onto the measured NR4 intensity dependence.

Our observation of a very gradual increase of $1/\tau_c^{on}$ with increasing excitation intensity (Figure 2.7a) is consistent with, though far less pronounced than, the intensity dependence of the on-time distribution observed in spherical NCs, which has previously been attributed to a reduced hopping rate at lower excitation intensities. [Shimizu 2001] The intensity dependence we observe for NR4, *i.e.* 5×18 nm NRs, is far weaker than that predicted by Tang and Marcus, [Tang 2005a] though it could be a linear relationship with a constant offset.

By studying $1/\tau_c^{on}$ as a function of photon absorption rate in different samples (Figure 2.7b), we find that changes in absorption cross-section can account for the dependence of $1/\tau_c^{on}$ on length for the NRs with larger diameters (NR4 through 7), which have fairly similar aspect ratios (3.5-5.5). However, $1/\tau_c^{on}$ for the spherical NCs and the NRs with a 3.5 nm diameter is different from that measured in the larger NRs with the same photon absorption rate. Our results therefore indicate that absorption cross-section changes cannot account for all of the observed variation in $1/\tau_c^{on}$.

2.4 Conclusions

In conclusion, we found that blinking statistics of CdSe NRs with a wide range of aspect ratios (3-11) display power law off-time statistics and truncated power law on-time statistics, with the crossover time for the on-time statistics decreasing with increasing aspect ratio and excitation intensity. We observed no significant difference in on-time statistics between core, core/shell, and HDA-capped core NRs, indicating that surface passivation had no major effect on NR blinking, while we saw a greater crossover time for core/shell than for core spherical NCs. We found that the variation in crossover times

with aspect ratio for NRs can be partly explained in terms of changes in the absorption cross-section and hence the photon absorption rate.

We therefore attributed the shorter crossover times in NRs with higher aspect ratios to a combination of a larger absorption cross-section, weaker quantum confinement, and possibly a higher density of internal trap states. In contrast to these differences in the on-time statistics, the off-time power law exponents do not depend on NR shape or surface coverage and are very similar for NRs and NCs. Consequently, the mechanism determining the off-times is most likely the same for NRs and NCs, while the light-induced mechanism affecting longer on-times begins at shorter times in NRs than in NCs and is less sensitive to surface passivation. These findings indicate that blinking poses significant limits on potential applications of NRs in optoelectronic devices, and that the behavior of NR-based devices may be particularly sensitive to excitation intensity.

2.5 Supplementary Information

2.5.1 Fitting methods of probability densities for off-times

Previous studies of blinking in core/shell NCs [Kuno 2000, 2001, Shimizu 2001] have used a variety of approaches to fit the off-time probability density to a power law. In order to find the best fitting approach, in this section, we applied all these different methods to our off-time probability density measured from the core/shell NCs with a diameter of 5.2 nm (NCcs, see Table 2.1), which were used in previous studies. By comparing results using different methods, we showed that the power law exponent depends significantly on the fitting approach used. We also argued that the variation of

this exponent reported in literature was partly due to the difference among the various ways of doing data analysis.

All the different approaches consist of two separate steps: calculating the probability density and fitting it to the power law. For the first step, the method involving the least data manipulation was to simply use the definition given in Eq. 2.3:

$$P(t_{off(on)}) = \frac{N(t_{off(on)})}{N_{off(on)}^{tot}} \times \frac{1}{\Delta t}, \text{ with } \Delta t \text{ being the time resolution of measurements.}$$

Subsequently fitting this off-time density to the power law $P(t_{off}) = At_{off}^{-\alpha_{off}}$, as shown in Figure 2.8a, gave $\alpha_{off} = 1.34$.

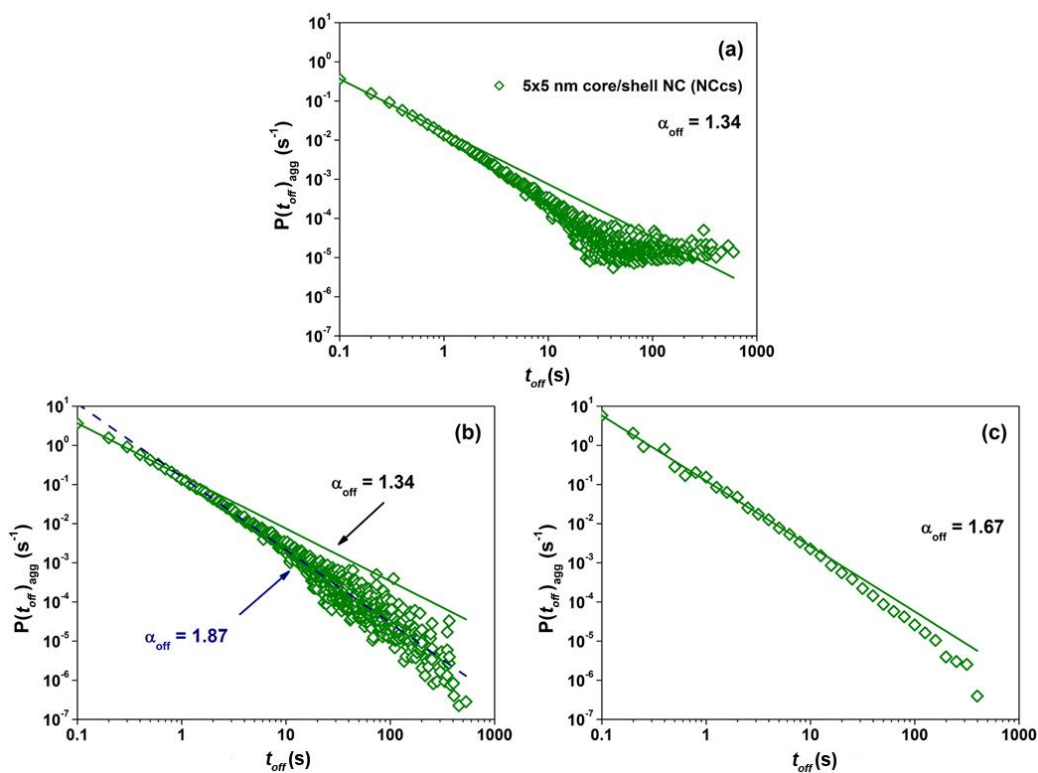


Figure 2.8 $P(t_{off})_{agg}$ obtained from 100 single NCcs. Solid lines indicate the best-fit power law. a) Unweighted distribution according to Eq. 2.3. b) Distribution weighting the rare events according to Ref. [Kuno 2001]. The dashed line represents the linear best-fit of the log-log plot. c) Distribution binned logarithmically. [Shimizu 2001]

As can be seen in Figure 2.8a, the distribution calculated in this fashion reached a plateau at large off-times, which was an artifact due to finite experiment duration. For

rare events that occur only a few times or not at all in a particular measurement, the probability calculated using Eq. 2.3 was not their true statistical probability. To overcome this shortcoming, Kuno *et al.* [Kuno 2000, 2001] introduced a weighting procedure, in which Δt was replaced by $\Delta t_{off(on)}^{ave} = (a+b)/2$, where a and b are the time differences to the next longest and next shortest observed events. This only affected rare events. Figure 2.8b shows the probability density obtained using this weighting scheme. Fitting this weighted probability density to a power law, we found $\alpha_{off} = 1.34$ (solid line in Figure 2.8b), the same as that obtained with the unweighted probability distribution. It is not surprising that the exponent was unchanged since the power-law fit was dominated by high-probability, short-duration points.

To further smooth the distribution, Shimizu *et al.* calculated the probability density from their data with only ten time bins in each decade of event duration; the length of the bins thus increased logarithmically. [Shimizu 2001] Binning our data in this manner greatly reduced the scatter (Figure 2.8c), and increased the best-fit power-law exponent to $\alpha_{off} = 1.67$.

As seen in Figure 2.8b, the low-probability, long-duration points in the off-time distribution fall slightly below the power law (though not enough for a truncated power law fit to be successful). In their analysis, Kuno *et al.* [Kuno 2000, 2001] calculated $\log[P(t_{off})]$ and $\log[t_{off}]$, and fit a line to the result. In such a fit (dashed line in Figure 2.8b), the longer-time events influenced the fit as much as the shorter-time events did, so the best-fit line was steeper ($\alpha_{off} = 1.87$ for our data), with the shortest-time points falling below the fit.

For data analysis in this chapter, we chose to bin our data by the 100 ms frame duration of the experiment, rather than using logarithmically increasing bins, to maximally preserve the measured results. We used Kuno's method to calculate weighted probability of rare events, which did not alter the resulting exponent. We also performed power-law fits to $P(t_{off})$ vs t_{off} directly instead of linear fits to $\log[P(t_{off})]$ vs $\log[t_{off}]$, since the power-law fit was dominated by short time events which represented the most reliable part of the probability distribution. These choices resulted in our off-time exponents being somewhat smaller than what would be obtained using either of the other two approaches reported in literature; the higher values obtained for our spherical NC data shown in Figure 2.8 were consistent with results of other groups.

2.5.2 Effect of experiment duration on individual NR on-time distributions

In order to check the validity of using aggregated data to determine crossover times, we compared on-time distributions obtained from measurements of 2000 s and 4000 s performed on the 5×18 nm NRs (NR4). Figure 2.9a shows that the longer measurements included more long-duration events and produced an on-time distribution that increasingly resembles that obtained by aggregating data from many shorter measurements. Figure 2.9b shows that the histogram of crossover time of individual rods narrowed as the experiment lengthens, while the peak value stayed essentially the same (within experimental uncertainty). In addition, when fitting data of individual NRs to the truncated power law, out of 100 NRs observed for 2000 s, five had crossover times

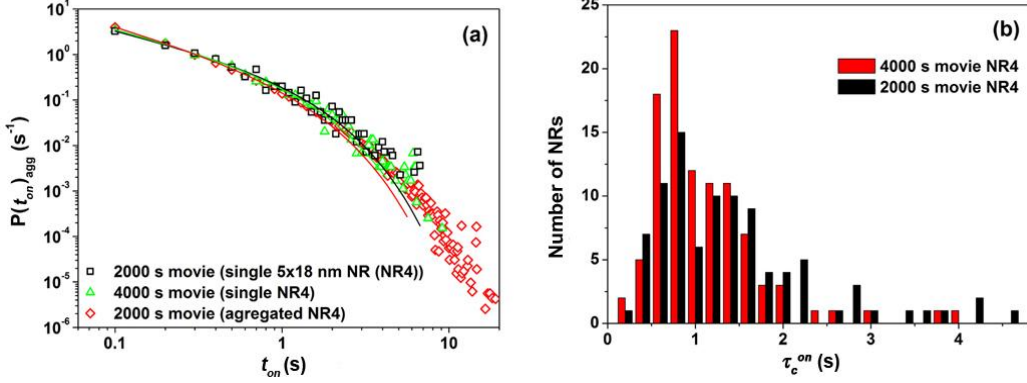


Figure 2.9 a) On-time probability distributions obtained from a single 5×18 nm NR (NR4) measured for 2000 s (black squares) or 4000 s (green triangles), and aggregated from 210 NRs measured for 2000 s (red inverted triangles). b) Histograms of crossover times τ_c^{on} obtained from 100 NRs measured for 2000 s (black) or for 4000 s (red). Fits to the probability distributions for five of the NRs measured for 2000 s gave $\tau_c^{on} > 4.5$ s, which do not appear on the graph above, and the fits of two NRs did not converge, while all of those measured for 4000 s gave fits that converged with $\tau_c^{on} < 4$ s.

greater than 4.5 s, and the fit failed to converge for 2 NRs. For 100 NRs observed for 4000 s, all fits converged and yielded crossover times less than 4 s, indicating that lengthening the experiment time aided convergence of blinking statistics results.

2.5.3 Determination of uncertainty in τ_c^{on}

We estimated the uncertainty in τ_c^{on} using several different approaches. Because τ_c^{on} in Tables 2.2 and 2.3 was determined from data aggregated from an ensemble of NRs or NCs, it had uncertainty because of the limited number of samples and the variation among individual NRs or NCs in each sample. Two independent measurements of τ_c^{on} for the 5×28 nm core/shell NR (NR5cs) on two separated chips, each determined from a fit to aggregated data from 100 single NRs, gave 0.88 s and 1.02 s. Figure 2.10a shows the histogram of τ_c^{on} values of individual NR5cs in the data set that gave the mean of 0.97 s, and the standard deviation of 0.6 s. Considering both the two independent aggregated measurements and the histogram of individual measurements, the uncertainty in τ_c^{on} was

approximately 0.1 s, or 10%. Another way to determine the uncertainty was by aggregating 100 NRs randomly selected out of 210 NR4; repeating this process 200 times gave τ_c^{on} values between 0.99 s and 1.30 s. We therefore attributed an uncertainty of 20% to the value of τ_c^{on} obtained by aggregating data from 100 NRs each measured for 2000 seconds. Considering the uncertainties found by different methods, we then took the larger value, 20%, as the uncertainty of the value of τ_c^{on} .

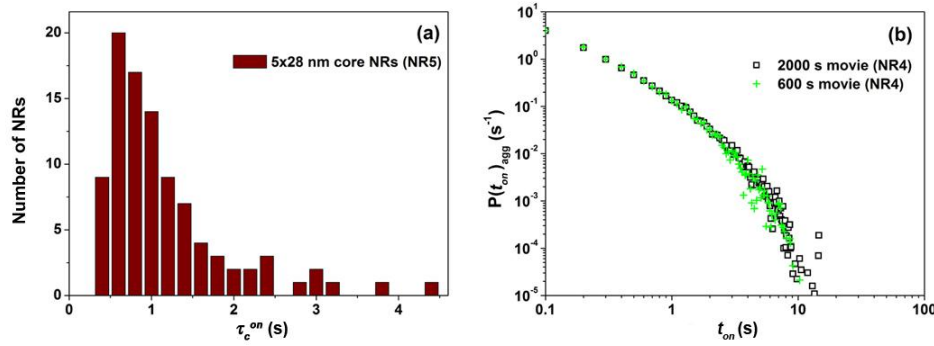


Figure 2.10 a) Histogram of truncation times obtained for NR5. b) On-time distributions obtained from (black square) 2000 s movie and (green cross) 600 s excerpt from same 2000 s movie of NR4.

For the NRs with a diameter of 3.5 nm, we measured fluorescence for only 1200 s or (for the 3.5×25 nm NR, *i.e.* NR2) 600 s due to rapid photo-bleaching of the samples, which increased the uncertainty in τ_c^{on} . To estimate this uncertainty, we analyzed a 600 s excerpt from a 2000 s movie of NR4. Figure 2.10b showed the on-time distributions obtained from the full movie and the excerpt; for the shorter dataset, the overall distribution was noisier at large on times (though nearly identical for small on times), and τ_c^{on} decreased by 20%. We therefore used error bars of +40% and -30%, with the larger positive error bar indicating the likelihood that the value of τ_c^{on} was underestimated for 600 s experiments. Following the same procedure with a 1200 s excerpt gave us an uncertainty estimate of +30% and -20% for the 1200 s movies.

Chapter 3

Blinking statistics correlated with nanoparticle number

3.1 Introduction

Previous work [Cichos 2007, Frantsuzov 2008] on blinking in quantum dots focused on single emitters and ensembles of independent emitters without identifying the exact number of NRs. Although a few experiments used photon emission statistics [Messin 2001, Brokmann 2003] or spectral measurements [Issac 2005] to unambiguously identify single particles, most blinking studies relied on careful sample preparation by using extremely dilute nanoparticle solutions and assuming that well dispersed nanoparticles would result. In such studies, some blinking sources could in fact be clusters of a few particles. Recently, fluorescence from clusters of close-packed spherical nanocrystals (NCs) was observed to fluctuate more rapidly than isolated NCs blinking independently; the fluorescence from single emitters and clusters displayed distinguishable autocorrelation functions. [Yu 2006] By correlating fluorescence data and atomic force microscopy, the authors were able to determine the effective volume of the clusters, but not the number of or distance between particles in the clusters. In this chapter, we correlated fluorescence image to transmission electron microscopy (TEM) to determine the number and arrangement of CdSe nanorods (NRs) within each fluorescent source. This approach [Koberling 2002] allowed for high resolution imaging and direct particle counting.

In chapter two, we pointed out that NRs and spherical nanocrystals share some common features in their blinking: the distribution of off-times follows a power law while the distribution of on-times follows a truncated power law $P(t_{on}) \propto t_{on}^{-\alpha_{on}} e^{-t_{on}/\tau_c^{on}}$, where α_{on} is the power-law exponent and τ_c^{on} is the truncation time. The primary difference, however, is that τ_c^{on} is smaller for NRs (~ 1 - 10 s) than for spherical NCs (typically > 10 s). In addition, NRs with larger aspect ratios usually have smaller τ_c^{on} values, which is a consequence of a larger absorption cross section, weaker quantum confinement, and possibly a higher density of internal trap states in these NRs. [Wang 2006]

In this chapter, we present the fluorescence intensity *vs.* time, $I(t)$, of NR clusters containing 1 to 15 NRs. TEM images of these clusters were used to determine their number of particles, N , the distance between NRs, d , and the angle of NRs, θ , relative to each other and to the laser polarization direction. We found that samples drop-cast on low stress silicon nitride (Si_3N_4) membranes from dilute solutions with concentration $\sim 10^{-9}$ mol·L⁻¹ were mostly comprised of individual emitters, but $\sim 25\%$ of blinking sources corresponded to clusters of particles. Clusters consisting of two or three NRs exhibited fluorescence intermittency similar to that of individual NRs and we showed that probability density analysis cannot unambiguously distinguish between individual NRs and such small clusters. Clusters of ~ 5 or more particles were clearly distinguishable by their longer truncation times of the on-time probability densities, τ_c^{on} , and their emission intensity. The very long fluorescence measurements ($\sim 2.4 \times 10^4$ s) also allowed us to directly observe the truncation time to the Lévy distribution of the off-times.

3.2 Experimental Methods

For the study reported in this chapter, we used NRs for this correlation study rather than spherical NCs partly because the elongated NR shape made it easier to unambiguously distinguish isolated NRs from the background features of the substrate in TEM images. Additionally, NRs had a lower surface to volume ratio than NCs with the same diameter, making them more robust against photobleaching, and had a higher absorption cross section than NCs with the same emission wavelength. We used TOPO-capped CdSe/ZnSe/ZnS core/double shell semiconductor NRs (see Supplementary Information 3.5.1), with a 5.8×34 nm optically active CdSe core and an overall size of 8×38 nm.

Low stress silicon nitride (Si_3N_4) membranes [Fischbein 2006] with a thickness of 50 nm were used as substrates because they are transparent to electrons in TEM and contribute a negligible fluorescence background. [Koberling 2002] Gold markers, to aid in locating NRs, were fabricated on the membranes using electron beam lithography (Figure 3.1).

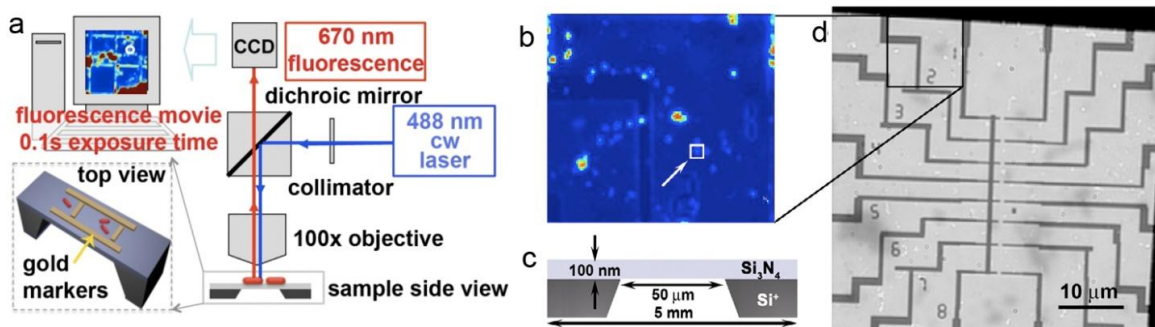


Figure 3.1 a) Schematic of the wide-field fluorescence imaging setup using an upright epi-fluorescence microscope. b) Fluorescence micrograph of a $\sim 10 \times 10 \mu\text{m}^2$ region, where a blinking movie was taken. The arrow indicates the location of the two NRs shown in **Figure 3.4b**. c) Schematic (side-view) of the Si_3N_4 substrate. d) TEM of the transparent window region ($\sim 50 \times 50 \mu\text{m}^2$) patterned with gold markers. The rectangle indicates the area of the fluorescence image. The dark border is the membrane region on top of the p-doped Si that is not TEM-transparent.

Solution of NRs dispersed in toluene ($10^{-9} \text{ mol} \cdot \text{L}^{-1}$) was deposited onto the substrate by drop-casting (1 μL). Wide-field fluorescence imaging (Figure 3.1a) was

performed at room temperature in air, using an upright epi-fluorescence microscope (Nikon Eclipse 80i) with a Nikon Apo 100×0.95 NA dry objective and a 670 ± 25 nm emission filter (Chroma 670/50M). Samples were illuminated at 488 nm ($100 \text{ W} \cdot \text{cm}^{-2}$) with a continuous-wave solid-state laser (Coherent Sapphire). Fluorescence movies (10 frames/s, up to ~ 7 h long) were captured by a thermoelectrically cooled CCD camera (PhotonMAX, Princeton Instruments). The fluorescence intensity of each emitter was determined in each frame throughout the entire movie (see Supplementary Information 3.5.2) and corrected by subtracting a background signal taken from a nearby dark region (see Supplementary Information 3.5.3), which was different from the thresholding method used for mica substrates in Chapter 2.

The mechanical stability of our setup with a drift of 100 nm/h, allowed us to trace the fluorescence dynamics for many hours. The small mechanical drift was accounted for by offsetting the position of the recorded frames appropriately during data analysis. The analysis of fluorescence statistics was performed after thresholding and subsequent digitizing of a thresholded signal and the conclusions in Chapter 3-5 hold qualitatively for a range of thresholds. Statistical analysis of various temporal sub-segments within a fluorescence movie showed no significant or systematic change in the blinking parameters of single NRs over the duration of the experiment. Still, effects of sample degradation over time cannot be excluded and some clusters become dark during measurements.

Following fluorescence imaging, we located NRs relative to the nearest gold markers using TEM (JEOL 2010) (Figure 3.1). TEM was always performed after the fluorescence measurements to avoid sample contamination and degradation. TEM image

analysis was performed using the Image Processing Toolbox application in Matlab. Image registration was applied to align the fluorescence and TEM images of the same sample area by using the gold grid pattern on the substrate, mapping four points on each image and transforming (e.g., rotating or expanding) one image to overlay it on top of the other. The uncertainty in overlaying the two images was < 100 nm, which is better than the spatial resolution of two nearby fluorescent sources (~ 330 nm). The measurement error in the number of NRs, N , comes primarily from TEM imaging and is estimated to be ± 1 for $N \leq 10$ and 10% for $N > 10$. The number of emitting NRs may be significantly smaller.

3.3 Results and Discussion

3.3.1 Individual NRs and effect of thresholds

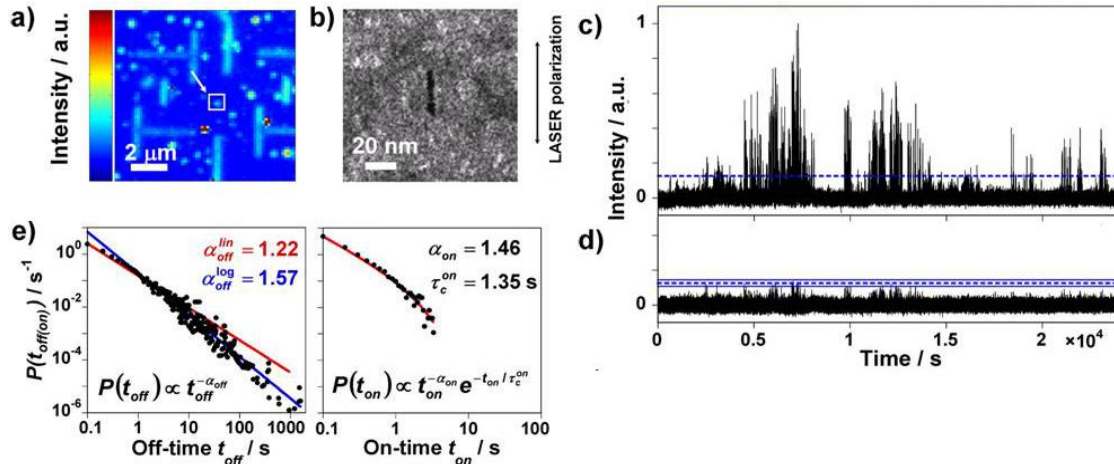


Figure 3.2 a) Fluorescence micrograph and b) TEM image of an individual CdSe/ZnSe/ZnS core/double shell NR, oriented approximately parallel to the laser polarization. c) Fluorescence intensity $v.s.$ time, $I(t)$, for this NR (dashed line indicates on-/off-threshold). d) Fluorescence intensity $v.s.$ time, $I(t)$, of a nearby dark region. Dashed blue line indicates the on-/off-threshold defined as $m_{dark} + 7\sigma_{dark}$ (as used in c), where m_{dark} is the mean and σ_{dark} is the standard deviation of the corresponding intensity $v.s.$ time of the dark region. The two solid blue lines correspond to $m_{dark} + 6\sigma_{dark}$ and $m_{dark} + 8\sigma_{dark}$ respectively (see Supplementary Information 3.5.3). (e) Probability densities of off-times (left) and on-times (right). The off-times are fitted to a power-law, either on a linear scale dominated by short off-times (red line) or on a \log_{10} - \log_{10} scale dominated by long off-times (blue line). The corresponding exponents are indicated. The on-times probability densities are best fitted by a truncated power-law with an exponent, $\alpha_{on} = 1.46$, and a truncation time, $\tau_c^{on} = 1.35$ s.

Figure 3.2 shows one example of an individual NR, oriented approximately parallel to the laser polarization direction (Figure 3.2b). The fluorescence intensity *vs.* time (also referred to as “intensity trajectory”), $I(t)$, recorded over 2.4×10^4 s, shows intermittency with relatively short on-times (<4 s), and long off-times up to ~ 1700 s (Figure 3.2c).

To examine the effect of the choice of threshold on the on- and off-time probability densities, we analyzed the trajectories using a range of threshold values. All results reported in this chapter were determined using a threshold of $m_{dark} + 7\sigma_{dark}$ (dashed blue lines in Figures 3.2c,d), chosen to lie above the signal from the dark regions, where m_{dark} and σ_{dark} are the mean and standard deviation of the intensity of a nearby dark region. Setting the threshold higher or lower by σ_{dark} (blue solid lines in Figure 3.2d) does not change the on-/off-time probability densities significantly (Supplementary Information 3.5.3).

Below we analyze the on- and off-time probability densities. For on-times, we observe a truncated power-law dependence, $P(t_{on}) \propto t_{on}^{-\alpha_{on}} e^{-t_{on}/\tau_c^{on}}$ where $\alpha_{on} \sim 1.5$ and $\tau_c^{on} \sim 1.4$ s (Figure 3.2e, right). [Tang 2007] We find that τ_c^{on} is the parameter most sensitive to the threshold level; it changes by $\sim 10\%$ over the threshold range investigated (between the two solid blue lines in Figure 3.2d), while $\alpha_{on(off)}$ change by less than 1% (more details in Supplementary Information 3.5.3).

3.3.2 A truncated Lévy off-time distribution

We now focus on the off-time statistics, for which the Lévy distribution without truncation, $P(t_{off}) \propto t_{off}^{-\alpha_{off}}$, has been routinely observed in previous studies. The off-time

probability density of an individual NR (Figure 3.2e, left) indeed approximately follows a power law, $P(t_{off}) \propto t_{off}^{-\alpha_{off}}$, with $\alpha_{off}^{lin} \sim 1.2$, obtained by fitting a power law to the data on a linear scale (red line). Alternatively, a linear fit to $\log_{10} P(t_{off})$ vs. $\log_{10} t_{off}$ gives $\alpha_{off}^{\log} \sim 1.6$ (blue line). Such a fitting accounts more accurately for the longer off-events, while both fitting approaches have been used in literature. [Wang 2006, Kuno 2000]

However, we find that the Lévy process does not hold indefinitely, and is also truncated, but on a much longer timescale than the on-times. To determine the truncation time, we measured 22 other 2.4×10^4 s -long intensity trajectories of single NRs. The unprecedented length of our measurements reveals the previously unobserved truncation of the Lévy distribution of the off-times for single NRs. Figure 3.3 shows a truncated power-law fit, $P(t_{off}) \propto t_{off}^{-\alpha_{off}} e^{-t_{off}/\tau_c^{off}}$, to the off-time probability density for the aggregated data of all the individual NRs measured. The data and the truncated power law fit (red line) clearly fall below the power-law fit (blue dashed line) by roughly a decade in the tail of the distribution. The truncated-power law fits give values of $\alpha_{off} = 1.56$ and $\tau_c^{off} \sim 1100$ s for a single NR (shown in Figure 3.2), and $\alpha_{off} = 1.78$ and $\tau_c^{off} = 2500$ s for the aggregated data. A truncated Lévy off-time distribution with such a long cut-off time is consistent with the results of ensemble measurements on spherical nanocrystals. [Chung 2004]

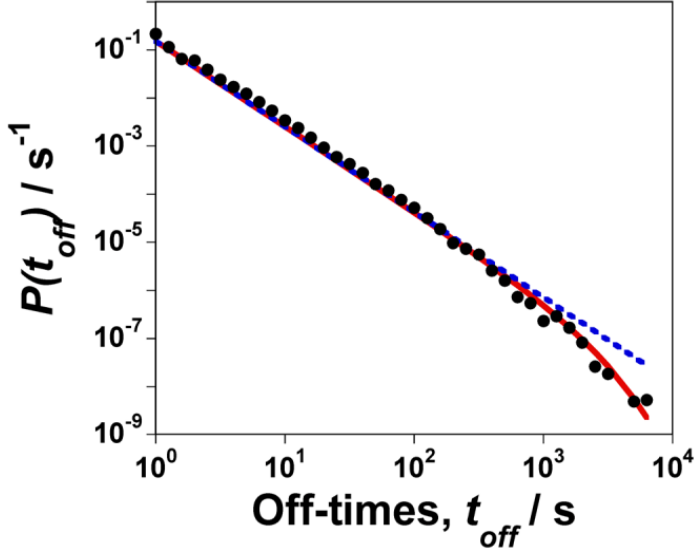


Figure 3.3 Off-time probability density of the aggregated data from all 23 individual NRs measured for 2.4×10^4 s. The data is best fitted by a truncated power-law (red), $P(t_{off}) \propto t_{off}^{-\alpha_{off}} e^{-t_{off}/\tau_c^{off}}$, with $\alpha_{off} \sim 1.78$ and $\tau_c^{off} \sim 2500$ s. The power-law fit (blue dashed line) is indicated for comparison.

3.3.3 Small clusters

Of all the fluorescent sources examined with TEM, ~25% correspond to small clusters of 2 or more NRs that are sufficiently close to each other and cannot be resolved by optical microscopy. Figure 3.4 shows the fluorescence intensity *vs.* time, $I(t)$, and corresponding TEM images of another single NR and two small NR clusters: (a) an individual NR oriented at $\sim 35^\circ$ relative to the laser polarization direction, (b) two NRs aligned parallel to each other, spaced by ~ 10 nm, oriented at $\sim 15^\circ$ relative to the laser polarization direction, and (c) three NRs, spaced by ~ 50 - 100 nm, oriented at 0° , 45° and 40° relative to the polarization direction, respectively. Note that these intensity trajectories are shorter, 1500 s long. The examples in Figure 3.4 illustrate that an individual NR (Figure 3.4a) and small clusters (Figures 3.4b, c) can exhibit visually similar intensity trajectories. However, it has to be noted that the intensity trajectories should be compared with caution since the NRs are not oriented at the same angles. As NRs couple to the

laser field predominantly along their long axis, the emission intensity, I , depends on the angle, θ , between the NR long axis and the laser polarization: $I \sim \cos^2 \theta$. [Hu 2001] As an example, rotating the laser polarization by 90° in the case of the two NRs, shown in Figure 3.4b, decreased their maximum emission intensity to $\sim 10\%$ of the initial integrated intensity as θ increased from $\sim 15^\circ$ to $\sim 75^\circ$, which is in good agreement with the expected angle dependence. Details for this and a few other examples are given in the Supplementary Information 3.5.4. Furthermore, the observed broad intensity distribution of these trajectories does not necessarily indicate multiple particles but rather demonstrates a continuous distribution of emission states (instead of a single “on” state) even for a single NR, as discussed by Zhang *et al.* [Zhang 2006]

Figure 3.4d shows the off- and on-time probability densities, $P(t_{off})$ and $P(t_{on})$, and the corresponding fits, for clusters of two NRs (Figure 3.4b) and three NRs (Figure 3.4c), respectively. The threshold above which the NRs are considered “on” is defined as in the case of single NRs and the consistency of fitting parameters is verified for a range of threshold values as detailed in Supplementary Information 3.5.3. Similar to individual NRs, we find a power-law distribution for the off-times, where $\alpha_{off,2}^{lin} \sim \alpha_{off,3}^{lin} \sim 1.3$, and a truncated power-law distribution for the on-times for the two and three NRs with a truncation time τ_c^{on} in the range of $\sim 1\text{-}2$ s. A linear fit to the off-time probability densities on a log-log scale yields larger values of the power-law exponents, $\alpha_{off,2}^{\log} \sim \alpha_{off,3}^{\log} \sim 2$ for the two and three NRs, respectively. In comparison, individual NRs, as shown in Figure 3.4a, exhibit very similar parameters, $\alpha_{off}^{lin} \sim 1.4$ and $\alpha_{off}^{\log} \sim 2.3$, and the truncation time for on-events, $\tau_c^{on} \sim 3$ s. We note that the downward bending of the off-time PDF in Figure 3.4d

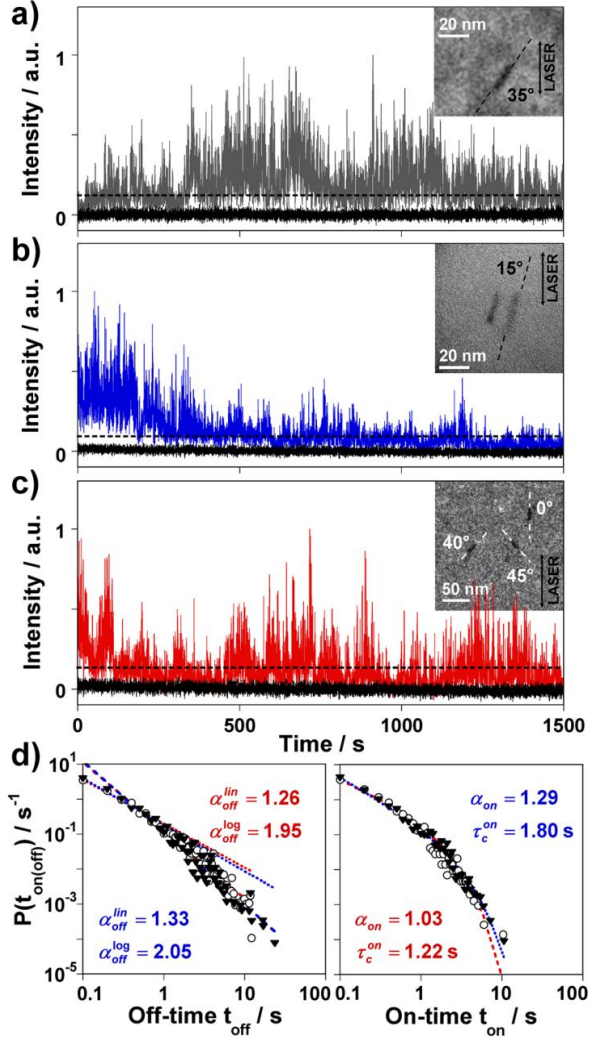


Figure 3.4. $I(t)$ and corresponding TEM images of a) an individual NR, b) two parallel NRs, ~ 10 nm apart, and c) three randomly oriented NRs, spaced between ~ 50 and ~ 100 nm. The relative orientation with respect to the laser polarization is indicated in each case. Fluorescence intensity vs. time, $I(t)$, of nearby dark regions are also shown in each case (black curves). d) Off-time and on-time probability densities for the two clusters, comprised of two (blue) and three (red) NRs, respectively. The fitting parameters for the truncated power-law (on-times) and power-law (off-times) are indicated (see also Table 3.1).

Table 3.1. Blinking parameters of individual NRs ($N = 1$) and small NR clusters up to $N = 15$.

N^a	1 ^b	2 ^b	3 ^b	5	7	10	15
α_{on}	1.46 (1.46)	1.29 (1.46)	1.03 (1.19)	1.36	1.48	1.29	1.40
τ_c^{on} / s	1.35 (1.40)	1.80 (2.38)	1.22 (4.00)	35.9	40.02	26.8	487.69
α_{off}^{lin}	1.22 (1.26)	1.33 (1.28)	1.26 (1.32)	1.38	1.39	1.35	1.46
α_{off}^{\log}	1.57 (1.69)	2.05 (1.75)	1.95 (1.98)	1.86	2.02	1.91	2.15

^a N is the number of NRs in one cluster. ^bThe indicated values correspond to the clusters shown in Figures 3.2, 4b and 4c, whereas the italic numbers in parentheses are the averages determined from all observed events with the same N (i.e., twenty four for $N = 1$, four for $N = 2$, two for $N = 3$).

is less pronounced than that in Figure 3.3, since the total measurement duration, 1500 s, is shorter than the truncation time determined above. The exact values of fitting parameters are listed in Table 3.1, together with their mean values obtained from several clusters containing one, two, and three NRs, respectively. The maximum off-time, t_{off}^{\max} , for $N = 1$ is smaller than those of $N = 2$ and $N = 3$ (20 s vs. 38 s and 25 s), while the maximum on-time, t_{on}^{\max} , for $N = 1$ is smaller than that of $N = 2$ (20 s vs. 25 s) but larger than that of $N = 3$ (20 s vs. 16 s). Based on these parameters, the trajectories cannot be *a priori* attributed to a particular N .

Among all $\sim 2.4 \times 10^4$ s-long fluorescence measurements, using TEM we have identified 23 individual blinking NRs and 8 additional blinking sources that correspond to clusters consisting of up to $N = 15$ NRs. The sizes of these clusters range from ~ 40 nm ($N = 2$) to ~ 300 nm ($N = 15$) in diameter. Figure 3.5 displays seven fluorescence intensities vs. time, $I(t)$, in order of increasing number of particles, $N = 1, 2, 3, 5, 7, 10$ and 15 , with their corresponding background signals and threshold levels. While the intensity trajectories for small N are visually similar, larger clusters exhibit noticeably larger intensities that are significantly elevated above the baseline. In addition, the maximum off-time decreases as N increases (from $t_{off}^{\max} \sim 2200$ s ($N = 1$) to ~ 70 s ($N = 15$)), while the maximum on-time shows an opposite trend (from $t_{on}^{\max} \sim 7$ s ($N = 1$) to ~ 3000 s ($N = 15$)).

3.3.4 Blinking parameters

Figure 3.6 shows the histograms of blinking parameters α_{on} , τ_c^{on} , and α_{off} (*i.e.*, α_{off}^{lin} and α_{off}^{\log}) for both individual NRs and clusters. From the histograms for individual NRs

(black bars in Figure 3.6), we find the means and standard deviations of the blinking parameters to be $\alpha_{off}^{lin} = 1.26 \pm 0.06$, $\alpha_{off}^{\log} = 1.7 \pm 0.2$, $\alpha_{on} = 1.5 \pm 0.2$, and $\tau_c^{on} = 1.4 \pm 0.6$ s.

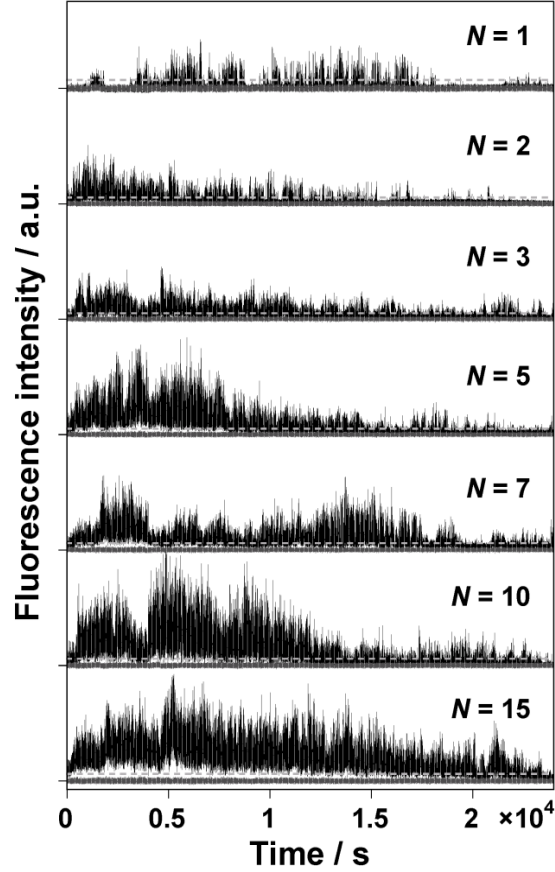


Figure 3.5 Fluorescence intensities vs. time, $I(t)$, in order of increasing particle number, $N = 1$ to 15 , with their corresponding background signals (gray curves) and threshold levels (dashed lines), recorded over $\sim 2.4 \times 10^4$ s.

We have also sampled the on- and off-time probability distributions of single NRs throughout a ~ 6 -h-long measurement by dividing it into three 2-h-long segments and sampling the corresponding probability distributions. Such an analysis shows that probability distributions of single NRs do not change significantly over time and there are no evident systematic trends of the blinking parameters. In turn, this also implies that the decrease of average fluorescence intensity over time observed in some clusters (see Figure 3.5) could be due to statistical aging of ensembles. [Brokmann 2003]

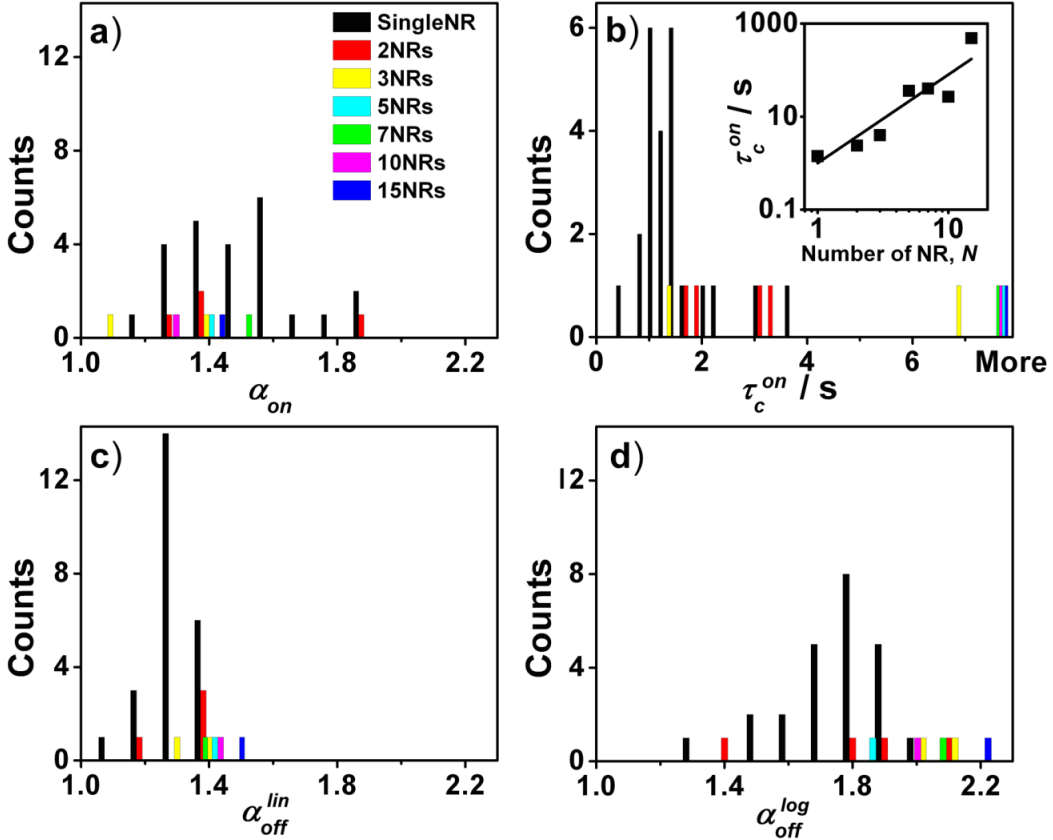


Figure 3.6 Histograms of the blinking parameters (a) α_{on} , (b) τ_c^{on} , (c) α_{off}^{lin} and (d) α_{off}^{log} for 24 individual NRs and 10 additional blinking sources that correspond to NR clusters consisting of up to 15 NRs, including also the spots measured only for 1500 s (shown in Figure 3.4). The values of α_{off} (*i.e.*, α_{off}^{lin} and α_{off}^{log}) for $N \geq 2$ fall above the mean values of the corresponding distributions of single NRs, while the values of α_{on} for $N > 2$ fall within those obtained for individual NR. Inset of b): τ_c^{on} vs. N on a \log_{10} - \log_{10} scale. τ_c^{on} increases to ~ 30 s for $N = 5-10$ and up to ~ 500 s for $N = 15$ (solid line shows the best fit to the data, $\tau_c^{on} \sim N^{1.9}$).

Correlated TEM imaging also allows for a direct measurement of the angle of NRs, θ , relative to the laser polarization that can be aligned with the gold markers on the substrate. Our analysis (Supplementary Information 3.5.4) suggests no apparent dependence of the blinking parameters of single NRs on θ . However, any potential angle dependence might become unobservable because of the variation of blinking parameters across the single NRs measured (black bars in Figure 3.6). We also measured a series of 600 s-long fluorescence movies of ~ 80 single NRs in which the linear polarization of the laser was alternated between two orthogonal directions in successive movies. These

measurements did not reveal any clear dependence of the blinking parameters on polarization direction. In order to see any potential angle dependence, more precise values of the blinking parameters are required, which in principle can be achieved by performing measurements of longer durations. In addition, our preliminary measurements of NR blinking using both circular and linear polarization showed similar distributions of truncation times. All these results suggest that the effect of polarization is simply to change the excitation intensity, and are consistent with the weak intensity dependence of the blinking parameters reported in Chapter 2. [Wang 2006]

The broad distribution of single-NR blinking parameters means that the on- and off-exponents for clusters fall within the range of the values observed for single NRs. In addition, the observed values of τ_c^{on} for $N = 2$ and 3 lie within the observed range of single NR blinking parameters, indicating that probability density analysis cannot be used as a reliable way to distinguish between single NRs and small clusters; only direct particle counting allows us to unambiguously distinguish single particles from small clusters ($N = 2, 3$). Similarly, we find that the integrated intensity, calculated as $I_{int} = \left(\sum_{i=1}^M I_i \right) / M$, where I_i is the intensity count after the background subtraction for the i^{th} time interval of 0.1 s, from $N = 2$ clusters is indistinguishable from the range of integrated intensities observed from single NRs. Other methods of analysis such as autocorrelation function do not reveal differences between single NRs and clusters either (Figure 3.15 in Supplementary Information). In contrast, Ref. [Yu 2006] finds that autocorrelation function (ACF) analysis can be used to distinguish between individual nanoparticles and nanoparticle clusters. They attribute the difference of ACF in clusters to

inter-particle interactions possibly arising from the close packing of quantum dots and a different sample preparation method. However, that work does not address differences that may exist in the blinking parameters, thus not allowing a comparison with our finding of the particle number dependence of the truncation times of the on-time probability density.

We do, however, observe an increasing τ_c^{on} with increasing particle number for $N > 3$. The inset of Figure 3.6b shows the mean τ_c^{on} as a function of N on a log-log scale. While the mean τ_c^{on} is ~ 1.4 s for individual NRs, it increases to ~ 30 s for $N = 5-10$ and ~ 500 s for $N = 15$; a fit to the data suggests that τ_c^{on} grows faster than N (the line shown corresponds to $\tau_c^{on} \sim N^{1.9}$). Additionally, the values of α_{off} (Figures 3.6c,d) for $N > 2$ all fall above the mean values of the corresponding distributions obtained from single NRs. These trends, being insensitive to the choice of threshold (see Supporting Information), are consistent with larger N increasing the probability of long on-events (*i.e.*, larger τ_c^{on}) and the maximum on-time, and decreasing the probability of long off-events (*i.e.*, larger α_{off}^{lin} and α_{off}^{\log}) and the maximum off-time.

3.4 Conclusion

In summary, we correlate blinking statistics of individual nanoparticles and their clusters to TEM imaging which determines the number of particles. We find that off- and on-time probability density analysis and autocorrelation function analysis do not unambiguously distinguish single particles from clusters of 2 or 3 particles. Direct determination of the particle number, N , can be only achieved by doing direct counting with TEM images.

However, clusters of 5 or more NRs can be distinguished from single NRs by their significantly larger τ_c^{on} . Finally, facilitated by very long fluorescence measurements, we have estimated the truncation time of the Lévy distribution of off-times for single NRs to be of the order of 2000 s.

The distance between NRs within the clusters in our study is highly variable, ranging from ~1-10 nm to ~50-100 nm. While direct charge tunneling between NRs is very unlikely, due to such relatively large inter-particle separations, it is difficult to *a priori* exclude longer-range energy transfer between NRs, [Xu 2006, Kimura 2004, Pons 2006, Shubeita 2003, Muller 2004, Crooker 2002, Shabaev 2004] given that blinking occurs on very long timescales and thus even relatively weak interactions could still have an effect. Possible forms of inter-particle interaction will be discussed in following chapters.

3.5 Supplementary Information

3.5.1 Experimental details NR synthesis and characterization

CdSe/ZnSe/ZnS core/double shell semiconductor nanorods (NRs) were prepared in a two-step procedure. First, CdSe core NRs having a diameter of 5.8 nm and a length of 34 nm were synthesized using a multiple injection method. [Shieh 2005] In detail, 45.1 mg of cadmium oxide (CdO, Aldrich, 99%) had been placed with 140.9 mg of decylphosphonic acid (DPA, Alfa Aesar, 99%) and 5.5 g of tri n-octylphosphine oxide (TOPO, Aldrich, 90%) under nitrogen atmosphere and were heated to 300°C for approximately 2 hours until the initially red-brown suspension turned colorless. Independently, a solution of 563 mg of selenium powder (Se, Aldrich, 99.99%) was

dissolved in 7 mL of tri n-octylphosphine (TOP, Aldrich, 99%). The TOPSe solution was injected slowly into the Cd-precursor solution in aliquots of 0.1 mL (5 times, 2 minute waiting between each injection), 0.2 mL (5 times, every 3 minutes), and finally 0.4 mL (10 times, every 5 minutes). The initial injection temperature was 295°C, which was gradually reduced via 280°C (during the 0.2 mL injections) to 270°C (for the 0.4 mL injections). The reaction was stopped after 80 minutes by removing the heating source and the growth solution was allowed to cool to 60°C, when 20 mL of methanol were added to precipitate the NRs. After centrifugation and washing additionally with methanol (3 times), the NRs were dispersed in toluene for optical characterization (Figure 3.7a).

The absorption spectrum (USB-2000 spectrometer, Ocean Optics) was characterized by an excitonic peak at 640 nm. Concentration dependent absorption measurements allowed us to determine an absorption cross-section at 488 nm to be $4.22 \cdot 10^{-14} \text{ cm}^2$. [Wang 2006] The emission (USB-4000FL spectrometer, Ocean Optics, excitation: 470 nm LED, 35 μW) of these NRs was centered at 665 nm with a full-width at half medium (FWHM) of 38 nm, i.e., this sample exhibited a Stokes shift of 15 nm. Comparing the area of the emission peak to the one of an aqueous solution of rhodamine 6G adjusted to an identical optical density at the excitation wavelength allowed us to estimate a fluorescence quantum yield of 0.3%.

These NRs were further characterized by high-resolution transmission electron microscopy (HRTEM, JEOL 2010F) after deposition on holey carbon grids from a dilute solution. From the TEM images (Figure 3.7a inset) we determined a NR size of 5.8×34 nm, *i.e.*, the aspect ratio is ~ 5.9 .

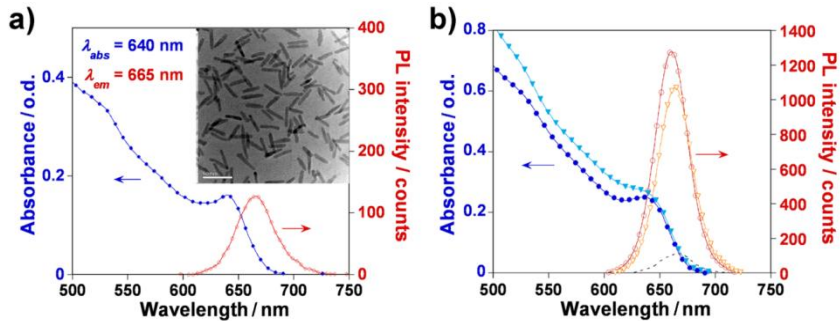


Figure 3.7 a) Absorption and emission spectra of CdSe core NRs recorded in toluene. The inset shows a TEM image (the scale bar is 50 nm) of this sample. b) Absorption and emission spectra of CdSe/ZnSe core/shell NRs (circles, dark blue and red) and of CdSe/ZnSe/ZnS core,double shell NRs (triangles, light blue and orange). For comparison reasons, the emission of the core NRs is indicated as dashed line.

Subsequently, the CdSe core NRs were capped with a thin intermediate ZnSe shell and a thicker ZnS outer shell to prepare the CdSe/ZnSe/ZnS core,double shell system. [Reiss 2003] In particular, $4.4 \cdot 10^{-9}$ mol of the CdSe core rods had been mixed with 5.0 g of TOPO and 3 g of hexadecylamine (HDA, Aldrich, 90%). Solutions of 0.08 M TOPSe (6.4 mg Se in 1 mL TOP) and 50 mg of zinc stearate (ZnSt, Aldrich, 99%) in 1 mL of dioctylamine (DOA, Aldrich, 99%) were prepared and mixed together. These quantities should correspond to the formation of 1 monolayer (ML) of ZnSe. At 225°C, this solution was slowly injected over a period of 10 min. The reaction mixture was allowed to stir for another 15 minutes.

The absorption and emission spectra of the core/shell(s) systems are summarized in Figure 3.7b. The absorption of all three samples is very similar and the main difference consists in a increasing absorption at higher energies (*i.e.*, at smaller wavelengths) with increasing shell thickness. The width of the emission peak remains unchanged upon shell growth and is slightly red-shifted (with increasing shell(s) thickness) compared to the core NRs. The fluorescence quantum yield increased significantly during the shell growth: from 0.3% for the CdSe core sample to 1.7% for the CdSe/ZnSe core/shell NRs and 1.6%

for the CdSe/ZnSe/ZnScore/double shell NRs. These values were obtained for the extensively purified samples. One can however note that for samples taken at intermediate stages of the shell growth, recorded in solutions containing still excess surface ligands such as HDA or DOA, fluorescence quantum yields of up to 14% for the core/shell NRs and 6.1% in the case of the core/double shell NRs have been measured.

3.5.2 Determination of fluorescence intensity vs. time from fluorescence movies on silicon nitride membranes

Fluorescence from a single emitter was determined by integrating the signal from the appropriate “segment” (region) of a fluorescence image. For the data in this and following chapters, we determined the segments for individual emitters by correlating them with TEM images (Figure 3.8). For the analysis, we chose clusters that can be optically resolved from nearby emitters. The resolution determined by the emission wavelength (λ) and the numerical aperture (NA) of our setup can be calculated as $\lambda / 2NA \sim 330$ nm which corresponds to ~ 2 pixels of the magnified image on our CCD detector, so that the fluorescence from an emitter was spread over an area ranging from 2×2 pixels to 4×6 pixels in our samples.

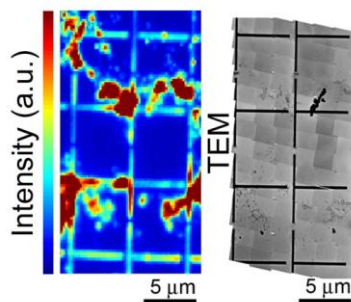


Figure 3.8 Fluorescence micrograph of a $18 \times 12 \mu\text{m}^2$ region on the $175 \times 175 \mu\text{m}^2$ Si_3N_4 membrane window (50 nm thickness), and TEM of the same transparent window region patterned with a grid of gold lines, composed by combining 84 high-resolution TEM images.

The fluorescence intensity of each cluster was determined in each frame throughout the entire movie and it was corrected by subtracting the background measured from a nearby bare region of the substrate; for example, **e** is the background segment of **a** and **c**, and **f** is the background segment of **d** (Figure 3.9).

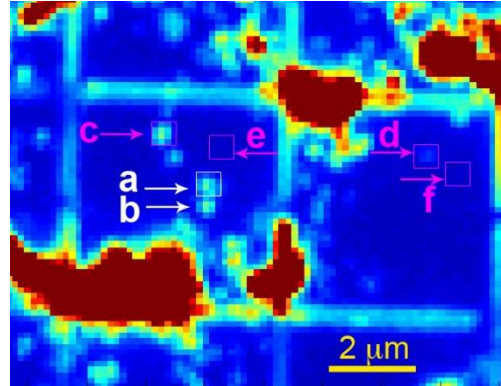


Figure 3.9 Fluorescence micrograph of a 13 by 9 μm^2 region on the 175 by 175 μm^2 Si_3N_4 membrane window (50 nm thickness). **a, c, d**, Three clusters used in the data analysis in the paper, with $N = 2, 4$, and 2, respectively. **b**, Another cluster near the cluster **a**. **e**, The background segment of clusters **c** and **a**. **f**, The background segment of cluster **d**.

The centers of the fluorescence segments that we analyzed are separated by at least 3 pixels from the centers of their nearest neighbors. Segments **a**, **c** and **d** are three emitting spots included in the data analysis with $N = 2, 4$, and 2, respectively, and **b** is another bright spot near **a**. However, the brightness spreads out from the center of some emitters (e.g. **a** and **c**) to the edges of the neighboring spots, though the centers (local maximal brightness) of them can be well resolved.

3.5.3 Background correction and definition of threshold for fluorescence intensity trajectories on silicon nitride membranes

In contrast to mica, silicon nitride (Si_3N_4) membrane devices show a slight background fluorescence signal that is not homogenous throughout the whole substrate. Consequently, in the study of this and following chapters, each fluorescent segment was corrected with

respect to a dark segment in its vicinity. Moreover, the background can evolve slightly over time for very long fluorescence movies. To account for these changes, we fit the background signal with a fourth-order polynomial that is subtracted from the fluorescence segment (Figure 3.10a). To set the threshold level, we previously added the width of the background noise plus one standard deviation to the minimum of the fluorescence intensity time trace. [Wang 2006] Figure 3.10b shows the intensity time-trace of an individual NR (corrected according to Figure 3.10a) and the different threshold levels that were tested. Here, m_{dark} is the mean, and σ_{dark} is the standard deviation of the intensity *vs.* time of a nearby dark region, ΔI_{dark} and $min(dark)$ are the width and the minimum value of the background signal, and $min(intensity)$ is the minimum value of fluorescence intensity *vs.* time.

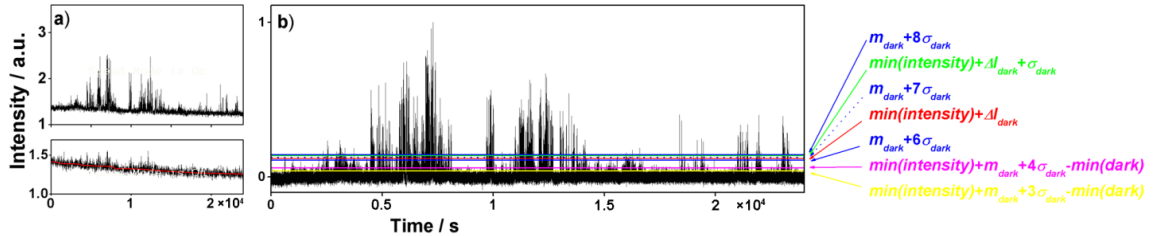


Figure 3.10 (a) Background signal with a polynomial fit. (b) Intensity trajectory of an individual NR. Different lines (color) are the different threshold levels tested.

Table 3.1 summarizes the blinking parameters for the individual NRs and small clusters. In conclusion, all results reported in this chapter were determined using a threshold of $m_{dark} + 7\sigma_{dark}$ chosen to lie above the signal from the dark regions. Setting the threshold higher or lower by σ_{dark} does not change the on-/off-time probability densities significantly (Table 3.2). Figure 3.11-13 shows the histograms of blinking parameters from individual NRs and small clusters up to 15NRs using three different thresholds.

Table 3.2 List of blinking parameters of NR clusters from **Figures 3.2, 3.4** for different threshold levels (see also **Figure 3.10**).

Threshold	Individual NR (from Figure 2)				Individual NR (from Figure 4a)				Two NRs (from Figure 4b)				Three NRs (from Figure 4c)			
	α_{on}	τ_c^{on} / s	α_{off}^{lin}	α_{off}^{\log}	α_{on}	τ_c^{on} / s	α_{off}^{lin}	α_{off}^{\log}	α_{on}	τ_c^{on} / s	α_{off}^{lin}	α_{off}^{\log}	α_{on}	τ_c^{on} / s	α_{off}^{lin}	α_{off}^{\log}
$m_{dark} + 8 \sigma_{dark}$	1.44	1.19	1.23	1.56	1.11	2.43	1.32	2.25	1.27	2.72	1.29	1.92	1.10	1.52	1.24	1.88
$\min(\text{intensity}) + \Delta I_{dark} + \sigma_{dark}$	1.49	1.32	1.23	1.57	1.16	3.10	1.34	2.29	1.22	1.70	1.32	2.05	1.04	1.61	1.28	2.04
$\min(\text{intensity}) + \Delta I_{dark}$	1.42	1.30	1.23	1.57	1.06	3.52	1.40	2.47	1.25	2.13	1.35	2.02	1.14	2.13	1.31	2.18
$m_{dark} + 7 \sigma_{dark}$	1.46	1.35	1.22	1.57	1.1	2.96	1.36	2.33	1.29	1.80	1.33	2.05	1.03	1.22	1.26	1.95
$m_{dark} + 6 \sigma_{dark}$	1.44	1.40	1.24	1.58	1.03	3.50	1.41	2.48	1.26	2.29	1.37	2.07	1.11	1.83	1.28	2.06
$\min(\text{intensity}) + (m_{dark} + 4\sigma_{dark} - \min(\text{dark}))$	1.62	2.37	1.23	1.66	1.00	3.36	1.42	2.49	1.27	2.54	1.31	1.92	1.18	2.31	1.31	2.21
$\min(\text{intensity}) + (m_{dark} + 3\sigma_{dark} - \min(\text{dark}))$	1.86	3.9	1.20	1.78	1.05	4.72	1.45	2.50	1.18	3.46	1.35	2.06	1.07	2.86	1.39	2.30

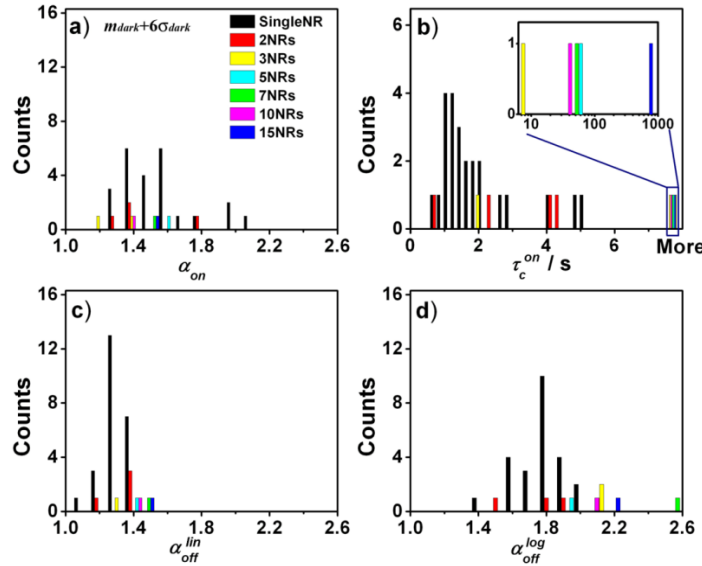


Figure 3.11 Histogram of the blinking parameters (a) α_{on} , (b) τ_c^{on} , (c) α_{off}^{lin} and (d) α_{off}^{\log} of individual NRs and small clusters up to 15NRs, shown for $m_{dark}+6\sigma_{dark}$.

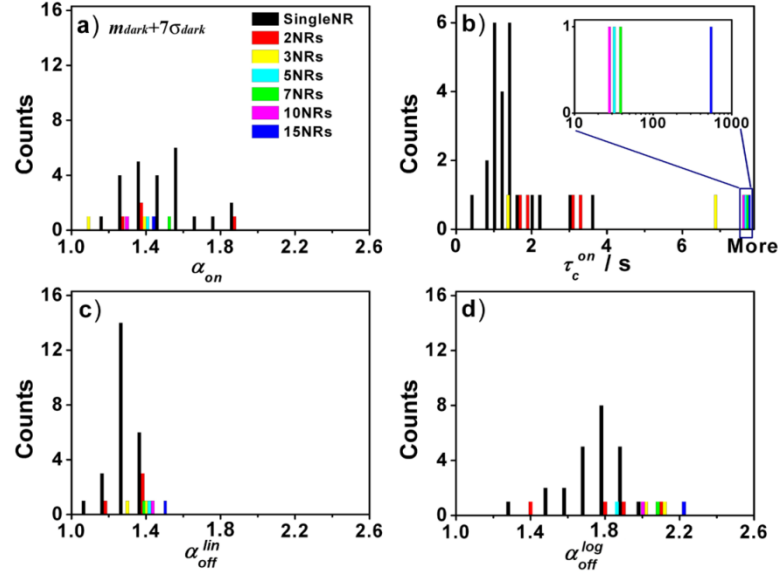


Figure 3.12 Histogram of the blinking parameters (a) α_{on} , (b) τ_c^{on} , (c) α_{off}^{lin} and (d) α_{off}^{\log} of individual NRs and small clusters up to 15NRs, shown for $m_{dark} + 7\sigma_{dark}$

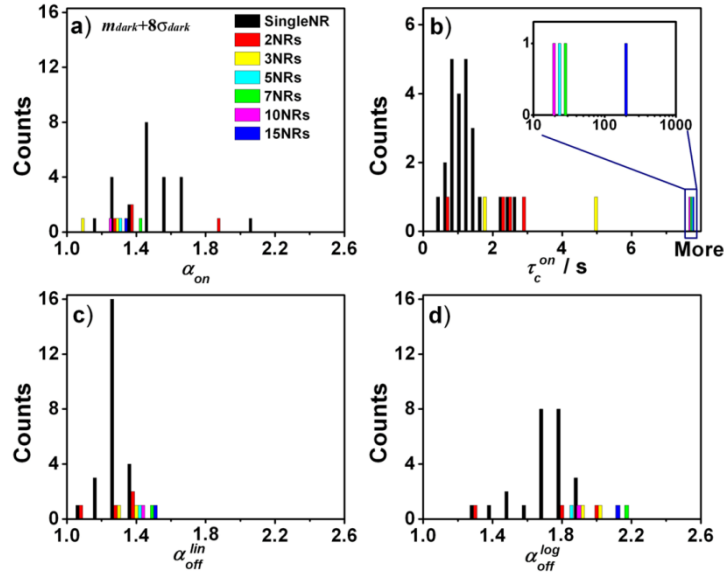


Figure 3.13 Histogram of the blinking parameters (a) α_{on} , (b) τ_c^{on} , (c) α_{off}^{lin} and (d) α_{off}^{\log} of individual NRs and small clusters up to 15NRs, shown for $m_{dark} + 8\sigma_{dark}$.

3.5.4 Dependence of blinking parameters on NR angle relative to the laser polarization direction

Figure 3.14 shows blinking parameters of individual NRs on silicon nitride substrates as a function of NR angle relative to the laser polarization direction.

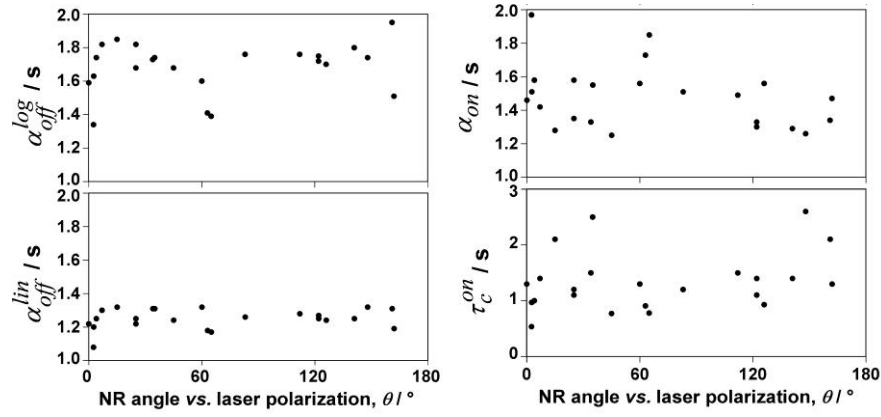


Figure 3.14 Blinking parameters of individual NRs on silicon nitride substrates as a function of NR angle relative to the laser polarization direction.

3.5.5 Auto-Correlation Function Analysis

The autocorrelation function is defined as

$$g_2(\tau) = \frac{\langle I(t) \cdot I(t + \tau) \rangle}{\langle I(t)^2 \rangle},$$

where $I(t)$ is the fluorescence intensity at time t , and τ is the lag time.

Figure 3.15 shows the autocorrelation functions of the fluorescence intensity trajectories of individual NRs and small NR clusters up to 15 NRs. We find that the autocorrelation functions of NR clusters fall within the broad family of curves for single NRs and that no clear distinction can be made in terms of slope or magnitude.

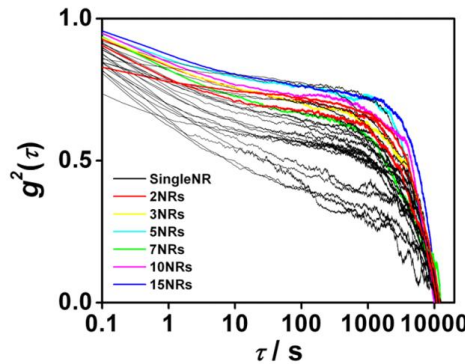


Figure 3.15 Autocorrelation functions of individual NRs (black curves) and small NR clusters (shown in color).

Chapter 4

Fluorescence dynamics of semiconductor nanorod clusters

4.1 Introduction

While the blinking of single semiconductor nanoparticles, including core and core-shell CdSe NRs,[Wang 2006] has been studied, the inability to determine particle number directly has so far impeded the correlation of emission properties in groups of emitting particles with the number of particles. Though significant progress has been made in elucidating the possible origins of single nanocrystal blinking, and in developing theoretical models to explain the blinking dynamics, [Cichos 2007] including trap models [Nirmal 1996, Shimizu 2001, Kuno 2001, Efros 1997] and random walk models, [Shimizu 2001] less attention has been given to ensemble emission properties as well as their relation to single-particle blinking. For collections of independent CdSe nanocrystals, Brokmann *et al.* reported that the fluorescence intensity decays as a power-law in time with an exponent between 0 and 1, as a consequence of the Lévy statistics governing the blinking process of single emitters. [Brokmann 2003] This leads to a non-ergodic intensity decay with time, termed statistical aging. Recently however, an ergodic nature of collections of independent emitters, as manifested at long times by the steady-state ensemble emission, has been discussed by Chung *et al.* [Chung 2004, 2006, 2007] and Tang and Marcus. [Tang 2005c, 2006] In order to reconcile the steady-state emission from ensembles with single-particle behavior, single-particle blinking should show deviations from Lévy statistics at long time-scales. The probability density should decrease faster than a power-law at long off-times. Consequently, an upper bound for the

single-quantum dot power law behavior, *i.e.*, a truncation time, τ_c^{off} (denoted as t_{off}^{\max} in Ref. [Chung 2004, 2006, 2007]), is established. On-time probability densities deviate from the power-law at significantly shorter times ($\tau_c^{on} \sim 10$ s) than the off-time distributions ($\tau_c^{off} \sim 1000$ s) and are therefore more easily experimentally accessible. This exponential truncation behavior of single-particle blinking has been presented in Chapter 2 and 3. With NRs, the power-law blinking behavior is truncated at shorter time-scales ($\tau_c^{on} \sim 1\text{-}10$ s) compared to spherical nanocrystals. In addition, the truncation time for on-states decreases with increasing NR aspect ratio, which should further help to discriminate between the different blinking models that have been proposed.

In the experiments, the NRs were arranged in sub-micron and micron-sized clusters that were either closely packed or well isolated with average spacing of tens of nanometers. We used fluorescence microscopy, atomic-force microscopy (AFM) and transmission-electron microscopy (TEM) to correlate the emission properties with particle number and other structural details of the emitting clusters, such as the cluster area and the orientation and distribution of individual NRs within these clusters.

4.2 Experimental Methods

For the study in this chapter, we used the same CdSe/ZnSe/ZnS core/double shell semiconductor NRs as the samples in Chapter 3 (see Section 3.5.1). Low stress silicon nitride (Si_3N_4) substrates and gold markers were prepared using the same method as Section 3.2.

Solutions of NRs in toluene ($\sim 10^{-8}$ mol·L⁻¹) were deposited onto the substrate by drop-casting (~5 µL) and allowed to dry in air for ~5 min. Clusters formed readily, covering the whole substrate. Wide-field fluorescence imaging (Figure 3.1) was performed at room temperature in air. The experimental setup and the image processing are the same as the description in Section 3.2.

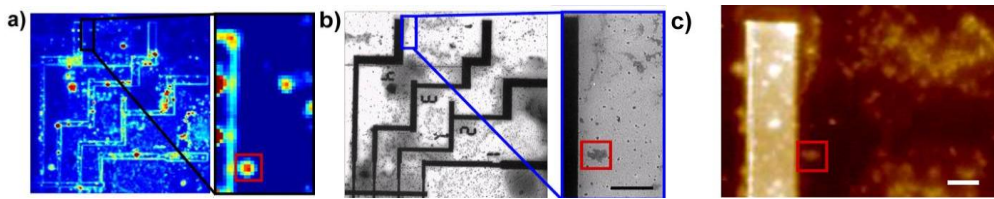


Figure 4.1 a) Fluorescence micrograph ($45 \times 45 \mu\text{m}^2$) of a silicon nitride (Si_3N_4) membrane with patterned gold markers, and a zoom-in image (right) corresponding to the region containing the cluster from Figure 4.2, indicated by the red square. b) Transmission electron micrograph (TEM) of the same region on the substrate. The scale bar in the zoom-in image, identifying the same cluster (red square), is 2 µm. c) Atomic force micrograph (AFM) containing the same zoom-in region shown in fluorescence and TEM images in a) and b); the red square outlines the same cluster as in a) and b). The scale bar is 2 µm.

Following the fluorescence imaging, we carried out TEM (JEOL 2010, operating at 200 kV) and AFM (Veeco EnviroScope, tapping mode) imaging of the whole membrane region and located emitting NR clusters relative to their nearest gold markers. TEM and AFM imaging was performed after the fluorescence experiment to avoid sample contamination and degradation. Figure 4.1 shows the correlated fluorescence (Figure 4.1a), TEM (Figure 4.1b) and AFM (Figure 4.1c) micrographs of the same region. To illustrate the correlation of one particular NR cluster, a red square outlining the location of this cluster is indicated in each micrograph (Figures 4.1a-c).

For comparison, we have also measured the fluorescence of clusters containing spherical CdSe/ZnS core-shell nanocrystals (Evident Technologies) with a core diameter of 4.1 nm and an emission peak at 580 nm. The experimental setup and conditions were identical to those detailed for the NR samples, except for the emission filter (Chroma 570/60M).

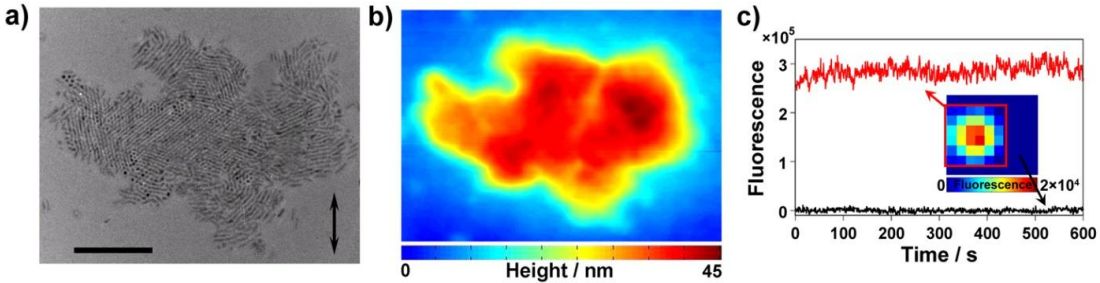


Figure 4.2. a) TEM of the cluster identified in Figure 4.1. The scale bar is 200 nm. b) AFM of the same cluster. c) Integrated fluorescence intensity *vs.* time (red) of the region indicated by the red square in the inset, corresponding to this cluster, and a nearby background segment (black) of the same size, *i.e.*, same number of pixels. Inset: zoom-in image of the fluorescence micrograph of this cluster.

4.3 Results and Discussion

4.3.1 Fluorescence/TEM/AFM correlation of NR clusters and direct particle counting

Figure 4.2 shows the TEM (Figure 4.2a), AFM (Figure 4.2b) and fluorescence (inset of Figure 4.2c) micrographs of one particular NR cluster containing ~ 1500 close-packed NRs. This cluster is also indicated by the red square in Figures 4.1a-c. While TEM revealed the assembly patterns and the structural details at single nm-resolution as projected in plane, AFM provided the topographic height profile of the cluster. Both techniques were used in conjunction to determine the number of NR monolayers and to estimate the total number of particles, N , of the cluster. For example, we find from AFM that the maximum height of the cluster shown in Figure 4.2 is ~ 40 nm, while from TEM it is evident that most NRs ($\sim 93\%$) are oriented parallel to the substrate. Given the film thickness (40 nm) and the NR dimensions (8×38 nm), it is impossible to have standing NRs perpendicular to the substrate below the top layer of parallel NRs. Furthermore, the film thickness at different locations within a cluster is found to increase approximately in

increments of the NR width (*i.e.*, thickness of ~10, 20, 30 or 40 nm are recorded), suggesting that NRs stack in monolayers parallel to the substrate. Therefore, we can conclude that the cluster is composed of up to 4 stacked monolayers, considering that the NR diameter is ~8 nm and the organic shell is ~1-2 nm. Part of these in-plane oriented NRs form columnar phases with end-to-end assembled NRs. [He 2007] In addition, the TEM image shows that some NRs (106 out of 1500 NRs, *i.e.*, ~7% of the total number) form regions of vertical superlattices consisting of one layer of standing NRs, which are perpendicular to the substrate. The cluster height determined from AFM is consistent with the NR length of ~38 nm (including organic ligands). These assembly patterns differ from theoretical predictions based on entropically-driven assembly in two dimensions. [Bates 2000] Thus the assembly and packing of NRs is not purely entropically-driven, but interfacial energy and droplet drying dynamics do play a crucial role. [He 2007, Querner 2008] While we can accurately determine the absolute number of NRs in monolayers, the error in particle counting (~5% per NR monolayer) comes from multilayer regions because only the NRs in the top layer can be accurately counted (see Supplementary Information 4.5.1). Even though the cluster exhibits regions of highly ordered NRs (columnar phases), the overall angular distribution of the NRs is random.

The spatially-integrated fluorescence intensity *vs.* time of the cluster in Figures 4.2a,b is shown in Figure 4.2c (red curve) together with the corresponding background intensity signal (black curve). The average fluorescence intensity, measured over 600 s, is approximately constant in time, but it exhibits fluctuations around its mean intensity, $I_{mean} \sim 290000$ counts, with a standard deviation (σ) of ~14300 counts or $\sigma/I_{mean} \sim 5\%$. These fluctuations are ~6 times higher than the ones in the corresponding background

signal, which have $\sigma \sim 2400$ counts, and therefore it is clear that they originate from NR events.

Figure 4.3 shows four additional TEM images of close-packed NR clusters, illustrating the structural diversity of assembly patterns that can be observed, and their corresponding fluorescence intensity vs. time (respectively labeled a-d). The number of particles in these and 50 additional clusters (see Supplementary Information 4.5.2) was determined by combined TEM and AFM, as described above. Table 4.1 summarizes the structural parameters of twelve selected clusters, including the five clusters shown in Figures 4.2 and 4.3. Among all the clusters studied, the percentage of standing NRs ranged between 0 and 56%. We observe that a minimum

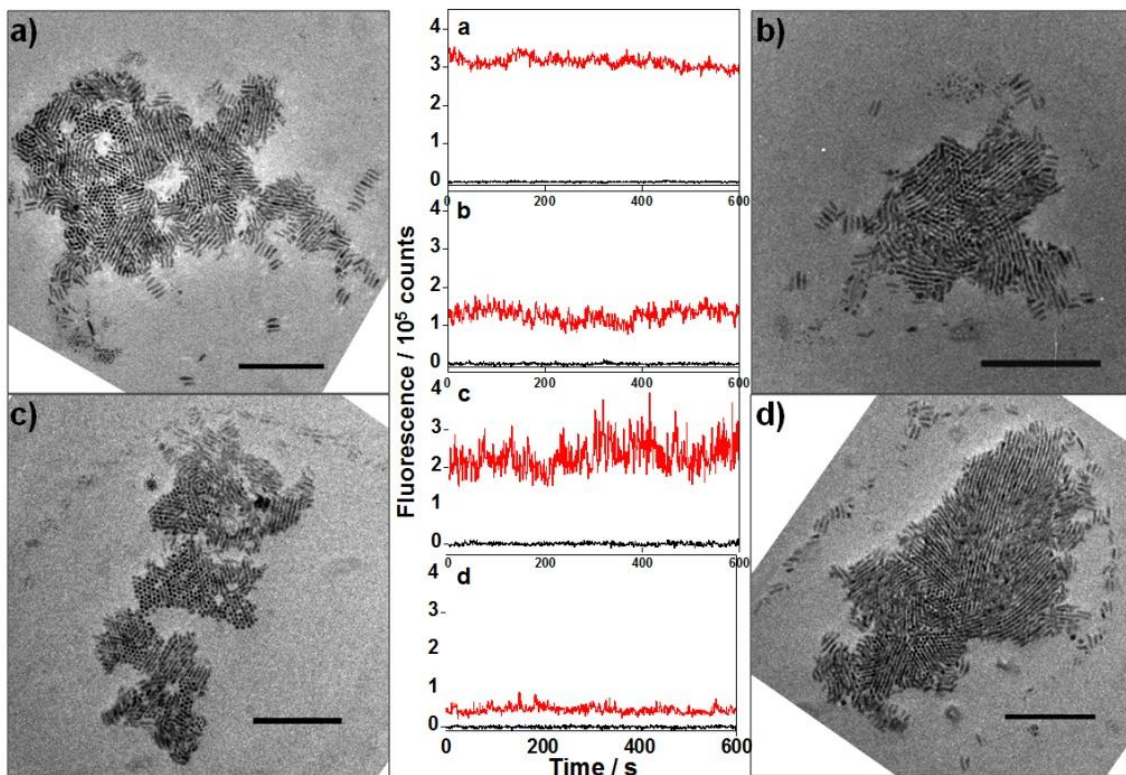


Figure 4.3. TEM images and corresponding integrated fluorescence vs. time (gray curves; black curves are traces from adjacent background segments) of four different clusters. The “fresh” clusters, shown in a)-c), have not been exposed to light prior to the fluorescence measurement whereas the cluster in d) was measured after previous laser light exposure, *i.e.*, it was “aged”. Scale bars are 200 nm. The TEM images are rotated to account for the orientation of the clusters with respect to the laser polarization, which is vertically in the plane of the page.

cluster size of ~250 NRs seems to be required before any standing NRs are observed. However, bigger clusters (up to ~700 NRs) can be observed without a single standing NR, while even larger clusters (>700 NRs) show at least 3% of standing NRs. Similarly, preferential orientation of NRs, and the extent of this ordering, can vary tremendously from cluster to cluster. As little as 7% or as many as 76% of the NRs were aligned within $\pm 30^\circ$ of an arbitrary reference (in this case this reference was chosen to be the direction of the laser polarization).

Neighboring NRs can be aligned to varying degrees, *e.g.*, in columnar phases or smaller regions of side-to-side oriented NRs (Figure 4.3a). This structural diversity of NR clusters was used to investigate the possible effects of individual parameters, such as particle number or assembly pattern, on the fluorescence properties.

Despite the large variety in structural patterns, the cluster area increases approximately linearly with the number of NRs. The slope gives a packing density of $\sim 6000 \text{ NRs}/\mu\text{m}^2$ (see Supplementary Information 4.5.3). The cluster-to-cluster variation is significant and most clusters range between 4000 and $8000 \text{ NRs}/\mu\text{m}^2$. Considering that a perfectly close-packed monolayer of planar NRs can contain $2500 \text{ NRs}/\mu\text{m}^2$, this density range is consistent with the varying thickness of the clusters up to four NR layers (Table 4.1). For comparison, in ensembles of loose-packed NRs (Figures 4.5 and 4.9), we found packing densities of $\sim 100\text{-}500 \text{ NRs}/\mu\text{m}^2$. In some cases (Figures 4.3c,d), the close-packed, multilayer clusters were surrounded by a “corona” of individual or loosely packed NRs which effectively decreases the overall particle density. For consistency, we will therefore relate all emission or structural parameters to the number of NRs, rather than the cluster area, in the following discussion.

4.3.2 Dependence of fluorescence intensity on N and assembly patterns

Within a short experimental window of ~ 10 min, the fluorescence emission of the NR clusters is relatively constant in time, and can therefore be represented by its mean intensity and standard deviation. Assuming that, on average, a similar fraction of NRs in each cluster are “bright”, *e.g.*, about one third of the NRs, [Ebenstein 2002] we expect a linear increase of the mean intensity with particle number. Figure 4.4a shows the mean fluorescence of 38 “fresh” NR clusters containing between 66 and ~ 1800 NRs, which have not been exposed to the laser beam prior to their measurement. It can be seen that the intensity does indeed increase with particle number. However, there is significant scatter around this trend. One factor that can contribute to the scatter is variations in the fraction of emitting NRs in each cluster. Even though we can determine the particle number in each cluster, we cannot measure directly the number of “dark” NRs. The number of “dark” NRs can be significant, since we found that about one half of the clusters on the substrate were completely “dark”, *i.e.*, they did not contain any “emitting” NRs within the experimental limit of detection. To explore other possible factors, we investigated the extent to which the assembly patterns of the clusters can be correlated to the fluorescence properties.

Table 4.1. Structural details and fluorescence properties of NR clusters.

Cluster #	Number of NRs ^a	Area (μm^2) ^b	NR layers ^c	Cluster density (NRs/ μm^2)	NR orientation ^d in plane			I_{mean} (counts) ^e (σ/I_{mean})
					upright (%)	$\pm(0\text{-}30^\circ)$ (%)	$\pm(30\text{-}60^\circ)$ (%)	
1	279	0.04	4	8305	5	76	11	9 *87400 (48%)
2	388	0.11	4	3526	0	15	57	29 32400 (40%) *76000 (32%)
3	418	0.05	3	9015	2	58	8	32 72800 (28%) *55600 (38%)
4	449	0.11	3	4144	0	28	25	48 27300 (12%)
5	671	0.07	4	9420	34	19	24	24 77000 (31%) *61500 (27%)
6 (Fig.3b)	764	0.09	3	8550	9	30	38	23 128000 (15%)
7 (Fig.3c)	1051	0.17	3	6063	41	16	20	23 231000 (18%) *97000 (22%)
8	1132	0.17	3	6851	3	56	17	23 294000 (7%)
9	1329	0.23	3	5893	38	19	20	23 180000 (18%) *71000 (28%)
10 (Fig.2)	1499	0.26	4	5857	7	24	34	35 288000 (5%)
11(Fig.3d)	1696	0.25	4	6791	7	47	26	19 *45500 (22%)
12 (Fig.3a)	1784	0.28	4	6448	11	40	21	28 314000 (5%)

^a Number of particles estimated by direct counting of top layers from TEM image and extrapolation for sub-layers assuming similar particle packing. ^b Cluster area determined from TEM images with ImageJ software. ^c Maximal number of NR layers constituting the cluster determined from height analysis with AFM. ^d Orientation of the NRs with respect to the substrate (upright or in plane) and with respect to the laser polarization. ^e Mean fluorescence intensity, I_{mean} , and standard deviation, σ , indicated in percent of I_{mean} . The data preceded by an asterisk are for “aged” NR clusters.

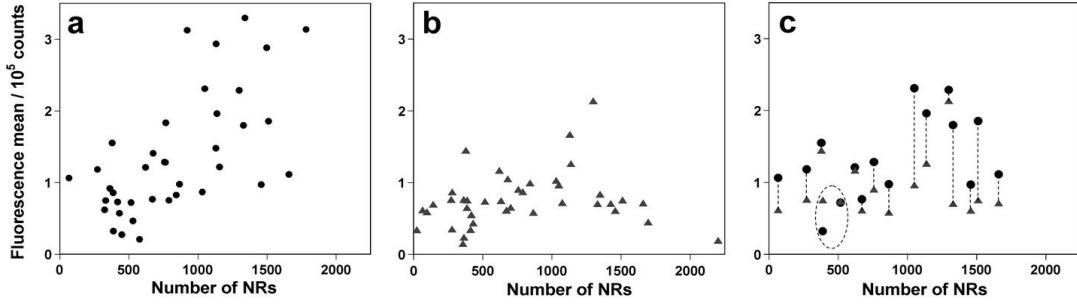


Figure 4.4. Mean fluorescence intensity vs. number of NRs for different clusters. a) “Fresh” NR clusters that were not (or only slightly) exposed to laser light prior to the 10 min measurement. b) “Aged” clusters that were exposed for ~25 min to laser light prior to the corresponding measurement. c) Comparison of 16 selected clusters that were measured “fresh” (black circles) and “aged” (gray triangles).

We find that NR orientation on the substrate relative to the laser polarization direction plays a role in determining the absolute fluorescence intensity of the clusters. In particular, it is expected that populations of NRs that are highly aligned (or perpendicular) to the laser polarization should increase (or decrease) the overall intensity. Since NRs couple to the laser field predominantly along their long axis, their emission intensity, I , depends on the angle, θ , between the NR long axis and the laser polarization, according to $I \sim \cos^2 \theta$. [Hu 2001] In this context, standing NRs are perpendicular to the laser polarization and exhibit a relatively small contribution to the overall observed intensity. Similarly, simulations of radiation from dipoles in micron-scale dielectric rod-shaped particles show zero-emission from the tip. [Li 2007] Indeed, by subtracting the number of standing NRs from the total number of NRs in each cluster, the linear trend from Figure 4.4a becomes slightly more pronounced with an improved coefficient of determination, R^2 , from 0.37 (all NRs) to 0.41 (corrected NRs) (Figure 4.11a). Similarly, clusters with a higher fraction of planar NRs aligned to the laser polarization exhibit a relatively higher emission (compare, e.g., clusters #3 and #4 in Table 4.1).

When studying the emission from clusters that have been exposed to laser light for \sim 35 min prior to the fluorescence measurement, *i.e.*, from the “aged” clusters, we observe an overall decrease in the mean intensity. Figure 4.4b shows the mean fluorescence intensity of 41 “aged” clusters. When comparing 16 specific clusters that have been measured both “fresh” and “aged” (Figure 4.4c), we observe that the extent of photodarkening is not the same for all of the clusters and that these variations are independent of the number of particles. The strongest decay occurred for clusters at the very center of the laser beam, *i.e.*, being exposed to the maximum laser intensity. In 2 out of 28 cases (indicated in Figure 4.4c), an increase in fluorescence intensity was observed. The decrease of fluorescence intensity in the majority of clusters, as well as memory effects, *i.e.*, the recovery of fluorescence after keeping the sample in the dark for some time, have been previously explained by Brokmann *et al.* for spherical nanocrystals in terms of statistical aging that results from power-law statistics governing single-particle blinking dynamics at short times. [Brokmann 2003]

4.3.3 Dependence of fluorescence fluctuations on particle number

In addition to studying the mean fluorescence intensity, examining fluctuations in the signal can also elucidate in more detail the underlying dynamics of single-particle blinking that influences the ensemble fluorescence of the clusters. One example of the time-dependent fluorescence intensity measured from a single NR on Si₃N₄ and the corresponding probability densities of on- and off-times are shown in Figure 4.12. In very small ensembles, containing only a few NRs (Figure 4.5a), we find that fluorescence fluctuations are similar to the single emitter “on/off” switching events. For example, the

fluorescence *vs.* time of a cluster containing 5 NRs (Figure 4.5a) shows clear blinking-like events, however, the minimum fluorescence intensity is higher than for an adjacent background segment, *i.e.*, the ensemble is always “on” during the measurement window of 25 min. A similar continuous, but weak, fluorescence signal during “dark” periods was observed for CdSe nanowires. [Glennon 2007, 2008, Protasenko 2005] With increasing numbers of particles, the minimum fluorescence intensity increases, but the blinking events remain superimposed, leading to significant fluctuations. These fluctuations can be as high as 40% of the mean fluorescence, even in clusters containing several hundreds or thousands of NRs (Table 4.1), though they tend to decrease with increasing particle number (Figure 4.11b), approximately with $\sigma/I_{mean} \propto N^{-0.5}$, which is consistent with the central limit theorem. For example, in a cluster containing ~9000 NRs the fluctuations were 2% of the mean fluorescence intensity.

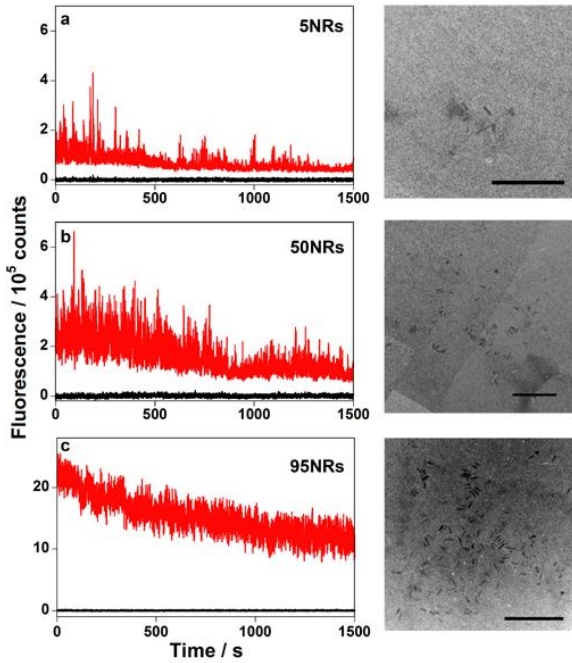


Figure 4.5 Fluorescence intensity *vs.* time and the corresponding TEMs (scale bar: 200 nm) for loose-packed ensembles containing a) 5 NRs, b) 50 NRs and c) 95 NRs (gray curves; the black lines are the corresponding background traces). The packing density of these ensembles was a) 477, b) 231 and c) 336 NRs/ μm^2 .

4.3.4 Fluorescence dynamics dependence on particle number ($N < 10000$)

The fluorescence intensity *vs.* time of this large cluster, containing 9000 NRs (Figure 4.6c), displayed another interesting feature: its mean fluorescence intensity increased during the measurement. Specifically, it reached a maximum intensity after ~ 350 s, approximately 10% higher than the initial value, before decreasing by $\sim 3\%$ during the final 250 s of the experiment. In smaller clusters containing several hundred or thousand NRs, such a pronounced fluorescence enhancement was never observed, though slight increases could be seen occasionally (Figure 4.3c). However, we find that in very small ensembles, such as the one containing 95 NRs (Figure 4.5c), the mean fluorescence intensity decays, similar to previous reports for spherical nanocrystals. To illustrate these different behaviors depending on the particle number, Figure 4.6 shows the fluorescence intensity *vs.* time curves, on a \log_{10} - \log_{10} scale, for three clusters containing 95, ~ 1500 and ~ 9000 NRs, respectively. To account for the different absolute fluorescence intensities, the data has been normalized with respect to the initial intensity, *i.e.*, the intensity measured directly after beginning exposure of the samples to laser illumination. All clusters were situated in the center of the laser beam, *i.e.*, illuminated with 100 W/cm². These data clearly show several types of time-dependence of the fluorescence intensity (within the measurement window of 10 or 25 min, respectively): (i) an exponential decay in small ensembles (Figure 4.6a, 95 NRs), (ii) an approximately constant fluorescence for “medium-sized” clusters (Figure 4.6b, 1500 NRs), and (iii) an increase in intensity, followed by a decrease, for large clusters (Figure 4.6c, 9000 NRs). These general types of fluorescence intensity time-dependence were also observed for other clusters of comparable size. Figure 4.6 also displays that the magnitude of relative

fluctuations, σ/I_{mean} , decreases by a factor of $\sim 3\text{-}4$ for each order of magnitude increase in particle number, *i.e.*, from 20% for 95 NRs, to 5% for 1500 NRs, and finally to 2% for 9000 NRs, in accordance with the central limit theorem as mentioned above. This decrease of relative fluctuations implies that single NR blinking events are averaged more with an increasing particle number.

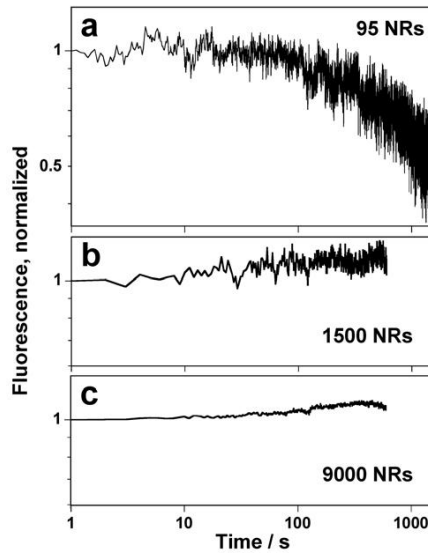


Figure 4.6 Normalized fluorescence intensity *vs.* time on a $\log_{10}\text{-}\log_{10}$ scale for NR clusters containing a) 95 NRs, b) ~ 1500 NRs and c) ~ 9000 NRs. The time resolution is 0.1 s (a) and 1 s (b,c);

From the above discussion and the data summarized in Table 4.1, it can be clearly established that there is significant cluster-to-cluster variation and that measurements from a single cluster are not necessarily always consistent with the overall trend obtained from a large number of clusters, outlined above. This can be illustrated with one example of three clusters (#5, #7 and #9 in Table 4.1) with similar percentages of standing NRs and NRs approximately aligned and perpendicular to the laser polarization, but with a different total number of NRs (671, 1051, and 1329 NRs, respectively). Among these clusters, the smallest (#5) is the darkest, as expected. However, the medium cluster (#7) is the brightest (Table 4.1). Importantly, this finding suggests that the variation in the

properties of individual NRs that compose the clusters contribute significantly to ensemble properties, at least for clusters in this size range. Consequently, there are no specific patterns or NR orientation to account for *all* the observed emission behaviors. Since larger clusters seem to be needed to average out the individual NR behavior, we proceeded to study such larger clusters by depositing a 5-times more concentrated solution.

4.3.5 Very large clusters ($N > 10000$) and long time-dependence of fluorescence

Figure 4.7a shows the fluorescence intensity *vs.* time on a \log_{10} - \log_{10} scale, recorded over a total of 18.6 hours, for NR clusters deposited from this more concentrated NR solution. This study at very long time-scales was used to further probe statistical aging effects. Curve NR1 corresponds to a cluster containing approximately 10000 NRs, and is comparable with the results discussed above (Figure 4.6c). It can be seen that after the initial period of almost constant intensity *vs.* time, the intensity decays at long exposure times, similar to the very small ensembles (Figure 4.6a); this decay occurs after ~ 100 s for $N \sim 100$ and after ~ 1000 s for $N \sim 10000$. We then considered larger numbers of particles, *i.e.*, $N \sim 50000$ NRs. Those were obtained by integrating the fluorescence of areas on the substrate containing several large clusters. We considered three regions of identical area ($7.5 \times 7.5 \mu\text{m}^2$) and similar cluster coverage that were located in different regions of the substrate and that were consequently exposed to different laser intensities (Figure 4.7c). Curve NR2 (black) corresponds to a cluster that was in the center of the beam, exposed to 100 W/cm^2 , whereas curves NR3 (blue) and NR4 (red) correspond to clusters located towards the periphery of the beam and exposed to ~ 50 and $\sim 25 \text{ W/cm}^2$,

respectively. Compared to the smaller cluster at the same illumination intensity (curve NR1 in Figure 4.7a), the larger cluster (curve NR2) shows a maximum intensity that is reached after \sim 2000 s. The decrease of illumination intensity from 100 to 50 W/cm² leads to a more pronounced fluorescence intensity peak that is shifted to \sim 5000 s (curve NR3 in Figure 4.7a). For curve NR4, the cluster illuminated at the lowest intensity (25 W/cm²), the fluorescence intensity does not reach a peak within the measurement time window (\sim 18.6 hours), but rather increases continuously. More specifically, we find that the onset of the power-law decay in ensemble fluorescence (*i.e.*, the time of the peak intensity) scales with the ratio of particle number and laser intensity, N/I_{laser} , *i.e.*, it scales inversely with the number of photons absorbed per NR.

For comparison, we have also measured the fluorescence of clusters containing spherical CdSe/ZnS core-shell nanocrystals on Si₃N₄ substrates with a similar number of particles. Figure 4.7b shows the fluorescence intensity *vs.* time for two regions with large nanocrystal clusters exposed to laser intensities of 100 and 25 W/cm² (Figure 4.7c). Both curves in Figure 4.7b show that the fluorescence intensity decreases in time, first at a slower rate (up to \sim 10 s) and then faster as a power-law. For the lower laser intensity, we observe that the fluorescence intensity decreases with time over the whole measurement range (curve NC2), while a higher laser intensity (curve NC1) leads to an approximately constant, apparently steady-state fluorescence, at very long times (>10000 s).

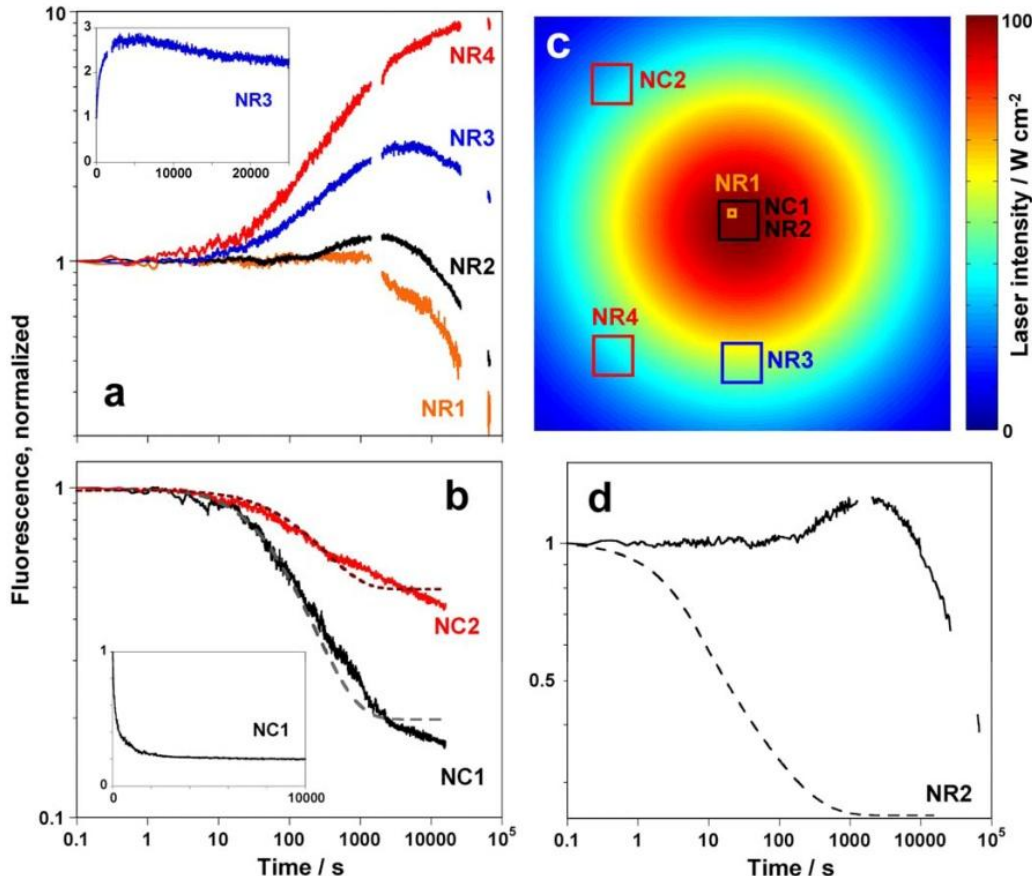


Figure 4.7 Normalized fluorescence intensity *vs.* time on a \log_{10} - \log_{10} scale for a) NR clusters containing ~ 10000 NRs (NR1, orange curve) and ~ 50000 NRs (NR2-NR4), as well as large clusters of b) spherical nanocrystals (NC1, NC2) with the associated fits from the statistical model derived from single particle blinking (parameters listed in Table 4.2). The insets show fluorescence intensity *vs.* time on a linear scale for NR3 and NC1, respectively. c) The laser beam intensity profile is well approximated by a Gaussian, with 100 W/cm^2 peak intensity. The field of view shown is $\sim 75 \times 75 \mu\text{m}^2$; the color scale bar indicates the intensity values. The large clusters (NR2-NR4, NC1-2) were irradiated with different laser intensities, due to their differing locations relative to the center of the beam. The sizes of the indicated squares reflect the sizes of the regions studied relative to the beam profile. d) The dashed line corresponds to the fit of the peak of trace NR2 (solid line) according to the statistical model proposed in Ref. [Chung 2004, 2006, 2007] (parameters listed in Table 4.2).

To directly compare NC and NR intensity *vs.* time curves, one needs to consider that the absorption cross-section of spherical nanocrystals is significantly smaller than of NRs with the same diameter, in this work, by a factor of ~ 20.14 . To effectively have an identical absorption rate per cluster, many more spheres are necessary, compared to NRs. Qualitatively, the intensity curve of nanocrystal clusters could correspond to that of NR clusters with a smaller number of particles measured at similar intensity (*e.g.*, NR1 and

NC1, Figure 4.7), suggesting that, in this situation, a single NR may be treated as a small cluster of a few spherical nanocrystals.

4.3.6 Statistical predictions of ensemble behavior based on single-particle dynamics

Fluorescence dynamics of nanoparticle ensembles results from the cumulative blinking behavior of single particles. The most popular current theory to explain single particle blinking assumes that neutral particles are “bright” and charged are “dark”. Fluctuation of charges on and around the particles can then result in fluctuations in the fluorescence signal, *i.e.*, blinking. Charge traps can originate from unpassivated surface atoms, *i.e.* surface transformations, [Hess 2001] defects within the quantum dot crystalline lattice and surface charges. [Krauss 1999, Krishnan 2004] Most previous studies of the role of environment [Verberk 2005, Cichos 2007] on single-particle blinking of the CdSe nanocrystal core and ensemble emission, such as the dielectric environment, [Issac 2005] the substrate [Uematsu 2005, Kimura 2004] and the surface passivation and atmosphere, [Koberling 2001, Müller 2004] support the above charge-trapping model, where traps are assumed to be either mobile or immobile. [Cichos 2007] The power-law statistics of blinking is robust for a wide range of experimental conditions, [Cichos 2007] *e.g.*, different atmospheres, ligands and temperatures. For particles with a thick shell, such as in this study, a similar power-law statistics of blinking occurs when particles are in air or in vacuum, [Müller 2004] implying that a similar statistical (time-dependent) behavior of ensembles is expected in both atmospheres. Nanocrystals with thick shells were reported to exhibit reduced blinking. [Chen 2008, Mahler 2008] Our combined experiments

support the theory that fluorescence properties of core-shell samples can be explained by the charge-trapping model.

The fluorescence measurements of spherical nanocrystal ensembles performed in our work can be qualitatively predicted by the particle number- and intensity-independent model by Chung *et al.* that provides a framework connecting single particle blinking behavior with ensemble fluorescence. [Chung 2004, 2006, 2007]

In general, single particles emit light intermittently with probability densities of on- and off-times which follow the relationship, $p_{on(off)}(t) = dP_{on(off)}(t)/dt$, where $1 - P_{on(off)}(t)$ are the cumulative distribution functions for on- and off-times, as expressed in Eq. 4.1, [Chung 2004, 2006, 2007]

$$1 - P_{on(off)}(t) = (1 + t/t_{on(off)}^{\min})^{-\alpha_{on(off)}} \cdot \exp(-t/\tau_c^{on(off)}) \quad (\text{Eq. 4.1})$$

where $p_{on(off)}$ is the probability density of on(off)-time; $\tau_c^{on(off)}$, denoted as $t_{on(off)}^{\max}$ in Ref. [Chung 2004, 2006, 2007], are the characteristic “truncation” times of the probability densities of on- and off-times, approximately marking the truncation of the probability density from a power-law into an exponential dependence in time; $t_{on(off)}^{\min}$ are the minimum durations of individual “on” and “off” blinking events, and $\alpha_{on(off)}$, denoted as $\mu_{on(off)}$ in Ref. [Chung 2004, 2006, 2007], are the power law exponents of the cumulative distribution functions.

The time-dependent ensemble fluorescence is described by the summation of the individual particle emission intensities *vs.* time. It is proportional to the probability function of a collection of emitting nanocrystals, $f_{on}(t)$, which is derived from the

probability densities of on- and off-times of single emitters and can be expressed analytically in its Laplace transform, [Chung 2004, 2006, 2007]

$$f_{on}(s) = \frac{\alpha + (1-\alpha) \cdot p_{off}(s)}{1 - p_{off}(s) \cdot p_{on}(s)} \cdot \frac{1 - p_{on}(s)}{s} \quad (\text{Eq. 4.2})$$

where α is the fraction of nanocrystals which are initially “on” at time $t=0$ and $p_{on(off)}(s)$ are the Laplace transforms of single emitters’ on- and off-time probability densities, $p_{on(off)}(t)$. The observed fluorescence properties of ensembles therefore depend on the nature of single-particle blinking, and we further tested the applicability of this model against known parameters derived from our previous measurements of single particle blinking.[Wang 2006, Cichos 2007]

To compare the model to experimental ensemble intensity *vs.* time curves, we generated $f_{on}(t)$ by setting α , $t_{on(off)}^{\min}$, $\tau_c^{on(off)}$, and $\alpha_{on(off)}$ to specific values, as discussed below, and by numerically calculating the inverse Laplace transform of Eq. 4.2. Simplified approximations of $f_{on}(t)$ valid over restricted time ranges, together with the known single particle blinking parameters, were used to estimate the range of values of α_{on} , α_{off} , τ_c^{on} and τ_c^{off} from the experimental intensity *vs.* time curves. Specifically, for $t < \tau_c^{on}$, $f_{on}(t) = \text{const}$ when $\alpha_{on} = \alpha_{off}$ and it increases as $f_{on}(t) \propto 1 - A \cdot t^{-(\alpha_{off} - \alpha_{on})}$ for $\alpha_{on} < \alpha_{off}$. For $\tau_c^{on} < t < \tau_c^{off}$, $f_{on}(t) \propto t^{-(1-\alpha_{off})}$. These facts were used to estimate α_{on} and α_{off} from the slopes of the ensemble intensity *vs.* time curves. The truncation times of the on- and off-time probabilities of single nanocrystals, τ_c^{on} and τ_c^{off} , were approximately determined as the times at the onset of the power law decay and the crossover between the power law decay and the long time steady state, respectively. Additionally, the

theoretical curves are not sensitive to the specific value of α ($\alpha = 0.5$ was used in Figure 4.7b) since the value of α affects $f_{on}(t)$ only at short times, outside of the time range in our measurements. Finally, $t_{on(off)}^{\min}$ are the minimum durations of individual blinking events and they do not affect the theoretical curves at timescales of our measurements. Given the number of parameters in the model, it was not feasible to determine their values *via* least square fitting, and therefore, we iterated the values of $t_{on(off)}^{\min}$, $\tau_c^{on(off)}$, and $\alpha_{on(off)}$ over a physically meaningful range until we generated a theoretical curve, $f_{on}(t)$, that best fits the experimental time trace over the full time range.

Figure 4.7b shows two theoretical curves (dashed lines) of the fluorescence intensity *vs.* time for nanocrystal ensembles (NC1 and NC2) at two different excitation intensities (see the positions of NC1 and NC2 in Figure 4.7c). The parameters used to generate these theoretical curves are listed in Table 4.2. Unlike the NR ensemble emission (Figure 4.7a), no initial brightening was observed for spherical nanocrystals. According to the model, this implies that $\alpha_{on} = \alpha_{off}$, determined from the theoretical curves to be 0.55 and 0.64 for excitation intensities of 100 and 25 W/cm², respectively, consistent with previous single nanocrystal measurements. The corresponding truncation times of on-time probabilities from the theoretical curves are $\tau_c^{on} \sim 16$ s and ~ 30 s for excitation intensities of 100 and 25 W/cm², respectively. These values of τ_c^{on} and the fact that τ_c^{on} decreases with increasing excitation intensity are also consistent with single particle measurements. The model also yields $\tau_c^{off} \sim 1500$ s and 800 s for excitation intensities of 100 and 25 W/cm², respectively.

To explore the possibility that decay in fluorescence at long times could be due to chemical or physical aging, we sampled the blinking probability distributions of single nanocrystals at a range of times throughout a very long measurement (~6 h). Within this time window, we studied seven single NRs and verified that the “on” and “off” probability distributions of single NRs are not time dependent: α_{on} and α_{off} did not vary more than 6% and 2% respectively, while τ_c^{on} varied by 25% (Figure 4.12), which is still within the variation of τ_c^{on} among different single NRs. No systematic trends were evident in these variations. We also note that the NRs measured consist of a double-shell structure and are less prone to bleaching than, for example, core-only nanoparticles. Most of the data in this paper are covered by several hours, for example, the observation of intensity peaks at ~5000 s. Even without any physical aging, the ensemble fluorescence should decay in time at long times before it reaches steady-state (*i.e.*, it should “statistically” age), so fluorescence decay does not necessarily mean that the sample is chemically or physically changing (*e.g.*, oxidation in air or the removal of ligands under vacuum); however, we cannot completely exclude chemical and physical changes as a possible partial explanation of why some data might deviate from the statistical model.

4.3.7 Deviations from the statistical model

According to the statistical model, the maximum fluorescence intensity of ensembles should occur at a time approximately equal to τ_c^{on} , implying that τ_c^{on} should be ~5000 s for NRs (see for example curve NR2 in Figures 4.7a,d). However, this value is larger than that from single NR measurements ($\tau_c^{on} \sim 1$ s) and represents a clear deviation from

the model. Despite this quantitative discrepancy, we observe that the maximum of the fluorescence intensity shifts to longer times for lower laser intensity (Figure 4.7a, curves NR2-4), which in turn implies a longer τ_c^{on} for lower laser intensity and is further consistent with our previous measurements of individual NRs. To illustrate the expected fluorescence from the statistical model, Figure 4.7d also shows a calculated fluorescence intensity *vs.* time curve (dashed line) where the values of $\alpha_{on(off)}$ and τ_c^{on} were taken from single NR measurements ($\alpha_{on} \sim 1.42$, $\alpha_{off} \sim 1.30$ and $\tau_c^{on} \sim 1.39$ s), while the remaining parameters, α , $t_{on(off)}^{\min}$, and τ_c^{off} were assumed to be identical to those used to generate the theoretical curves for nanocrystals (see Table 4.2). While α and $t_{on(off)}^{\min}$ do not influence the curve in the time range shown, the value of τ_c^{off} influences the slope of the fluorescence decay and the beginning of the steady state. The onset of the fluorescence decay occurs at $t \sim \tau_c^{on} \sim 1$ s, as would be expected from single NR measurements.

Table 4.2. Fitting parameters used to generate the theoretical intensity *vs.* time curves of nanocrystal and NR ensembles, shown in Figures 4.7b,d.

	α	α_{off}	α_{on}	$t_{on(off)}^{\min}$	$t_{on(off)}^{\min}$	$t_{on(off)}^{\min}$	$t_{on(off)}^{\min}$
NC1	0.5	0.55	0.55	10^{-5}	10^{-6}	16	1500
NC2	0.5	0.64	0.64	10^{-5}	10^{-6}	30	800
NR2	0.5	0.32	0.26	10^{-5}	10^{-6}	1.32	1500

To accurately describe the experimental data, the statistical model developed in Ref. [Chung 2004, 2006, 2007] will need to be extended in the future to include the intensity and particle number dependence of the individual blinking parameters. In particular, because the onset of the power law decay scales inversely with the number of photons absorbed per NR, as discussed above, τ_c^{on} should scale as N/I_{laser} .

An important assumption in this model is that individual nanoparticles are treated as independent emitters. This assumption may be justified, given that the probability for charges to tunnel from one NR core to the other is relatively small, since the NRs have a shell (~ 2 nm) and relatively long insulating ligands (~ 2 nm), and the tunneling probability decreases exponentially with NR-NR separation.

4.4 Conclusions

In conclusion, we studied the time-dependence and fluctuations of the fluorescence from CdSe-based core-shell NR clusters from single particles to over 10000 particles using correlated fluorescence imaging, AFM, and TEM. While it has been previously shown that single NRs emit light intermittently, we report here that small ensembles of as few as 5 NRs can exhibit, in addition to single particle-like events, a weak, non-zero fluorescence during “dark” periods, within the measurement time window. Larger clusters, containing several thousands of NRs, exhibit fluorescence approximately constant in time (over tens of minutes) that shows pronounced fluctuations which can be attributed to contributions from single particle blinking events. For even larger clusters these intensity fluctuations, decrease relative to the mean intensity since single particle events are averaged out following the central limit theorem.

The fluorescence intensity of NR clusters is time-dependent over long time scales (hours), exhibiting two characteristic trends: either, the intensity can decrease in time, or, the intensity first increases to a maximum and then decays in time according to a power-law. The nature of the time-dependence depends on the number of NRs and the laser intensity. As the particle number increases (at constant laser intensity), the time

dependence goes from an intensity decay for ensembles of up to ~ 100 particles to the presence of a peak in intensity for ensembles with ~ 1000 particles or more. As the laser intensity decreases while N remains constant, the intensity peak shifts to longer times. Thus the onset of the power-law decay scales inversely with the number of absorbed photons per NR. We have discussed these observations in the context of a previously proposed statistical model derived from the behavior of single particle blinking.

4.5 Supplementary Information

4.5.1 Details on direct particle counting

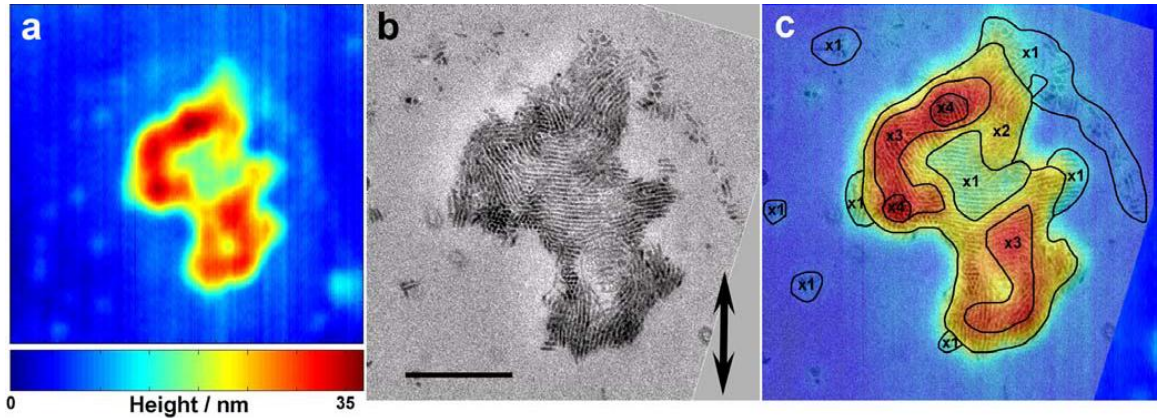


Figure 4.8 a) AFM image of cluster #32 (Table 4.4). b) TEM of the same cluster. The scale bar is 200 nm. The TEM image is rotated to account for the orientation of the cluster with respect to the laser polarization, which is vertically in the plane of the page, indicated by the arrow. c) Superposition of AFM and TEM images to identify regions of monolayers (light turquoise, “x1”), two layers (yellow/light orange, “x2”), three layers (red, “x3”) and four layers (dark red, “x4”). From the comparison, it can be seen that the highest regions of the cluster correspond to the standing NRs, whose length of ~ 38 nm is approximately equivalent to the thickness of four in-plane monolayers since the NR diameter is ~ 8 nm (with organic ligands).

To estimate the total number of particles, we first superpose AFM and TEM images to identify regions of different heights in the cluster corresponding to one, two, three or four layers (Figure 4.8c). For each of these regions, we count the visible NRs in the TEM image, *i.e.*, the top-layer, as a function of their orientation with respect to the laser polarization (arrow in Figure 4.8b) as summarized in Table 4.3. The total number of

particles, *i.e.*, 1032 NRs, is then obtained by multiplying the number of NRs in the top-layer by the number of layers. Only the number of particles in monolayers and upright NRs can be counted accurately. In multiple layers, we estimate an error of $\sim 5\%$ per layer, because we assume a similar packing density of the NRs in the sub-layers. Moreover, the transition between different layers is slightly “washed out” due to the lateral resolution of the AFM.

Table 4.3 Orientation with respect to the laser polarization.

layers	vertical	in plane			total
		$\pm 30^\circ$	$\pm(30-60)^\circ$	$\pm(60-90)^\circ$	
x1	75	16	41	108	165
x2		9	0	27	72
x3		128	44	60	696
x4		4	0	2	24
%	7%	33%	18%	42%	1032

Similarly, for the angular distribution, only the top-layer is taken into account. Considering the extent of ordered structures in the top-layer, it is reasonable to assume that a similar degree of orientation occurs in the sub-layers. Additionally, most clusters (Table 4.4) show overall a relatively random orientation which makes it unlikely that the sub-layer is significantly more ordered.

Table 4.4 Summary of structural parameters of studied NR clusters

Cluster	Number of NRs ^a	Area (μm^2) ^b	NR layers ^c	Cluster density (NRs/ μm^2)	vertical (%)	NR orientation ^d			$I_{\text{mean}} (\text{counts})^e$ (σ/I_{mean})
						in plane (%)	$\pm(0-30^\circ)$	$\pm(30-60^\circ)$	
1	1499	0.26	4	5857	7	24	34	35	288000 (5%)
2	1784	0.28	4	6448	11	40	21	28	314000 (5%)
3	764	0.09	3	8550	9	30	38	23	128000 (15%)
4	1051	0.17	3	6063	41	16	20	23	231000 (18%) *97000 (22%)
5	1329	0.23	3	5893	38	19	20	23	180000 (18%) *71000 (28%)
6	671	0.07	4	9420	34	19	24	24	77000 (31%) *61500 (27%)
7	1132	0.17	3	6851	3	56	17	23	294000 (7%)
8	449	0.11	3	4144	0	28	25	48	27300 (12%)
9	418	0.05	3	9015	2	58	8	32	72800 (28%) *55600 (38%)
10	388	0.11	4	3526	0	15	57	29	32400 (40%) *76000 (32%)
11	1696	0.25	4	6791	7	47	26	19	*45500 (22%)
12	279	0.04	4	8305	5	76	11	9	*87400 (48%)
13	~9000	1.26	7	~7141	6	no angular analysis			5882400 (2%)
14	530	0.13	3	3993	0	31	22	47	46700 (7%)
15	676	0.18	4	3840	0	45	21	34	141000 (10%)
16	1341	0.24	4	5642	4	31	22	42	330000 (7%)
17	768	0.11	3	7150	7	31	35	27	183500 (10%)
18	323	0.04	4	8474	0	61	19	21	61900 (23%)
19	332	0.08	4	4288	3	31	23	43	75000 (22%)
20	577	0.11	3	5378	10	37	15	38	20800 (22%)
21	922	0.09	4	10810	20	37	17	27	313000 (16%)
22	1157	0.14	4	8322	9	30	28	33	122000 (13%)
23	1660	0.22	4	7564	24	36	20	20	111000 (20%) *71800 (35%)
24	432	0.06	3	7564	21	20	20	40	57300 (34%) *43800 (40%)
25	1458	0.19	3	7609	56	25	10	9	97200 (26%) *61400 (35%)
26	759	0.14	3	5449	25	34	22	19	128000 (19%) *90800 (19%)
27	866	0.12	3	7010	11	27	22	39	97600 (18%) *58800 (23%)
28	362	0.06	3	5580	4	28	34	34	91800 (30%) *76800 (17%)
29	1129	0.13	4	8419	14	34	32	21	148000 (20%) *167000 (11%)

Cluster	Number of NRs ^a	Area (μm^2) ^b	NR layers ^c	Cluster density (NRs/ μm^2)	upright (%)	NR orientation ^d			$I_{\text{mean}} (\text{counts})^e$ (σ/I_{mean})
						$\pm(0-30^\circ)$	$\pm(30-60^\circ)$	$\pm(60-90^\circ)$	
30	378	0.05	3	8325	20	21	31	28	155000 (21%) *145000 (20%)
31	621	0.09	4	6875	20	12	22	46	121000 (19%) *117000 (14%)
32	1032	0.16	4	6555	7	33	18	42	87100 (31%) *103000 (14%)
33	1298	0.17	3	7597	23	19	33	25	229000 (16%) *214000 (16%)
34	386	0.08	3	5070	11	22	37	30	85700 (23%) *65500 (21%)
35	272	0.08	3	3328	19	35	24	23	118000 (31%) *76800 (51%)
36	66	0.02	2	2971	0	33	51	16	107000 (29%) *62200 (31%)
37	516	0.06	3	8370	18	14	30	38	72200 (25%) *74200 (24%)
38	1137	0.18	3	6174	3	42	25	30	196000 (12%) *127000 (10%)
39	1511	0.22	4	6967	43	7	15	35	185000 (16%) *75900 (22%)
40	843	0.13	4	6489	22	27	25	25	82500 (32%) *99800 (28%)
41	789	0.10	3	7558	5	24	44	26	75200 (27%) *87400 (27%)
42	1075	0.24	4	4452	4	29	27	39	*72500 (26%)
43	682	0.12	3	5639	0	26	41	33	*105000 (16%)
44	634	0.15	4	4350	0	44	26	30	*75000 (24%)
45	364	0.06	3	6168	15	22	23	40	*24200 (50%)
46	413	0.04	3	11683	9	46	9	36	*34900 (45%)
47	1426	0.14	4	9984	3	no angular analysis			*71400 (21%)
48	143	0.03	2	4198	0	52	19	30	*70100 (25%)
49	1348	0.20	4	6645	6	no angular analysis			*84100 (15%)
50	672	0.09	4	7869	7	no angular analysis			*61900 (29%)
51	702	0.09	4	7640	10	no angular analysis			*65700 (28%)
52	278	0.04	4	7399	0	49	41	10	*35400 (81%)
53	356	0.13	3	2801	0	40	27	33	*15600 (52%)
54	97	0.03	1	3257	0	34	38	28	*59700 (19%)
55	23	0.17	1	136	0	52	13	35	*34700 (49%)
56	2202	0.45	4	4926	5	25	29	40	*19900 (30%)

^aNumber of particles estimated by direct counting of top layers from TEM image and extrapolation for sub-layers assuming similar particle packing. ^b Cluster area determined from TEM images with ImageJ software. ^c Maximum number of NR layers constituting the cluster determined from height analysis with AFM. ^d Orientation of the NRs with respect to the substrate (vertical or in plane) and with respect to the laser polarization. ^e Mean fluorescence intensity, mean, and standard deviation, σ , indicated in percent of I_{mean} . The data preceded by an asterisk are for “aged” NR clusters, *i.e.*, those exposed to light prior to the fluorescence measurement.

4.5.2 Additional transmission electron and atomic force micrographs of NR clusters

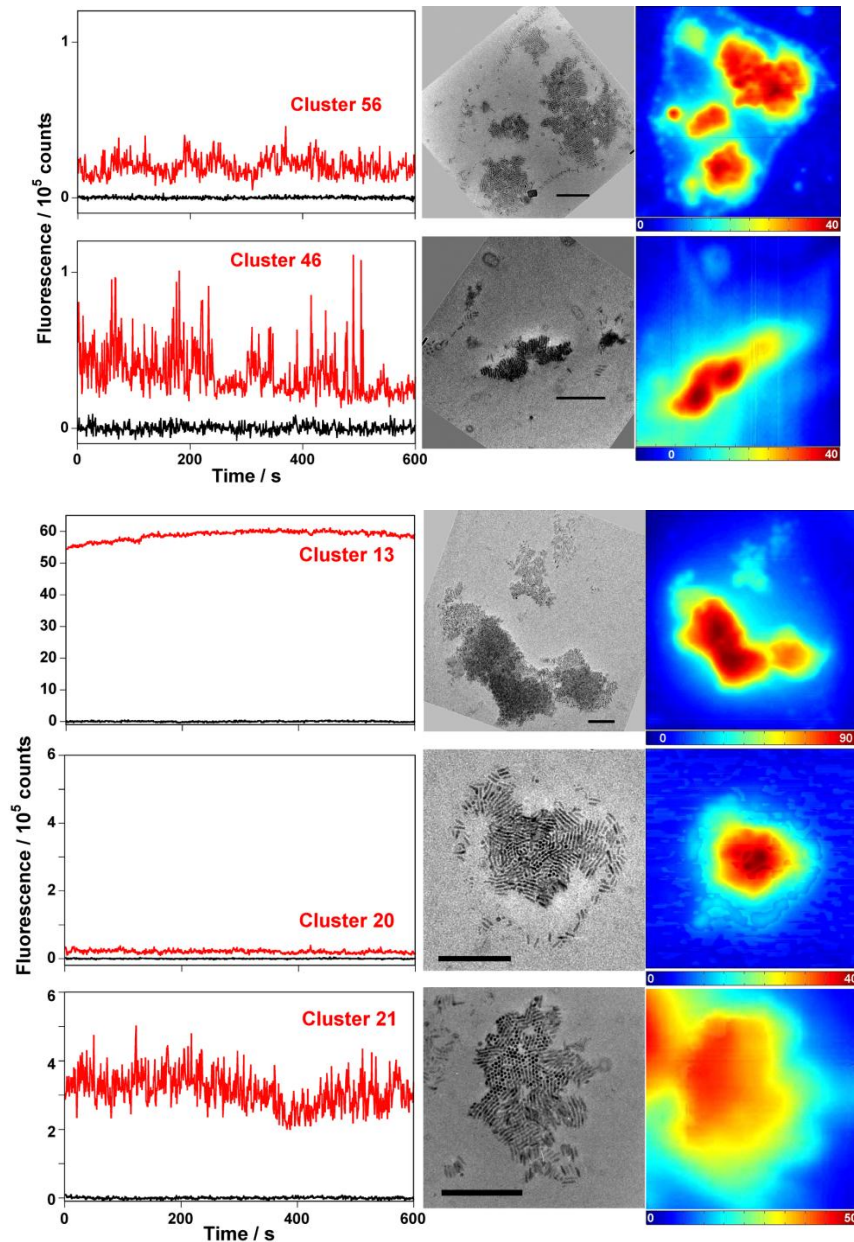


Figure 4.9 TEM and AFM images of close-packed “fresh” NR clusters and their corresponding fluorescence vs. time. The TEM images (scale bar: 200 nm) are rotated to account for the orientation of the cluster with respect to the laser polarization, which is vertically in the plane of the page. The cluster labels refer to the entries in Table 4.4.

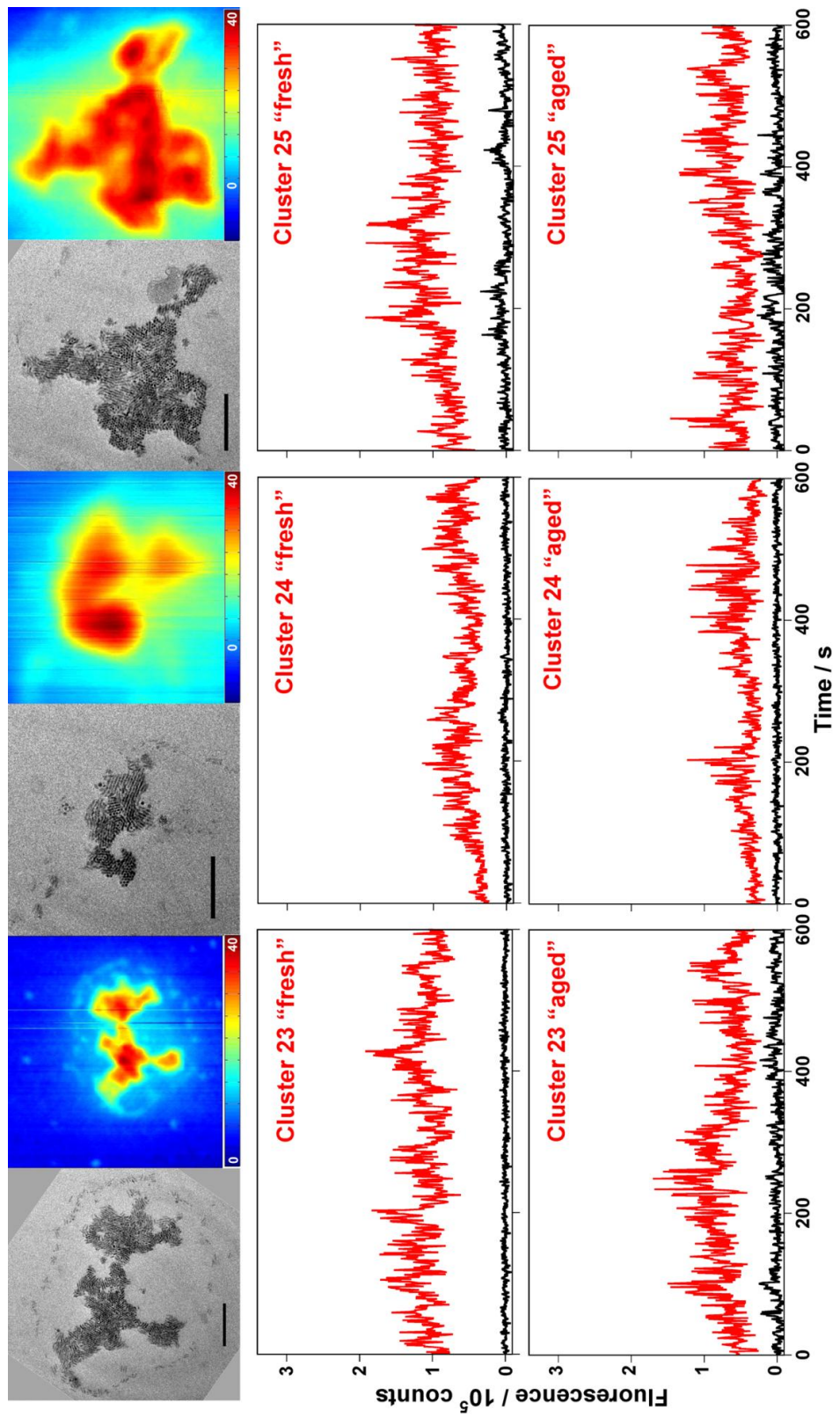


Figure 4.9(continued). TEM and AFM images of close-packed NR clusters, measured both “fresh” and “aged”, and their corresponding fluorescence vs. time traces. The TEM images (scale bar: 200 nm) are rotated to account for the orientation of the cluster with respect to the laser polarization, which is vertically in the plane of the page. The cluster labels refer to the entries in Table 4.4.

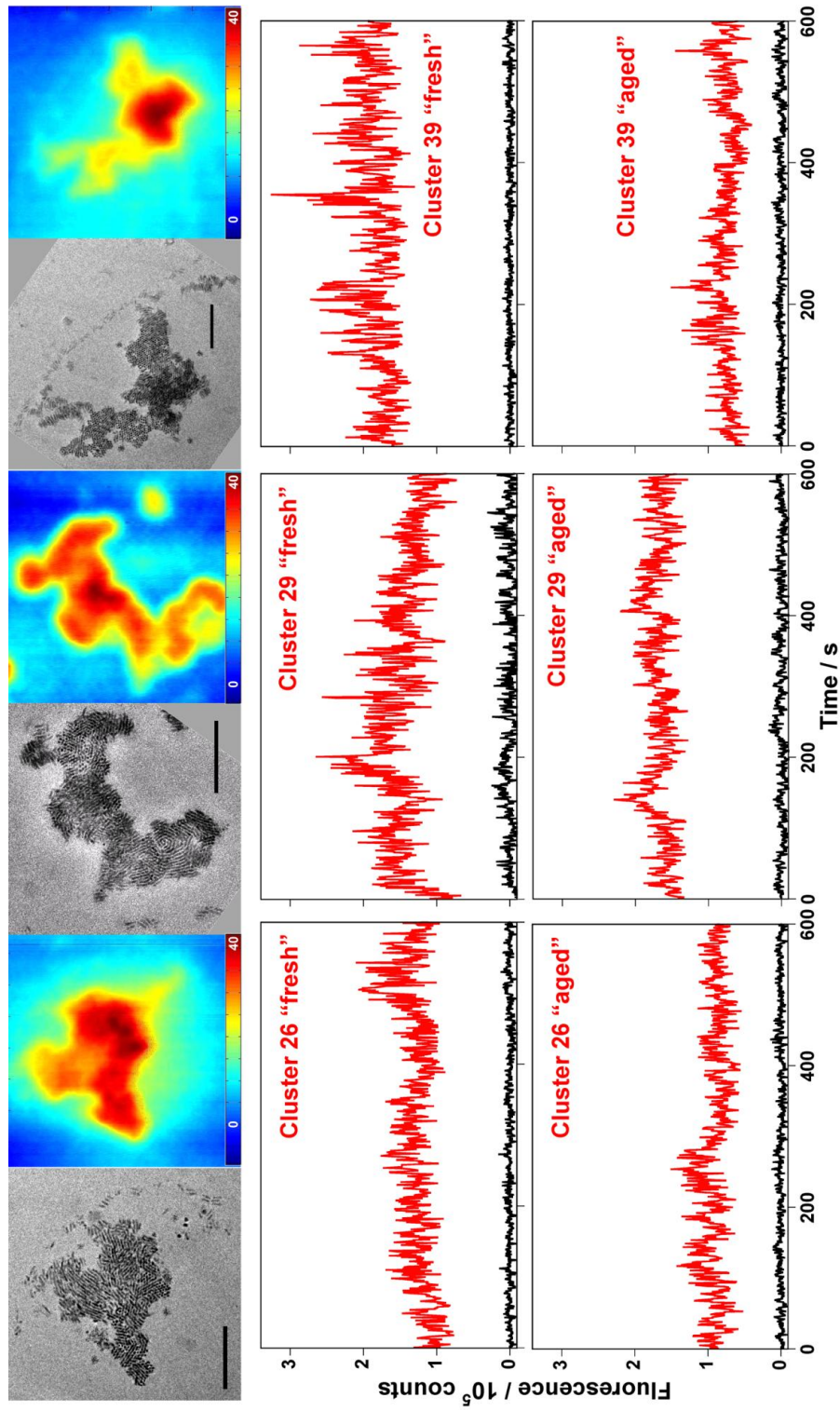


Figure 4.9 (continued). TEM and AFM images of close-packed NR clusters, measured both “fresh” and “aged”, and their corresponding fluorescence vs. time traces. The TEM images (scale bar: 200 nm) are rotated to account for the orientation of the cluster with respect to the laser polarization, which is vertically in the plane of the page. The cluster labels refer to the entries in Table 4.4.

4.5.3 Additional correlations of structural and fluorescence parameters of NR clusters

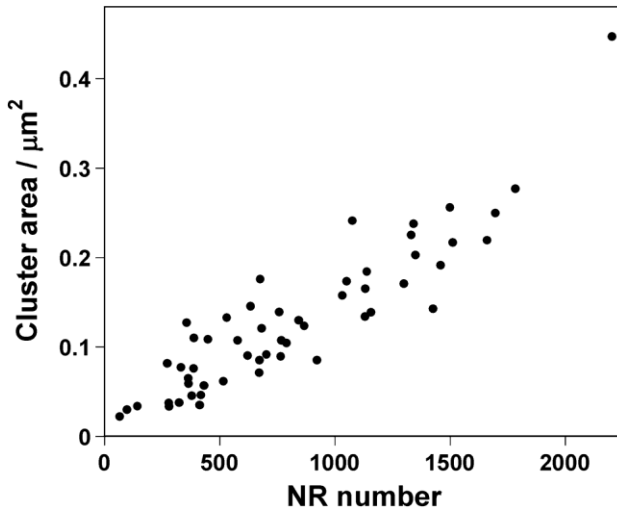


Figure 4.10 Cluster area vs. total number of NRs shows an approximately linear increase. The spread around the slope of $\sim 6000 \text{ NRs}/\mu\text{m}^2$ is partially accounted for by the varying cluster thickness between 2 and 4 monolayers (Table 4.3).

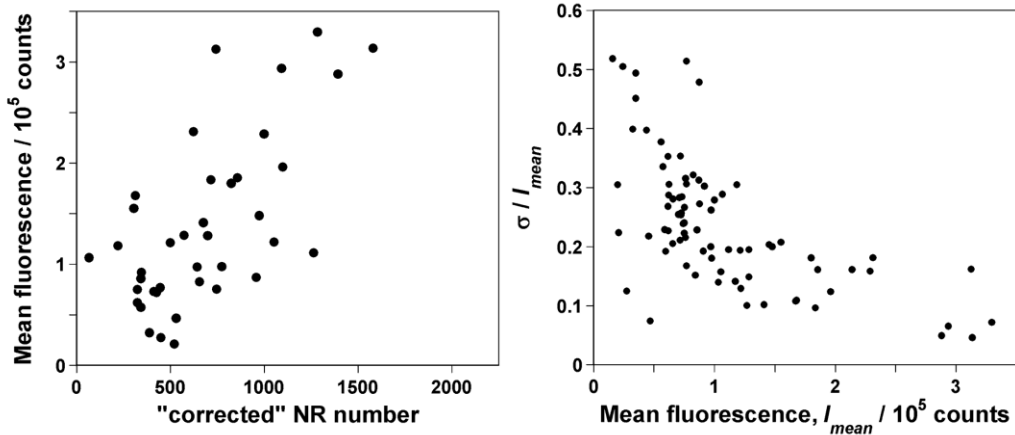


Figure 4.11 a) Mean fluorescence intensity vs. number of in-plane NRs. This “corrected” NR number is used to investigate the effect of vertically oriented NRs that are expected to contribute significantly less to the overall cluster fluorescence compared to NRs that are in plane and aligned to the laser polarization (compared to Figure 4.4a). b) Standard deviation of fluorescence fluctuations (relative to the mean fluorescence intensity) vs. mean fluorescence intensity. Relative fluctuations decrease with increasing intensity, *i.e.*, with increasing cluster size and increasing number of particles. In the limit of large clusters, such as cluster #13 containing ~ 9000 NRs (not shown in Figures 4.10 and 4.11), the fluctuations are as low as 2% (Table 4.4).

4.5.4 Fluorescence vs. time of individual NR on Si₃N₄

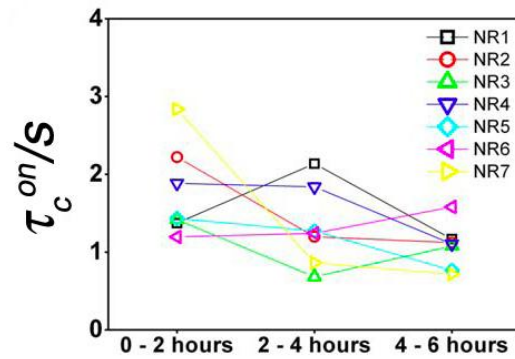


Figure 4.12 Statistical analysis of 6 h-long movies of 7 different individual NRs divided into three 2 h-long segments: τ_c^{on} varies by 25%, which is still within the variation of τ_c^{on} among different single NRs. No systematic trends were evident in these variations.

Chapter 5

Collective fluorescence enhancement in nanoparticle clusters

5.1 Introduction

A system's complexity is often tied to its statistical properties. In chemical systems, complexity of the environment results in the fluorescence intermittency or “blinking” displayed by many types of single emitters, such as single molecules, green fluorescent proteins, light harvesting complexes, organic fluorophores, and semiconductor nanoparticles. The fluorescence intensity stochastically changes between bright and dark regimes, commonly referred to as on- and off-states. Furthermore, this blinking does not follow a simple two-level quantum jump model, but instead displays approximately power-law (Lévy) statistics over many decades in time. Similar non-Poissonian statistics have been observed in electron transport through colloidal nanocrystal (NC) arrays.

[Novikov 2005]

The origin of the observed Lévy statistics has been the subject of extensive investigation, with several models proposed in the fifteen years since the first observation of power-law blinking. Although the details of the mechanism are still poorly understood, it is thought that NCs become “dark”, cease emitting light, when one of the charge carriers in a photoexcited exciton becomes trapped at the surface of the NC or tunnels off the NC into the environment, leaving a net charge delocalized in the NC core. In the charged core, highly efficient Auger processes lead to rapid nonradiative recombination of subsequent photoexcited excitons. Fluorescence then resumes once the core regains

electrical neutrality. Recently, the Krauss and Klimov's groups observed near-complete suppression of blinking in NCs synthesized with graded shells that greatly reduce the efficiency of Auger recombination, providing strong support for the proposal that dark states involve Auger recombination. [Wang 2009, Garcia-Santamaria 2009]

While fluorescence from single nanoparticles and from macroscopic ensembles has been studied extensively, there has been little study of fluorescence from small ensembles with the potential for interactions. In this chapter, we investigate blinking in small clusters of semiconductor colloidal nanorods (NRs) with known numbers of particles, N . Remarkably, the cluster fluorescence exhibits collective behaviour: we observe roughly N -fold enhancement of the durations of bright periods (“on-times”), compared to the combined fluorescence durations from N separate NRs. This observed effect of interactions can be figuratively described as a “campfire effect”: while clustering particles together does not help start the “fire,” i.e. off-times in a cluster are indistinguishable from those for the same number of independent NRs, grouping particles in a cluster does extend the “burning,” i.e. the on-times are strongly increased. The scaling of this interaction-induced increase of on-time durations with the cluster size reveals a novel collective effect in fluorescence at the nanoscale. Our study emphasizes the use of statistical properties in identifying the collective dynamics, and suggests that small nanorod clusters may be usable as nanoscale light sources with very long emission times.

5.2 Experimental Methods

We used the same experimental method and data analysis as those described in Section 3.2 to investigate the possible interactions in NRs. For this study, we still used TOPO-capped CdSe/ZnSe/ZnS core/double shell semiconductor NRs, with a 5.8 nm wide by 34 nm long optically active CdSe core and an overall size of 8 nm by 38 nm (details of synthesis and characterization are given in Supplementary Information 3.5.1).

NR solutions in toluene were deposited onto the substrate by drop-casting (7 μL). In order to obtain enough clusters of NRs, a fairly high concentration of NRs ($\sim 10 \text{ nM}$) was deposited on the substrate, producing many extended regions in which individual clusters were not optically resolvable; we only analyzed data from clusters optically resolvable from their neighbors (see Section 3.5.2). The analysis of thresholding and subsequent digitizing was previously described in Section 3.5.3 and the conclusions in this chapter hold qualitatively for a range of thresholds (Supplementary Information 5.5.1).

Fluorescence data collected from independent measurements on two different chips match very well (see Supplementary Information 5.5.2). Statistical analysis of various temporal sub-segments within the fluorescence movie showed no significant or systematic change in the blinking parameters of single NRs over the duration of the experiment. [Querner 2008] Still, effects of sample degradation over time cannot be excluded. Some clusters become dark over the course of the experiment, in which case the maximum on-times reported in Figure 5.4 may be smaller than what may be possible otherwise.

5.3 Results and Discussion

5.3.1 Fluorescence intensity of NR clusters correlated with the number of NRs, N

We analyzed the fluorescence intensity *vs.* time, $I(t)$, of NR clusters containing $N = 1$ to ~ 100 nanoparticles (N for each fluorescence source is determined by TEM imaging), as illustrated in Figure 5.1. Figure 5.1a and 5.1b shows fluorescence and TEM images of a $18 \times 12 \mu\text{m}^2$ region on the $175 \times 175 \mu\text{m}^2$ Si_3N_4 membrane window (50 nm thickness), patterned with a grid of gold lines, composed by combining 84 high-resolution TEM images. Figure 5.1c shows fluorescence intensities, $I(t)$, in the order of increasing particle number, $N = 2, 3, 5, 9, 18$, and 56, with the corresponding TEM images (Figure 5.1d).

5.3.2 Role of interactions in blinking statistics

As we discussed in the previous chapters, in NCs and NRs, the probability density function (PDF) of on-times has been observed to follow a truncated power law as a function of on-time, t_{on} , [Chung 2004, Tang 2005a, Wang 2006] $P(t_{on}) \propto t_{on}^{-\alpha_{on}} e^{-t_{on}/\tau_c^{on}}$, where $1 < \alpha_{on} < 2$ is the power-law exponent. The time, τ_c^{on} , is the truncation time, *i.e.*, the crossover time between two regimes: the power law at short times and the exponential at long times. At low excitation rates, single NCs typically display $\tau_c^{on} > 10$ s while for single NRs, τ_c^{on} is in the range of 1-10 s, with larger aspect ratio NRs giving smaller τ_c^{on} . [Wang 2006] Increasing the excitation power decreases τ_c^{on} . [Shimizu 2001, Tang 2005a, Peterson 2009] The PDF of off-times similarly follows a truncated power law

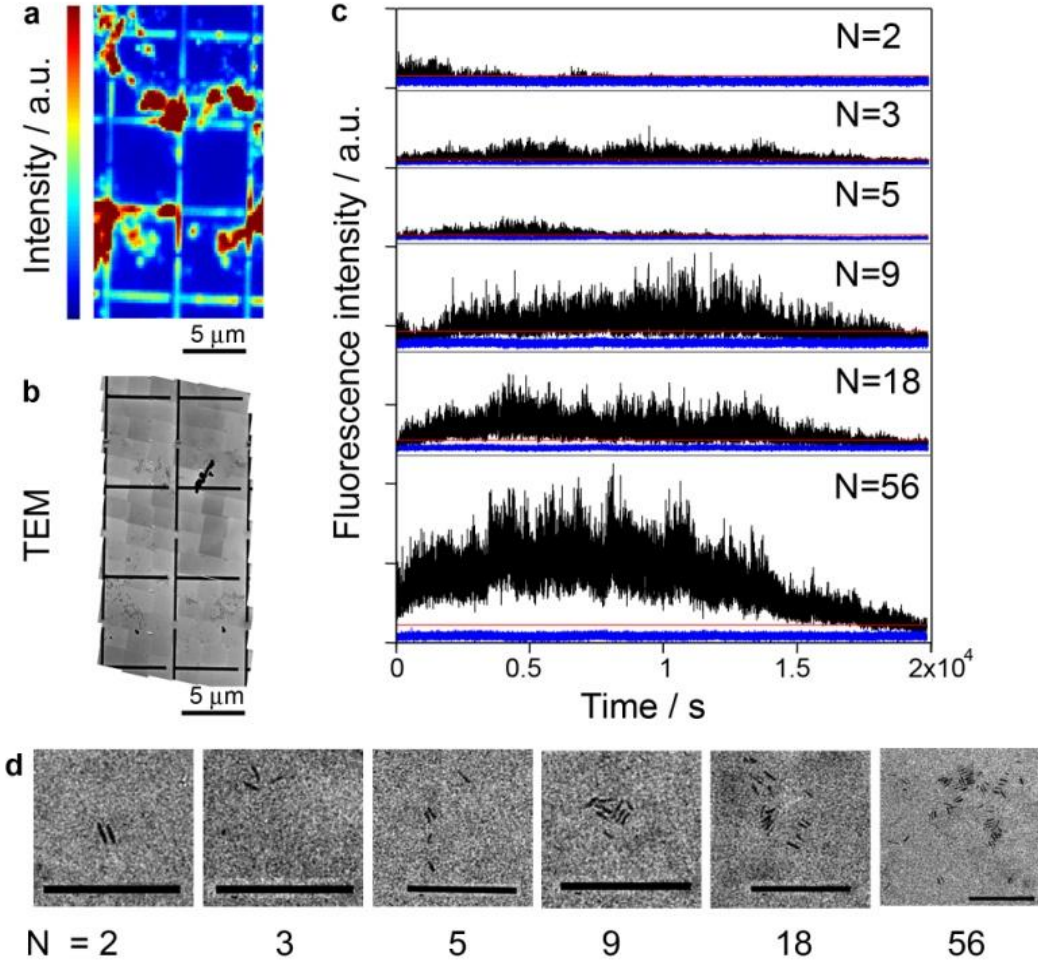


Figure 5.1 a) Fluorescence and b) TEM images of a $18 \times 12 \mu\text{m}^2$ region on the $175 \times 175 \mu\text{m}^2$ Si_3N_4 membrane window (50 nm thickness), patterned with a grid of gold lines, and (b) was composed by combining 84 high-resolution TEM images. c) Fluorescence intensities, $I(t)$, in the order of increasing particle number, $N = 2, 3, 5, 9, 18, 56$, background signals (blue curves) and threshold levels (red lines), recorded over 6 hours. d) TEM images corresponding to the clusters in (c). The scale bars in (d) on all TEM images are 200 nm.

with the corresponding power-law exponent $\alpha_{off} \sim 1.3$ and the truncation time $\tau_c^{off} \sim 1000$ s in NRs. [Wang 2008]

We now turn our attention to the clusters of NRs. Although it has been shown that blinking statistics are threshold-dependent when the threshold is varied significantly, [Wang 2008, Frantsuzov 2009, Crouch 2010] our analysis confirms that the trends reported here hold for a wide, reasonable range of thresholds (see Section 3.5.1). All

results reported in this chapter were determined using a threshold of $m_{dark} + 7\sigma_{dark}$ chosen to lie above the background signal from the bare substrate.

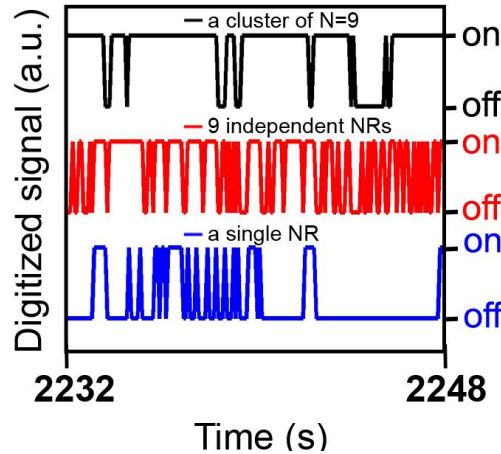


Figure 5.2 Digitized segment of the fluorescence time trace from a cluster of nine NRs (top), from $N = 9$ uncorrelated NRs (middle), and from a single NR (bottom).

Just from inspecting excerpts of the digitized time traces (Figure 5.2), it is evident that the clusters exhibit much longer on-times than a combined signal from the same number of separate NRs (summation of the traces from independent NRs, see Supplementary Information 5.5.3) measured from the same chip. The increased on-times are also clearly manifested in the shape of the on-time PDF that is stretched towards longer on-times (Figure 5.3a). The truncation time τ_c^{on} can be as much as two orders of magnitude greater for clusters than for the combined signal from the same number of isolated particles (Figure 5.3b).

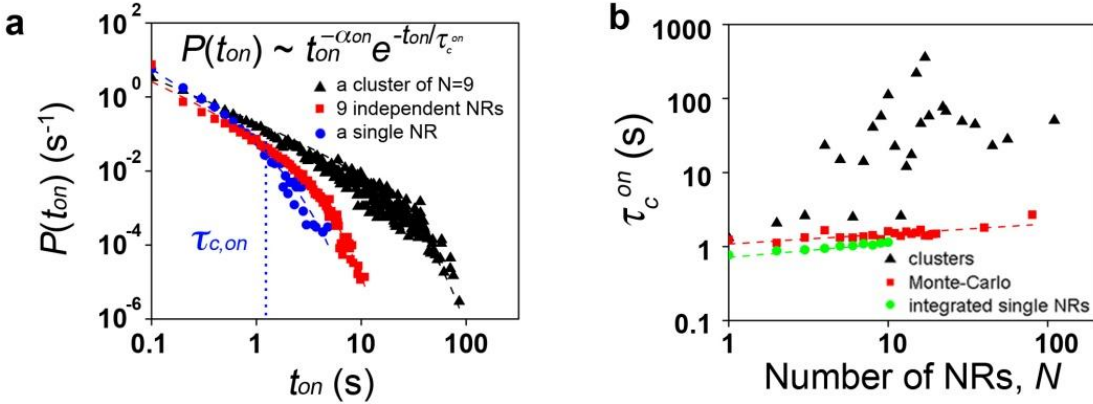


Figure 5.3 a) Probability density of on-times from the traces shown in Figure 5.2 for $N=9$. The effects of interactions are seen as a cutoff time $\tau_{\text{c},\text{on}}$ in the Lévy distribution of a cluster (black) compared to the corresponding $\tau_{\text{c},\text{on}}$ for integrated signals of nine independent particles (red) and for a single NR (blue). b) Scaling of $\tau_{\text{c},\text{on}}$ with the cluster size N (black triangles) compared with that of N isolated NRs located on the same chip (green squares) and with results from a Monte-Carlo simulation of N non-interacting particles (red squares).

We quantify the increased on-times by calculating the mean and maximum on-times, and by fitting the on-time probability densities to a truncated power law. Figure 5.4 shows the maximum and mean on-times for 120 clusters (open and solid black triangles), where each point gives the average obtained from all clusters with the same particle number, N . These results are compared to both the signal obtained by combining individual signals from N separate particles that were found on the same chip (Figure 5.4, open and solid green circles) and a Monte-Carlo simulation combining N independent trajectories following truncated power-law blinking dynamics (Figure 5.4, open and solid red squares). The combined experimental data were averaged over thirty random combinations of single NRs and the Monte-Carlo data were generated independently for each N . Individual signals from N separate NRs were combined either before or after the individual signals were digitized as described in Supplementary Information 5.5.4; both approaches, compared in Figure 5.13, yield the same conclusions.

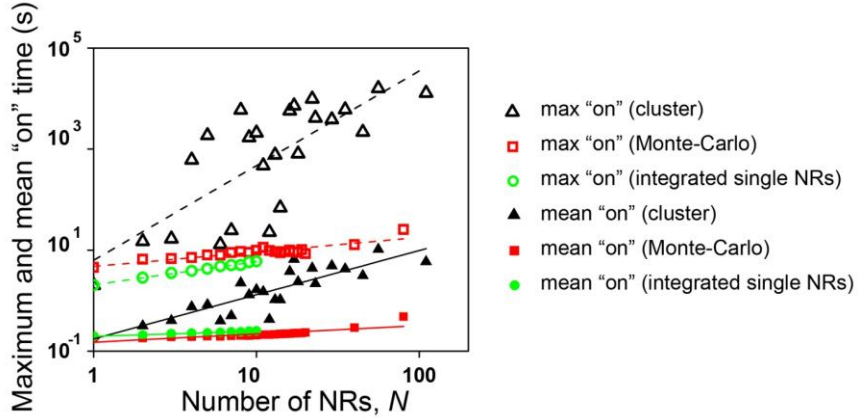


Figure 5.4 Scaling of mean and maximum on-times with the cluster size N (open and solid black triangles) compared with on-times obtained from integrating signals from N isolated NRs located on the same chip (open and solid green circles) and with results from a Monte-Carlo simulation of N non-interacting particles (open and solid red squares).

For clusters, we find that both maximum and mean on-times increase by a factor of N or more over the same number of independent NRs (both data and simulated). For example, the maximum on-time of ~ 10 s for $N = 10$ independent NRs increases to ~ 1000 s for clusters of ten NRs. Figure 5.4 displays the average over all measured clusters of a given N ; in addition, all clusters with $N > 6$ and more than 80% of clusters with $1 < N \leq 6$ exhibit enhanced on-times compared to both N measured individual NRs and Monte-Carlo simulations.

Similarly, the truncation time τ_c^{on} can be as much as two orders of magnitude greater for clusters than for the combined signal from the same number of isolated particles (Figure 5.3a). We use the fit to the truncated power law simply as a way to characterize the range of observed on-times; it is not clear that cluster fluorescence should be expected to display truncated power law statistics, and the variation in power law exponents between individual NRs would be expected to affect the distribution obtained from combining independent NRs.

The cluster data in Figure 5.3b and 5.4 show much more scatter than either the combined data from independent NRs or the Monte-Carlo simulation. One possible explanation for some of the scatter is that, for the combined independent NRs and the Monte-Carlo simulation, N is the number of emitting NRs, but for the clusters, N is the actual number of NRs in the cluster obtained from the TEM images, and may therefore be greater than the number of emitting NRs in each cluster, because a significant fraction (up to $\sim 50\text{-}70\%$) of NRs may be permanently dark. [Ebenstein 2002, Wang 2008, Querner 2008,] For the clusters, N therefore represents an upper bound on the number of emitting NRs. The enhancement of on-times may therefore be even more dramatic than Figure 5.3b and 5.4 suggest. Another likely source of scatter is the variation in distances between NRs in a cluster, which would be expected to affect the strength of any interaction. As shown in Figure 5.1d, in some clusters all NRs are closely packed, while in most, some are close-packed and others are more widely separated.

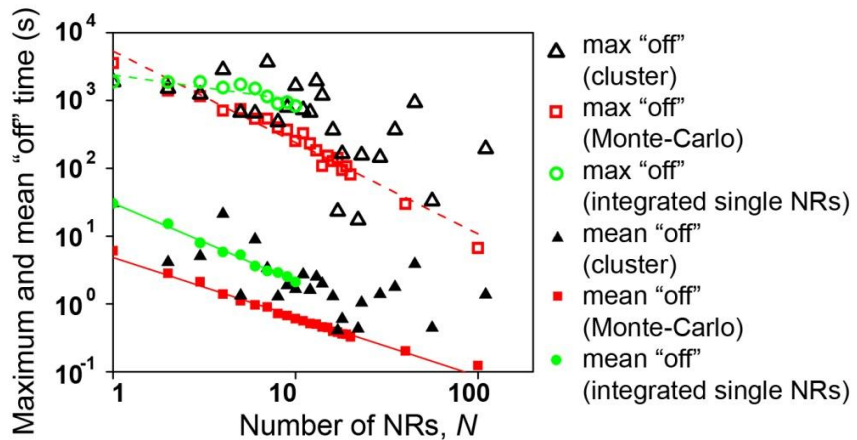


Figure 5.5 Scaling of mean and maximum off-times with the cluster size N (open and solid black triangles) compared with off-times obtained from integrating signals from N isolated NRs found on the same chip (open and solid green circles) and with results from a Monte-Carlo simulation of N non-interacting particles (open and solid red squares).

Although the distribution of on-times differs dramatically from clusters to combined independent NRs, the total time spent on (obtained by summing all on-times

from a given experiment) does not increase by more than one order of magnitude. This is shown in Figure 5.6a (compare green circles and black triangles). Furthermore, within our experimental resolution, we see no effect of interactions on the mean or maximum off-times (Figure 5.5). This indicates that cluster fluorescence trajectories are composed of fewer on-events that are on average longer, while trajectories combined from multiple independent particles are composed of a greater number of shorter on-events (Supplementary Information 5.5.5).

Figure 5.6b shows that the total integrated intensity, I_{int} , of clusters increases sublinearly with the number of NRs, although the decrease compared to the independent combined NRs is not dramatic. (The total integrated intensity is calculated according to

$$I_{int} = \sum_{i=1}^M I_i / M, \text{ with } I_i \text{ the background-subtracted intensity for the } i^{\text{th}} \text{ time interval of } 0.1$$

s from a particular time trace.) One possible explanation for the sublinearity is that the number of optically active NRs in the cluster is consistently less than N . This is plausible, because, as previously discussed, not all NRs in TEM images are necessarily emitting. [Ebenstein 2002] Another possibility is that interactions between the NRs in closest proximity significantly reduces simultaneous emission from multiple NRs within the cluster. Others have previously established that individual NCs are single-photon emitters. [Messin 2001, Michler 2000, Brokmann 2004] In the future, submicrosecond autocorrelation function measurements of cluster emission, to correlate particle number with the degree of photon antibunching, may clarify further under what circumstances multiple particles within clusters function as independent emitters.

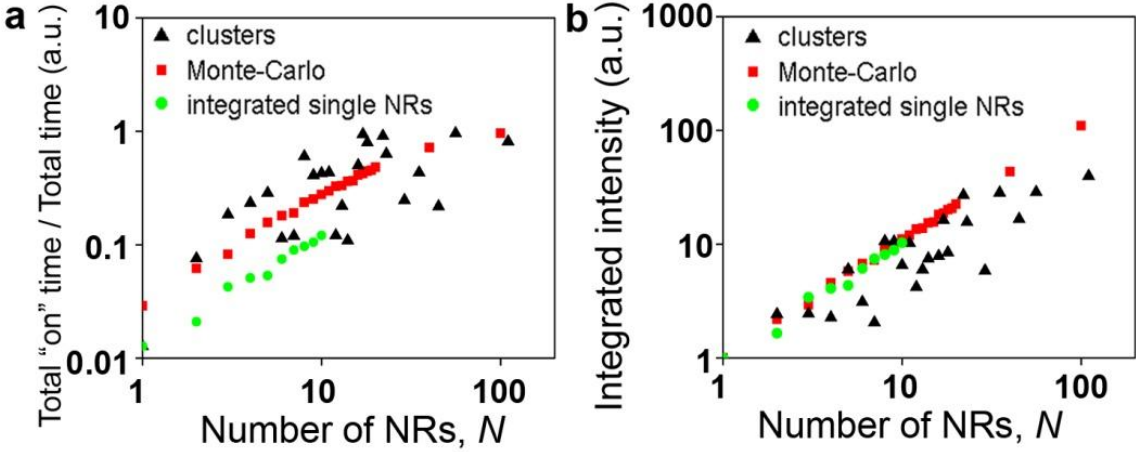


Figure 5.6 a) Scaling of the fraction of the total time spent in the on-states with N (black triangles) compared with data obtained from integrating signals from N isolated NRs found on the same chip (green circles), and with results from a Monte-Carlo simulation of N non-interacting particles (red squares). b) Scaling of the integrated intensity with N (black triangles) compared with data obtained from integrating signals from N isolated NRs found on the same chip (green circles) and with results from a Monte-Carlo simulation of N non-interacting particles (red squares).

We now consider the theoretical scaling of the mean and maximum on- and off-times with the cluster size N . To get an idea of how the mean and maximum on- and off-times should scale in the absence of interactions, first let us understand what would happen in the simplest case where each nanoparticle blinking is governed by Poissonian distributions of on- and off-times, supposing the ratio $r = \langle t_{off} \rangle / \langle t_{on} \rangle \gg 1$ (r approaches 150 from Figure 5.4 and Figure 5.5 for $N = 1$). For large r , the intensity trajectory is a sequence of bright spikes separated by long dark intervals; both mean and maximum duration off-intervals would be of the order $\langle t_{off} \rangle$. Adding N such uncorrelated signals will increase the rate of the spikes N -fold, thereby reducing both the mean and maximum off-times by a factor of N , while negligibly affecting the mean and maximum duration of the on-spikes, as long as $N < r$. (If $N \sim r$, the overlap of the on-spikes will become significant and both the mean and maximum values of the on-times will start increasing with N .)

This argument applies qualitatively to truncated power-law statistics as well, as long as the cutoffs for on- and off-distributions are much shorter than the observation time. Monte-Carlo simulations for summing either Poissonian or truncated Lévy uncorrelated distributions support these observations. Figure 5.4 (open and solid red squares) shows the Monte-Carlo simulations of the maximum and mean on-times for N independent particles with the same fluorescence statistics, assuming the same range of power-law exponents α_{on} , α_{off} , and truncation times (see Supplementary Information 5.5.4). The statistical parameters acquired from the Monte-Carlo simulated signal qualitatively agree with those acquired from the signal from a collection of non-interacting NRs. The quantitative discrepancies are attributed to the variability of the PDF parameters of the individual NRs, while the Monte-Carlo simulations are performed with identical $\tau_c^{on(off)}$ and $\alpha_{on(off)}$ for all NRs.

From Figure 5.5, we see that, in agreement with the above reasoning, both mean and maximum off-times for N non-interacting particles indeed decay approximately as $1/N$ (Figure 5.5). This property persists also for the clusters, at least within our experimental errors. For the on-times (Figure 5.4), the difference from the uncorrelated picture is profound: both mean and maximum on-times grow very rapidly with N even at $N \sim 1$, while the off/on ratio $r \sim 150$. In contrast, the same quantities for the non-interacting particles almost do not change with N . Quantitatively, the power laws for a cluster and for non-interacting particles differ approximately by a factor of $N^{1.6}$ for maximum on-times and by a factor of $\sim N^{0.7}$ for mean on-times. It is this significant scaling of the statistics of on-times with the cluster size that reveals the extensive

character of the observed effect. This scaling implies that the novel behaviour is indeed collective.

5.3.3 Autocorrelation functions and charging process

We also examine autocorrelation functions (ACFs) of fluorescence trajectories of individual NRs and clusters (Figure 5.7a). We define the autocorrelation function as

$$g_2(\tau) = \frac{\langle I(t) \cdot I(t + \tau) \rangle}{\langle I(t)^2 \rangle}, \quad \text{Eq 5.1}$$

where $I(t)$ is the fluorescence intensity at time t , and τ is the lag time. The ACFs shown in Fig. 4a are the average over the ACFs of clusters with the same particle number, N . At shorter lag times ($\tau < 100$ s), $g_2(\tau)$ decays fastest for individual NRs (black curve) and its decay slows down as N increases (colour). Figure 5.7b shows the average ACF values for all clusters studied as a function of N , at fixed lag times, $\tau_0 = 1$ s, 10 s, and 100 s; $g_2(\tau_0)$ increases with N for all τ_0 . This means that the fluorescence trajectory of a cluster correlates with itself more strongly in larger clusters. The bright state turns dark more slowly in clusters than in the case of independent particles and the on-times in clusters are extended. This is also consistent with our observation of the strong increase of on-times (Figure 5.4). Finally, we note that the ACF analysis of NC clusters reported in Ref. [Yu 2006] found that instead, the ACF decays faster for clusters than for individual NCs. The difference may be due to use of spherical NCs rather than NRs, combined with the different sample preparation method used to make clusters. As that work did not address differences in the blinking parameters, we cannot compare findings of the particle number dependence of on- and off-times.

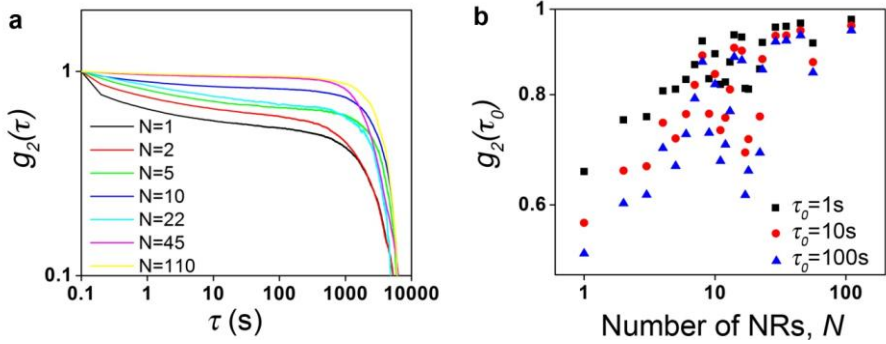


Figure 5.7 a) Autocorrelation functions of individual NRs (black curve) and NR clusters of $N = 2, 5, 10, 22, 45, 110$ (shown in colour). b) Scaling of the values of autocorrelation functions at $\tau_0 = 1$ s, 10 s, and 100 s with the cluster size N .

5.3.4 Physical models

To reconcile the dramatic enhancement of maximum and mean on-times with the unchanged off-time distribution for the cluster, and drawing on the Auger recombination model for blinking we propose two kinds of possible in-cluster charging processes, each one potentially capable of keeping at least one NR uncharged and, hence, bright: *direct charge tunneling* between closely located NRs, and *electric field-mediated charge redistribution* which can either be *static* (involving exciton rearrangement) or *dynamic* (involving coordinated trapping and detrapping). For the smallest possible cluster ($N = 2$), Fig. 5.8 shows a schematic diagram of each of these processes, compared with the charge states of two independent NRs. For two NRs, there are three possible charge state combinations: neutral-neutral, charged-neutral, and charged-charged (the latter one being dark). Here the charged state corresponds to an electron trapped in the NR shell or in the local environment, with the hole left on the NR rendering it dark. The charged-neutral state can become dark if an electron from the neutral NR also becomes trapped, causing it to switch off. In a cluster, this electron may instead recombine with the hole in the neighbouring dark NR, rendering the latter neutral (direct charge tunneling in Fig. 5.8).

Alternatively, when the electron from the neutral NR is trapped, the resulting electric field change may cause the previously dark NR to switch on without direct charge transfer between the NRs. This may happen either dynamically, by provoking recombination of the adjacent trapped electron with its dark NR core (i.e., coordinated trapping and detrapping, shown in Fig. 5.8), or statically, by the field change reducing the overall static field acting on the exciton in the dark NR (i.e., exciton rearrangement, shown in Fig. 5.8). Indeed, it has been shown experimentally [Rothenberg 2005] that a NR can be switched “off” or “on” by a static field which increases or decreases, respectively, the spatial electron-hole separation. Such a field in the dark NR may originate either from the residual crystal field in a NR [Rothenberg 2005] or due to charges in the environment. Estimates of the field strengths involved in the field-mediated processes are provided in the Supplementary Information 5.5.6.

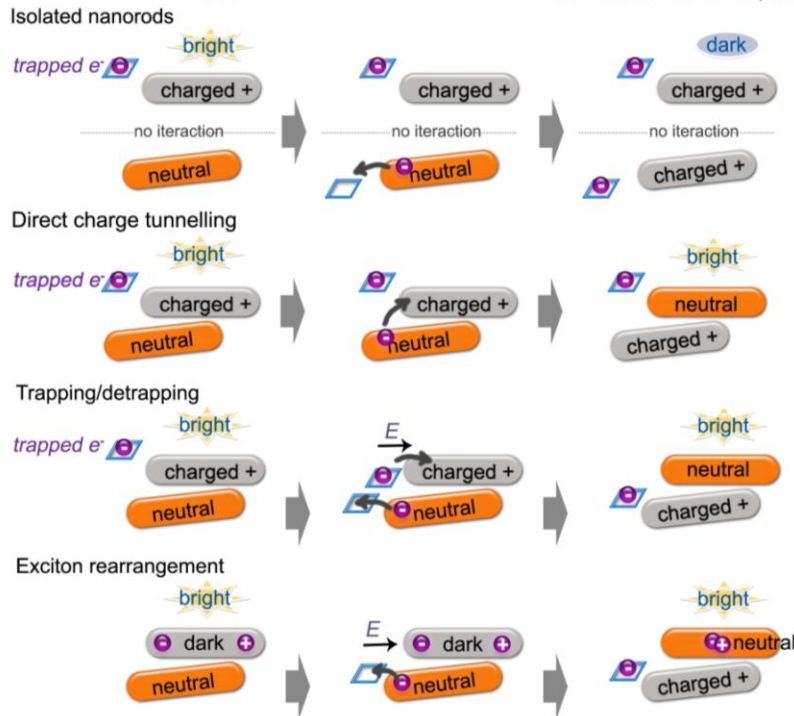


Figure 5.8 Proposed schematic diagrams of the charging process in a cluster of $N=2$ and in two isolated NRs.

Either of the suggested charge movements would facilitate combining the on-times of individual NRs in a continuous sequence, in a cluster of any size, as long as at least one NR remains bright. While the total time spent on should increase under either of these scenarios, the observed increase (Fig. 5.6a) of the fraction of time spent in the on state grows relatively slowly with N . This is expected near saturation, when this fraction approaches unity, resulting in the large clusters emitting most of the time. Notably, all of the suggested mechanisms would keep the distribution of off-times unchanged from what would be expected for independent NRs, in agreement with our observations. This is because an off-time for either the cluster or the combined independent NRs corresponds to a time during which there is no charge transfer into or out of any of the individual NRs.

Estimates of the distance ranges of these charging processes show that all are strongly sensitive to the separation between NRs, and thus the dominant interactions should occur between the closest NRs in clusters. Direct tunneling is only likely between close-packed NRs separated by 1-2 nm. For spherical core-shell nanocrystals, Kuno *et al* [Kuno 2001] estimate that the range of experimentally observable blinking rates (from 10 kHz to 0.01 Hz) could correspond to tunneling between the core and trap sites on the substrate 1-2 nm away from the surface of the nanocrystal shell. This suggests direct charge tunneling between close-packed NRs in our clusters is plausible. Furthermore, tunneling could involve an intermediate state on the silicon nitride substrate between the NRs, as long as its lifetime is sufficiently short that the complete charge transfer process occurs in less than our temporal resolution of 0.1 s. This could potentially extend the distance range somewhat. The dynamical effect of coordinated trapping and detrapping

depends on the details of the trapping potential. Our estimates (Supplementary Information 5.5.6) suggest that it is also most effective between NRs separated by just a few nm, because this charge rearrangement produces an effective dipole field that decays over relatively short distances. Finally, static exciton rearrangement may act on distances up to 8-10 nm (see 5.5.6) for NRs suitably aligned with the field of the trapped charge, so it may act on somewhat longer distances than the other mechanisms.

All of the above “interaction” mechanisms based on charge processes are consistent with the geometry of our clusters. Analysis of TEM images of the clusters studied shows that ~ 85% of the clusters in our study include at least two NRs separated by 2 nm or less from edge to edge, and that larger clusters have greater percentages of NRs next to each other. However, almost none of the $N > 2$ clusters are fully close-packed; most clusters have between 50% and 80% of NRs with at least one neighbour within 2 nm or less. (Details are provided in Supplementary Information 5.5.7).

Overall, the complexity of the observed statistics most likely reflects the presence of more than one mechanism at work, and possibly all of them. Indeed, although many of the proposed models for blinking are based on charging processes, an alternative class of models based on fluctuating nonradiative rates [Frantsuzov 2005, 2009, Hammer 2006, Park 2007] has also been proposed. In these models, blinking is associated with opening and closing certain nonradiative exciton recombination pathways involving localized surface states. With such a mechanism, resonant energy transfer, resulting in exciton transfer between NRs in a cluster, would be likely to affect the blinking statistics significantly, potentially by transferring excitations from dark NRs to bright ones, although it is not immediately clear to us how energy transfer within such a mechanism

could produce our observed sequencing of on-states while leaving the off-statistics unchanged. Regardless of the still debated blinking framework, the apparent interaction effect observed here should introduce constraints and couplings between the single-NR parameters of these and other possible models of blinking, and could help either validate them or rule them out. Such investigation is beyond the scope of this work.

To further test the mechanism behind the observed enhancement, we analyzed the mean and maximum on-times *vs.* mean inter-particle separations (the simplest case of $N = 2$ is shown in Supplementary Information 5.5.8). We find that the on-times are too scattered to observe any clear trend with inter-particle separations. This scatter can result from a large variation in blinking parameters of the individual NRs that comprise the clusters so that no clear trends are observable when measuring ensembles of clusters with fixed N . Another potentially important factor is the uncertainty in the actual number of emitting NRs within particular clusters. For example, a pair of NRs observed in TEM imaging may include only a single emitting NR.

To eliminate the confounding effects of ensemble averaging, we have also attempted to guide the NR assembly into ordered clusters by patterning surface features on silicon nitride substrates and by surface modifications, but subsequent TEM imaging revealed that the resulting clusters, though spatially more localized, still contained a large degree of disorder. In order to unequivocally explain the underlying interaction mechanisms, small NR clusters with well-controlled assembly patterns and inter-particle separations are needed. This is a challenging goal for future experiments since reproducible ordered assembly of CdSe nanoparticles is still a difficult task.

5.4 Conclusion

In conclusion, we observed a collective effect in the fluorescence of disordered nanoparticle clusters resulting in dramatically longer bright periods than measured and simulated on collections of independent particles. While clusters do not emit more intensely, the synergy is manifested in prolonged emission periods. One possible explanation for our observations is that particles may alternate with each other in bright and dark states to extend the overall emission period. The long on-times observed here may also explain earlier observations on very large NR ensembles ($N > 10,000$) [Querner 2008] where the onset of the power-law decay in ensemble fluorescence occurred much later than predicted by a statistical model based on non-interacting single-particle dynamics. [Chung 2006, Querner 2008] Finally, our study suggests that small NR clusters may be usable as nanoscale light sources with very long emission times. For example, maximum emission times can be extended from 10 to 1000 s for clusters with ten NRs. CdSe nanorods have many promising applications as nanoscale emitters, both as fluorescent labels in applications that do not require ultra-small nanoprobes, and as single photon sources. The dramatic increase of up to two orders of magnitude in emission times reported here demonstrates that inter-particle interactions in clusters can favourably modify blinking dynamics.

5.5 Supplementary Information

5.5.1 Maximum and mean on-time results hold qualitatively for a range of thresholds.

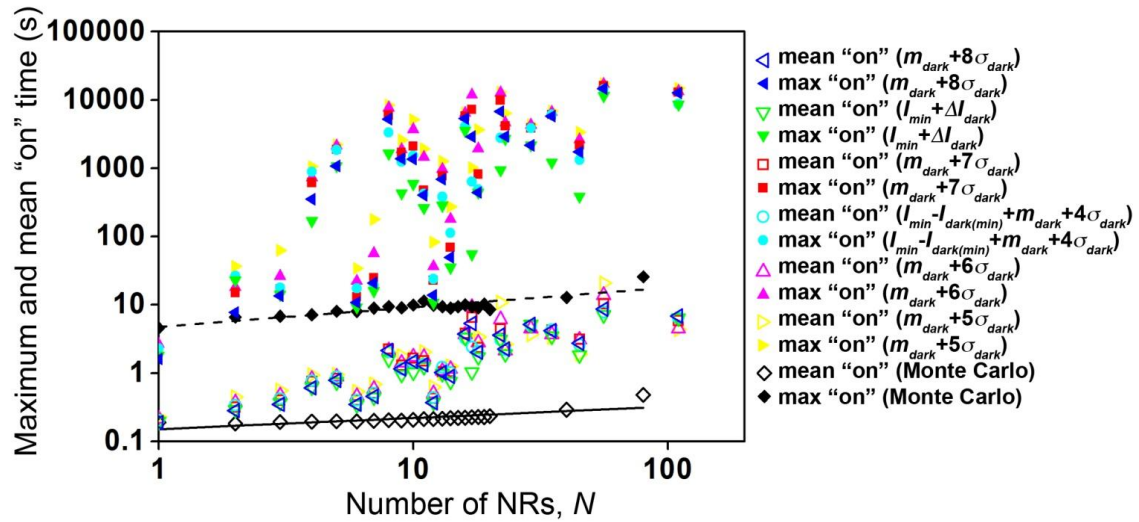


Figure 5.9 Scaling of mean and maximum on-times with the cluster size N with a range of thresholds defined as $m_{dark} + 8\sigma_{dark}$, $I_{min} + \Delta I_{dark}$, $m_{dark} + 7\sigma_{dark}$, $I_{min} - I_{dark(min)} + m_{dark} + 4\sigma_{dark}$, $m_{dark} + 6\sigma_{dark}$, and $m_{dark} + 5\sigma_{dark}$ (see **Section 3.5.3** for determination of thresholds).

5.5.2 Comparison of independent fluorescence measurements on two different chips

Several months apart, we made independent measurements under the same experimental conditions on samples prepared by spin-casting solutions of the same NRs on two identically prepared silicon nitride chips (Figure 5.10). Chip 2 was prepared with a higher concentration NR solution in order to produce more clusters. Figure 5.11 shows that the data from these independent measurements match very well.

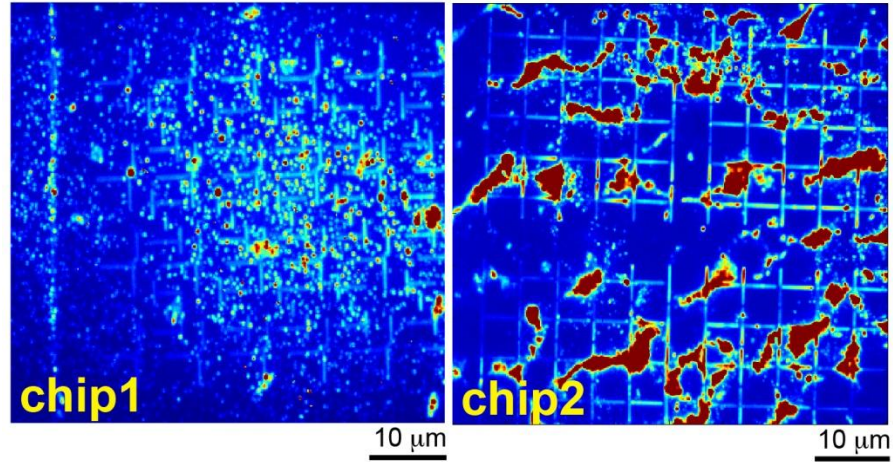


Figure 5.10 Fluorescence micrographs of two silicon nitride chips used in this study. The larger red areas correspond to extended regions in which individual clusters were not optically resolvable. We only analyzed data from clusters optically resolvable from their neighbours (see Section 3.5.2).

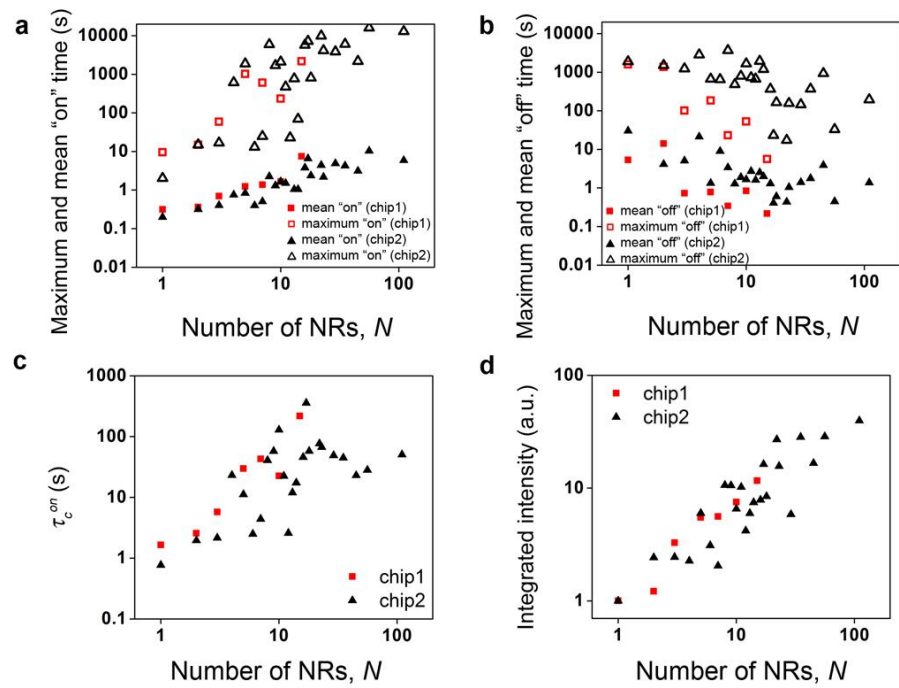


Figure 5.11 **a**, Scaling of mean and maximum on-times with the cluster size N from chip1 (open and solid red squares) compared with on-times obtained from chip2 (open and solid black triangles). **b**, Scaling of mean and maximum off-times with the cluster size N from chip1 (open and solid red squares) compared with off-times obtained from chip2 (open and solid black triangles). **c**, Scaling of τ_c^{on} with the cluster size N measured on chip1 (red squares) compared with data obtained from chip2 (black triangles). **d**, Scaling of the integrated intensity with the cluster size N measured on chip1 (red squares) compared with data obtained from chip2 (black triangles).

5.5.3 Overlapping effect of summing up digitized traces of nine independent NRs

The digitized trace of nine independent NRs in Figure 5.2 (the middle trace) was the digitized summation of the digitized traces of nine independent NRs in the experiment. Figure 5.12 shows the digitized traces of the additional 8 independent rods not showing in Figure 5.2 and the overlapping effect when these nine independent traces (blue and pink traces) sum up to produce the middle trace (red) in Figure 5.2. Figure 5.2 shows the excerpt in the dashed box.

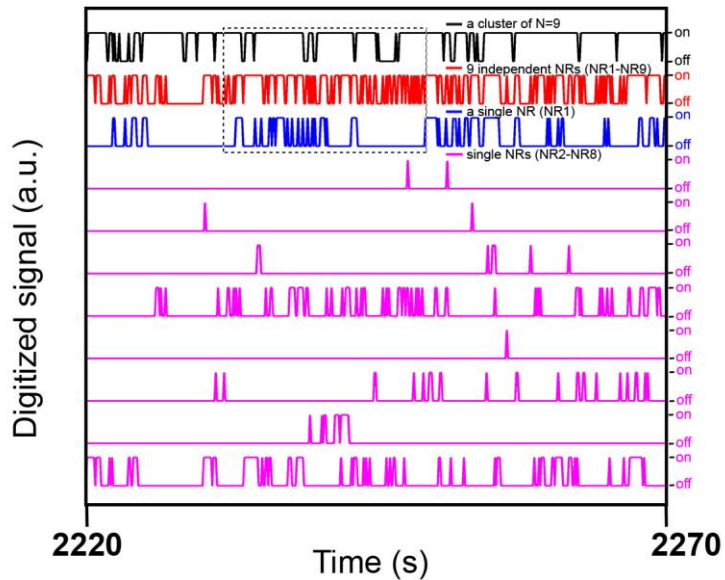


Figure 5.12 Overlapping effect of summing up digitized traces of nine independent NRs (blue and pink traces) to produce the red trace in **Figure 5.2**. **Figure 5.2** shows the excerpt in the dashed box.

5.5.4 Integration of fluorescence signals from independent NRs and Monte-Carlo simulation

We compare the mean and maximum on-times of the integrated N independent single NRs to those of clusters with N NRs on the same chip. To compute the integrated data, two distinct approaches were used: In the first approach (“digitizing before summing”), we add trajectories digitized to be 0 or 1 by a threshold (Section 3.5.3) of N single NRs

selected randomly from 14 single NRs found on the chip. We then determine the "on" events by setting a threshold of 0.5. In order to maximize the sampling size, we repeat a random selection and data analysis 30 times for $N = 1\text{-}10$ and take the average. In the second approach, ("summing before digitizing,") we sum up the raw trajectories prior to background subtraction and digitization. We subsequently subtract the appropriate polynomial fit to the background and a threshold determined from the integrated background signal.

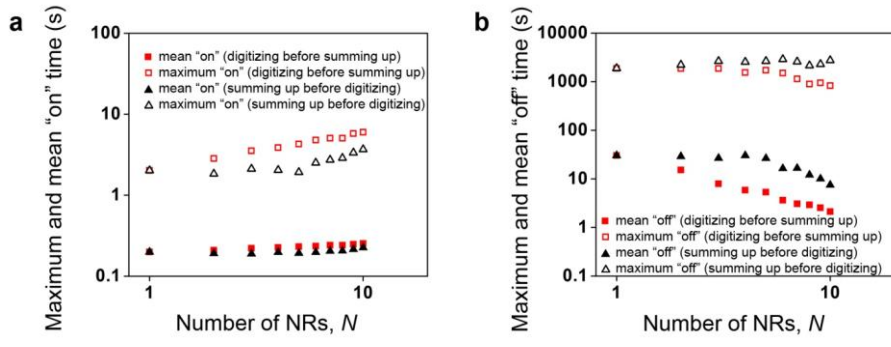


Figure 5.13 Scaling of **a.** mean and maximum on-times and **b.** mean and maximum off-times with the cluster size N using two methods of integrating independent single NRs, thresholding and digitizing before summing up (red squares) and summing up before thresholding and digitizing (black triangles).

Next, we compare the maximum and mean on- and off-times using the two methods. Figure 5.13a shows that the mean on-times of the two methods agree well, while the maximum on-times are smaller using the second method (black open triangles). In Figure 5.13b, both mean and maximum off-times using the second method (black triangles) are larger than those results from the first method (red squares). The reason could be that the threshold in the second method was determined the same way as described in Section 3.5.3, and it was elevated up too high due to the integration of background signals so that we lost some signals which should be considered "on", which shortened the on-times and extended the off-times. The on-times from both methods are

substantially lower than those of clusters data (Figure 5.4 shows on-times from the first method) and both support the conclusion in the main paper.

We do the Monte-Carlo simulation for a single NR by generating "on" and "off" events using the inverse function of Eq. 1 in the main article for on- and off-times, respectively. We set $\tau_c^{on} = 1$ s, $\tau_c^{off} = 1000$ s, and $\alpha_{on} = \alpha_{off} = 1.5$. For each N , we generate the single trajectories independently, integrate them and then digitize the result using a threshold of 0.5.

5.5.5 Total number of "on" events

Figure 5.14 shows the number of "on" events as a function of the cluster size N . This number on the y-axis was normalized to the data of $N = 1$ to account for the different lengths of the movies in the Monte-Carlo simulation compared to the cluster data. It shows that the total number of "on" events decreases in clusters of N NRs compared to the collection of independent NRs, *i.e.*, fluorescence time traces of clusters consist of a relatively smaller number of on-events that are on average longer, as described in the main article.

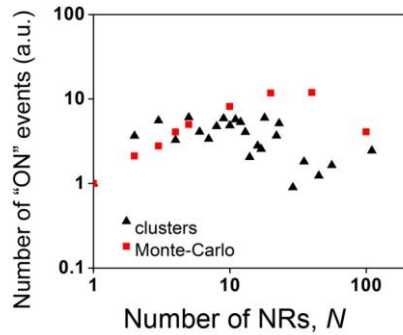


Figure 5.14 The total number of "on" events vs. the cluster size N (black triangles) compared with data obtained from a Monte-Carlo simulation of N non-interacting particles (red squares).

5.5.6 Estimates of electric field-induced exciton rearrangement and field-driven coordinated trapping/detrapping

Field-induced exciton rearrangement: A charge moving a distance a from a NR core to a neighboring trap would cause a change $E = \text{const} \cdot ea/\varepsilon r^3$ in the electric field at a distance $r >> a$ equivalent to a field from a dipole with the dipole moment ea . Even in the case of $r \sim a$, which applies to NRs very close to each other, this formula would still yield a correct order-of-magnitude estimate. Here ε is the effective dielectric constant of the environment, $\varepsilon = (\varepsilon_{\text{substr}} + 1)/2 \approx 4$, where $\varepsilon_{\text{substr}} = 7.5$ for SiN. The prefactor ‘const’ in the expression for the magnitude of E depends on the angle θ between the direction \mathbf{a} of the hop and the given direction \mathbf{r} , as $(1+3\cos^2\theta)^{1/2}$, which varies between 1 and 2, as well as on the further details of the dielectric environment (the depolarization factors, *etc*), see e.g. Ref. [Kovalev 1995].

As a result, using $e^2/(1 \text{ nm}) = 1.44 \text{ eV}$, we obtain for the electric field $E \sim (1\dots 2) \cdot 1.44 \cdot (a/r^3)/\varepsilon \text{ V/nm}$, where a and r are in nm. Note that $1 \text{ V/nm} = 10 \text{ MV/cm}$; with the hop distance $a = 4 \text{ nm}$ compatible with the wave function size within a NR, and $r = 8 \text{ nm}$ the distance to a neighbouring NR, find $E \sim 11\dots 22 \text{ mV/nm} = 110\dots 220 \text{ kV/cm}$ applied (unscreened) field depending on the direction, which, according to the measurements of Rothenberg *et al*, [Rothenberg 2005] could cause switching of a neighbouring NR at a distance r .

Field-driven coordinated trapping/detrapping: Now let us consider a *dynamic* effect of a sudden change in the electric field on an electron trapped in a vicinity of a given NR, due to switching off of a neighboring NR caused by the hop of its electron onto the

corresponding nearby trap. This sudden field change can potentially cause the release (a “shake-up”) of the trapped electron back on a given NR, thereby switching it on.

While any precise calculation would require detailed information about the character of a trapping potential, we may still make some order-of-magnitude estimates. First, assume a trapped electron in a ground state of an approximately harmonic oscillator potential with the oscillator frequency (potential curvature) ω_0 . Under a sudden change of an electric field E at the position of an oscillator, the probability P_k to get excited to the k^{th} oscillator level is given by the Poissonian distribution $P_k = (\lambda^k/k!) \cdot \exp(-\lambda)$, where $\lambda = (eE)^2/(2m\hbar\omega_0^3)$, see Ref. [Landau 2003]. As a realistic trap potential likely has only one or a few bound states, one can qualitatively assume that the shake-up occurs with a notable probability if the corresponding oscillator shake-up parameter $\lambda \sim 1$ (*i.e.* not small). For an estimate, we would also assume that the trap binding energy is of the order of oscillator energy spacing, $E_{\text{trap}} \sim \hbar\omega_0$, consistent with the above assumption of only a few eigenlevels in a trap. From the condition $\lambda \sim 1$ we obtain the maximal depth E_{trap} of the trap that could be depleted by the shake-up over a distance r : $E_{\text{trap}} \sim (eE(r))^{2/3}(\hbar^2/2m)^{1/3}$. Since $\hbar^2/(2m) = 38 \text{ meV}\cdot\text{nm}^2$ [m is the electron mass; the effective mass may be notably smaller depending on where the trap is located which would increase E_{trap}], and $eE \sim 10 \text{ meV/nm}$ for r and a as above (depending on the effective dielectric constant and orientation), obtain $E_{\text{trap}} \sim 10\text{-}100 \text{ meV}$, which is compatible with energies of shallow traps. When $r \sim 1 \text{ nm}$ rather than 10 nm , *i.e.* NRs are very close, E_{trap} can exceed 0.1 eV , covering a wider portion of the trap energies.

Overall, we expect the dynamic field-driven effect acts on a similar distance scale as direct charge tunneling ($\sim 2 \text{ nm}$). The short-range character of both effects is

fundamentally due to the fact that both the dipole field (in the first case) and its square entering the shake-up matrix element (in the second case), decrease faster than $1/r^d$, thereby being effectively short-ranged in the $d=2$ -dimensional geometry of our clusters. Our estimates indicate that static field-driven distortion may be somewhat longer ranged (up to ~ 8 nm).

5.5.7 Fraction of close-packed NRs within clusters

We analyzed the TEM images of the clusters to determine the fraction of close-packed NRs in each. Fig. 5.15 shows the fraction of close-packed NRs *vs* the number of NRs in the cluster for 74 clusters. There is a broad distribution of the fraction of close-packed NRs; nearly all clusters have at least a few close-packed NRs (60 out of 74 clusters). Some of the data points are overlapping, e.g. two $N=9$ clusters each have the same fraction (0.56) close-packed. Fig. 5.16 shows the histogram of the fraction of close-packed NRs of the 74 clusters. Most clusters have between 50% and 80% of NRs close-packed with at least one neighbor. However, almost none of the clusters for $N > 2$ are fully close-packed. We also show the fraction of close-packed NRs in Table 5.1 for reference.

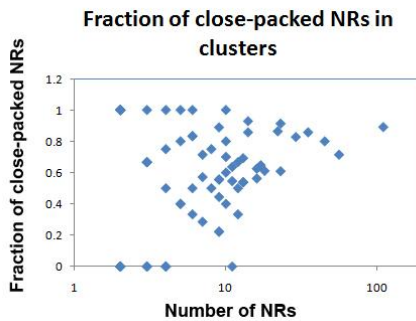


Figure 5.15 Fraction of close-packed NRs *vs* number of NRs of 74 clusters. Some of the data points are overlapping , e.g. there are two $N=9$ clusters which are having a fraction of 0.56.

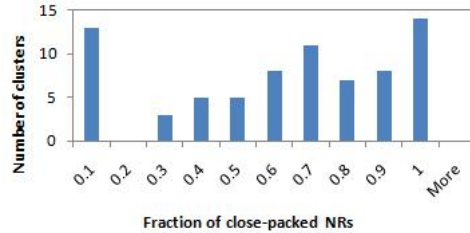


Figure 5.16 Histogram of the fraction of close-packed NRs in clusters.

Table 5.1 Fraction of close-packed NRs.

Number of NRs	2	2	2	2	2	2	2	2	2	2	2	2	2	3	3	3
Fraction of close-packed NRs	1	0	1	0	1	1	0	0	1	0	0	1	1	0.67	1	0
Number of NRs	3	3	3	3	4	4	4	4	4	5	5	5	5	6	6	6
Fraction of close-packed NRs	0.67	0	0	0.67	0.5	0	0.75	1	0	0	1	0.8	0.4	0.4	0.5	0.83
Number of NRs	6	6	6	7	7	7	8	8	9	9	9	9	9	9	10	10
Fraction of close-packed NRs	1	0.83	0.33	0.71	0.57	0.29	0.5	0.75	0.22	0.44	0.56	0.22	0.56	0.89	0.7	0.6
Number of NRs	10	10	10	11	11	11	12	12	12	13	13	13	14	14	16	16
Fraction of close-packed NRs	0.8	0.4	1	0	0.55	0.64	0.5	0.33	0.67	0.54	0.54	0.69	0.86	0.93	0.56	0.63
Number of NRs	17	18	22	23	23	29	35	45	56	110						
Fraction of close-packed NRs	0.65	0.61	0.86	0.91	0.61	0.83	0.86	0.8	0.71	0.89						

5.5.8 “On” time vs. particle separation for clusters with $N=2$

To further test the mechanism behind the observed enhancement, we analyzed the on-times vs. mean inter-particle separations (the simplest case of $N = 2$ is shown in Figure 5.17). Unfortunately, the on-times are too scattered to observe any clear trend with inter-particle separations. This scatter can result from a large variation in blinking parameters of single NRs that comprise the clusters so that no clear trends are observable when measuring ensembles of clusters with fixed N .

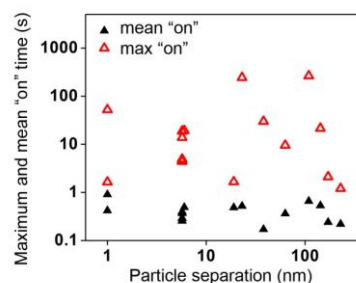


Figure 5.17 Mean and maximum on-time vs. inter-particle separation of cluster with $N = 2$.

Bibliography

- [Bates 2000] Bates, M. A. & Frenkel, D. *J. Chem. Phys.* **112**, 10034 (2000)
- [Beadie 1995] Beadie, G., Sauvain, E., Gomes, A. S. L. & Lawandy, N. M. *Phys. Rev. B* **51**, 2180 (1995)
- [Brokmann 2003] Brokmann, X., Hermier, J. P., Messin, G., Desbiolles, P., Bouchaud, J. P. & Dahan, M. *Phys. Rev. Lett.* **90**, 120601 (2003)
- [Brokmann 2004] Brokmann, X.; Giacobino, E., Dahan, M. & Hermier, J. P. *Appl. Phys. Lett.* **85**, 712 (2004)
- [Bruchez 1998] Bruchez, M., Moronne, M., Gin, P., Weiss, S. & Alivisatos, A. P. *Science* **281**, 2013 (1998)
- [Bullen 2006] Bullen, C. & Mulvaney, P. *Langmuir* **22**, 3007 (2006)
- [Chan 2004] Chan, Y., Caruge, J. M., Snee, P. T. & Bawendi, M. G. *Appl. Phys. Lett.* **85**, 2460 (2004)
- [Chen 2008] Chen, Y., Vela, J., Htoon, H., Casson, J. L., Werder, D. J., Bussian, D. A., Klimov, V. I. & Hollingsworth, J. A. *J. Am. Chem. Soc.* **130**, 5026 (2008)
- [Chen 2001] Chen, X., Nazzal, A., Goorskey, D., Xiao, M., Peng, Z. A. & Peng, X. *Phys. Rev. B* **64**, 245304 (2001)
- [Chung 2004] Chung, I. H. & Bawendi, M. G. *Phys. Rev. B* **70**, 165304 (2004)
- [Chung 2006] Chung, I., Witkoskie, J. B., Cao, J. S. & Bawendi, M. G. *Phys. Rev. E* **73**, 011106 (2006)
- [Chung 2007] Chung, I., Witkoskie, J. B., Zimmer, J. P., Cao, J. & Bawendi, M. G. *Phys. Rev. B* **75**, 045311 (2007)

- [Cichos 2007] Cichos, F., von Borczyskowski, C. & Orrit, M. *Curr. Opin. Coll. Int. Sci.* **12**, 272 (2007)
- [Crooker 2002] Crooker, S. A., Hollingsworth, J. A., Tretiak, S. & Klimov, V. I. *Phys. Rev. Lett.* **89**, 186802 (2002)
- [Crouch 2010] Crouch, C. H., Sauter, O., Wu, X., Purcell, R., Querner, C., Drndic, M. & Pelton, M. *Nano Lett.* **10**, 1692 (2010)
- [Dabbousi 1997] Dabbousi, B. O., Viejo, J. R., Mikulec, F. V., Heine, J. R., Mattoussi, H., Ober, R., Jensen, K. F. & Bawendi, M. G. *J. Phys. Chem. B* **101**, 9463 (1997)
- [Dubertret 2002] Dubertret, B., Skourides, P., Norris, D. J., Noireaux, V., Brivanlou, A. H. & Libchaber, A. *Science* **298**, 1759 (2002)
- [Ebenstein 2002] Ebenstein, Y., Mokari, T. & Banin, U. *Appl. Phys. Lett.* **80**, 4033 (2002)
- [Efros 1997] Efros, A. L. & Rosen, M. *Phys. Rev. Lett.* **78**, 1110 (1997)
- [Fischbein 2006] Fischbein, M.D. & Drndic, M. *Appl Phys. Lett.* **88**, 063116 (2006)
- [Frantsuzov 2005] Frantsuzov, P. A. & Marcus, R. A. *Phys. Rev. B* **72**, 155321 (2005)
- [Frantsuzov 2008] Frantsuzov, P., Kuno, M., Janko, B & Marcus, R. A. *Nature Physics* **4**, 519 (2008)
- [Frantsuzov 2009] Frantsuzov, P., Volka'n-Kacso', S., & Janko, B. *Phys. Rev. Lett.* **103**, 207402 (2009)
- [Garcia-Santamaria 2009] Garcia-Santamaria, F., Chen, Y., Vela, J., Schaller, R. D., Hollingsworth, J. A. & Klimov, V. I. *Nano Lett.* **9**, 3482 (2009)
- [Glennon 2007] Glennon, J. J., Tang, R., Buhro, W. E. & Loomis, R. A. *Nano Lett.* **7**, 3290 (2007)

- [Glennon 2008] Glennon, J. J., Buhro, W. E. & Loomis, R. A *J. Phys. Chem. C* **112**, 4813 (2008)
- [Hammer 2006] Hammer, N. I., Early, K. T., Sill, K., Odoi, M. Y., Emrick, T. & Barnes, M. D. *J. Phys. Chem. B* **110**, 14167 (2006)
- [He 2007] He, J., Zhang, Q., Gupta, S., Emrick, T., Russell, T. P. & Thiyagarajan, P. *Small* **3**, 1214 (2007)
- [Hess 2001] Hess, B.C., Okhrimenko, I. G., Davis, R. C., Stevens, B. C., Schulzke, Q. A., Wright, K. C., Bass, C. D., Evans, C. D. & Summers, S. L. *Phys. Rev. Lett.* **86**, 3132 (2001)
- [Hines 1996] Hines, M. A. & Guyot-Sionnest, P. *J. Phys. Chem.* **100**, 468 (1996)
- [Hohng 2004] Hohng, S. & Ha, T. *J. Am. Chem. Soc.* **126**, 1324 (2004)
- [Hu 2001] Hu, J.T., Li, L.S., Yang, W.D., Manna, L., Wang, L.W. & Alivisatos, A.P. *Science* **92**, 2060 (2001)
- [Huynh 2002] Huynh, W. U., Dittmer, J. J. & Alivisatos, A. P. *Science* **295**, 2425 (2002)
- [Issac 2005] Issac, A., von Borczyskowski, C. & Cichos, F. *Phys. Rev. B* **71**, 161302 (2005)
- [Kimura 2004] Kimura, J., Uematsu, T., Maenosono, S. & Yamaguchi, Y. *J. Phys. Chem. B* **108**, 13258 (2004)
- [Klimov 2000] Klimov, V. *J. Phys. Chem. B* **104**, 6112 (2000)
- [Koberling 2001] Koberling, F., Mews, A. & Basche, T. *Adv. Mater.* **13**, 672 (2001)
- [Koberling 2002] Koberling, F., Mews, A., Philipp, G., Kolb, U., Potapova, I., Burghard, M. & Basche, T. *Appl. Phys. Lett.* **81**, 1116 (2002)

- [Kobitski 2004] Kobitski, A. Y., Heyes, C. D. & Nienhaus, G. U. *Appl. Surf. Sci.* **234**, 86 (2004)
- [Kovalev 1995] Kovalev, D., Ben Chorin, M., Diener, J., Koch, F., Efros, A. L., Rosen, M., Gippius, N. A. & Tikhodeev, S. G. *Appl. Phys. Lett.* **67**, 1585 (1995)
- [Krauss 1999] Krauss, T. D. & Brus, L. E. *Phys. Rev. Lett.* **83**, 4840 (1999)
- [Krishnan 2004] Krishnan, R., Hahn, M. A., Yu, Z. H., Silcox, J., Fauchet, P. M. & Krauss, T. D. *Phys. Rev. Lett.* **92**, 216803 (2004)
- [Kuno 1997] Kuno, M., Lee, J. K., Dabbousi, B. O., Mikulec, F. V. & Bawendi, M. G. *J. Chem. Phys.* **106**, 9869 (1997)
- [Kuno 2000] Kuno, M., Fromm, D. P., Hamann, H. F., Gallagher, A. & Nesbitt, D. J. *J. Chem. Phys.* **112**, 3117 (2000)
- [Kuno 2001] Kuno, M., Fromm, D. P., Hamann, H. F., Gallagher, A. & Nesbitt, D. J. *J. Chem. Phys.* **115**, 1028 (2001); Kuno, M., Fromm, D. P., Gallagher, A., Nesbitt, D. J., Micic, O. I. & Nozik, A. J. *Nano Lett.* **1**, 557 (2001)
- [Landau 2003] L. D. Landau & E. M. Lifshitz, Quantum Mechanics (Non-Relativistic Theory), Third Edition: Volume 3, Sec. 41, Butterworth-Heinemann, Oxford (2003)
- [Le Thomas 2005] Le Thomas, N., Herz, E., Schops, O., Woggon, U. & Artemyev, M. V. *Phys. Rev. Lett.* **94**, 016803 (2005)
- [Leatherdale 2002] Leatherdale, C. A., Woo, W. K., Mikulec, F. V. & Bawendi, M. G. *J. Phys. Chem. B* **106**, 7619 (2002)
- [Lee 2009] Lee, J. D. & Maenosono, S. *Phys. Rev. B* **80**, 205327 (2009)
- [Li 2007] Li, C., Kattawar, G. W., You, Y., Zhai, P. & Ying, P. *J. Quant. Spectrosc. Radiat. Transfer*, **106**, 257 (2007)

- [Mahler 2008] Mahler, B., Spinicelli, P., Buil, S., Quelin, X., Hermier, J. P. & Dubertret, B. *Nature Mater.* **7**, 659 (2008)
- [Manna 2000] Manna, L., Scher, E. C. & Alivisatos, A. P. *J. Am. Chem. Soc.* **122**, 12700 (2000)
- [Messin 2001] Messin, G., Hermier, J. P., Giacobino, E., Desbiolles, P. & Dahan, M. *Optics Lett.* **26**, 1891 (2001)
- [Michler 2000] Michler, P., Imamoğlu, A., Mason, M. D., Carson, P. J., Strouse, G. F., & Buratto, S. K. *Nature* **406**, 968 (2000)
- [Millo 2004] Millo, O., Katz, D., Steiner, D., Rothenberg, E., Mokari, T., Kazes, M. & Banin, U. *Nanotechnology* **15**, R1 (2004)
- [Moerner 2003] Moerner, W. E. & Fromm, D. P. *Rev. Sci. Instrum.* **74**, 3597 (2003)
- [Muller 2004] Muller, F., Gotzinger, S., Gaponik, N., Weller, H., Mlynek, J. & Benson, O. *J. Phys. Chem. B* **108**, 14527 (2004)
- [Müller 2004] Müller, J., Lupton, J. M., Rogach, A. L., Feldmann, J., Talapin, D. V. & Weller, H. *Appl. Phys. Lett.* **85**, 381 (2004)
- [Müller 2005a] Müller, J., Lupton, J. M., Lagoudakis, P. G., Schindler, F., Koeppe, R., Rogach, A. L., Feldmann, J., Talapin, D. V. & Weller, H. *Nano Lett.* **5**, 2044 (2005)
- [Müller 2005b] Müller, J., Lupton, J. M., Rogach, A. L., Feldmann, J., Talapin, D. V. & Weller, H. *Phys. Rev. B* **72**, 205339 (2005)
- [Murray 1993] Murray, C. B., Norris, D. J. & Bawendi, M. G. *J. Am. Chem. Soc.* **115**, 8706 (1993)
- [Nirmal 1996] Nirmal, M., Dabbousi, B. O., Bawendi, M. G., Macklin, J. J., Trautman, J. K., Harris, T. D. & Brus, L. E. *Nature* **383**, 802 (1996)

- [Novikov 2005] Novikov, D. S., Drndic, M., Levitov, L. S., Kastner, M. A., Jarosz, M. V. & Bawendi, M. G. *Phys. Rev. B* **72**, 075309, (2005)
- [Park 2007] Park, S. J., Link, S., Miller, W. L., Gesquiere, A. & Barbara, P. F. *Chem. Phys.* **341**, 169-174, (2007)
- [Peng 1997] Peng, X. G., Schlamp, M. C., Kadavanich, A. V. & Alivisatos, A. P. *J. Am. Chem. Soc.* **119**, 7019 (1997)
- [Peng 2001] Peng, Z. A. & Peng, X. G. *J. Am. Chem. Soc.* **123**, 1389 (2001)
- [Peng 2002] Peng, Z. A. & Peng, X. G. *J. Am. Chem. Soc.* **124**, 3343 (2002)
- [Peterson 2009] Peterson, J. J. & Nesbitt, D. J. *Nano Lett.* **9**, 338 (2009)
- [Pons 2006] Pons, T., Medintz, I. L., Sykora, M. & Mattossi, H. *Phys. Rev. B* **73**, 245302 (2006)
- [Protasenko 2005] Protasenko, V. V., Hull, K. L. & Kuno, M. *Adv. Mater.* **17**, 2942 (2005)
- [Querner 2008] Querner, C., Wang, S., Healy, K., Fairfield, J. A., Fischbein, M. D. & Drndic, M. *J. Phys. Chem. C* **112**, 19945 (2008)
- [Reiss 2002] Reiss, P., Bleuse, J. & Pron, A. *Nano Lett.* **2**, 781 (2002)
- [Reiss 2003] Reiss, P., Carayon, S., Bleuse, J. & Pron, A. *Synth. Met.* **139**, 649 (2003)
- [Rothenberg 2004] Rothenberg, E., Ebenstein, Y., Kazes, M. & Banin, U. *J. Phys. Chem. B* **108**, 2797 (2004)
- [Rothenberg 2005] Rothenberg, E., Kazes, M., Shaviv, E. & Banin, U. *Nano Lett.* **5**, 1581 (2005)
- [Shabaev 2004] Shabaev, A. & Efros, A. L. *Nano Lett.* **4**, 1821 (2004)

- [Shieh 2005] Shieh, F., Saunders, A. E. & Korgel, B. A. *J. Phys. Chem. B* **109**, 8538 (2005)
- [Shimizu 2001] Shimizu, K. T., Neuhauser, R. G., Leatherdale, C. A., Empedocles, S. A., Woo, W. K. & Bawendi, M. G. *Phys. Rev. B* **63**, 205316 (2001)
- [Shubeita 2003] Shubeita, G. T., Sekatskii, S. K., Dietler, G., Potapova, I., Mews, A. & Basche, T. *J. Microsc.* **210**, 274 (2003)
- [Tang 2005a] Tang, J. & Marcus, R. A. *J. Chem. Phys.* **123**, 054704 (2005)
- [Tang 2005b] Tang, J. & Marcus, R. A. *Phys. Rev. Lett.* **95**, 107401 (2005)
- [Tang 2005c] Tang, J. & Marcus, R. A. *J. Chem. Phys.* **123**, 204511 (2005)
- [Tang 2006] Tang, J. & Marcus, R. A. *J. Chem. Phys.* **125**, 044703 (2006)
- [Tang 2007] Tang, J. *J. Phys. Chem. A* **111**, 9336 (2007)
- [Uematsu 2005] Uematsu, T., Maenosono, S. & Yamaguchi, Y. *J. Phys. Chem. B* **109**, 8613 (2005)
- [Wang 2006] Wang, S., Querner, C., Emmons, T., Drndic, M. & Crouch, C. H. *J. Phys. Chem. B* **110**, 23221 (2006)
- [Wang 2008] Wang, S., Querner, C., Fischbein, M. D., Willis, L., Novikov, D. S., Crouch C. H., & Drndic, M. *Nano Lett.* **8**, 4020 (2008)
- [Wang 2009] Wang, X., Ren, X., Kahlen, K., Hahn, M. A., Rajeswaran, M., Maccagnano-Zacher, S., Silcox, J., Cragg, G. E., Efros, A. L. & Krauss, T. D. *Nature* **459**, 686 (2009)
- [Xu 2006] Xu, L., Xu, J., Ma, Z., Li, W., Huang, X. & Chen, K. *Appl. Phys. Lett.* **89**, 0331212 (2006)
- [Yao 2005] Yao, J., Larson, D. R., Vishwasrao, H. D., Zipfel, W. R. & Webb, W. W. *Proc. Natl. Acad. Sci.* **102**, 14284 (2005)

- [Yu 2006] Yu, M. & Van Orden, A. *Phys. Rev. Lett.* **97**, 237402 (2006)
- [van Sark 2002] van Sark, W. G. J. H. M., Frederix, P. L. T. M., Bol, A. A., Gerritsen, H. C. & Meijerink, A. *Chem. Phys. Chem.* **3**, 871 (2002)
- [Verberk 2005] Verberk, R., Chon, J. W. M., Gu, M. & Orrit, M. *Physica E* **26**, 19 (2005)
- [Zhang 2006] Zhang, K., Chang, H., Fu, A., Alivisatos, A.P. & Yang, H. *Nano Lett.* **6**, 843 (2006)